

MINIATURE MASS SPECTROMETRY: THEORY, DEVELOPMENT
AND APPLICATIONS

James D. Fox, M.S.

Dissertation Prepared for the Degree of
DOCTOR OF PHILOSOPHY

UNIVERSITY OF NORTH TEXAS

December 2013

APPROVED:

Guido Verbeck, Major Professor
Rob Petros, Committee Member
Teresa D. Golden, Committee Member
Thomas Scharf, Committee Member
William E. Acree, Jr., Chair of the Department
of Chemistry
Mark Wardell, Dean of the Toulouse Graduate
School

Fox, James D. Miniature Mass Spectrometry: Theory, Development and Applications.

Doctor of Philosophy (Chemistry-Analytical Chemistry), December 2013, 106 pp., 53

illustrations, chapter references.

As mass analyzer technology has continued to improve over the last fifty years, the prospect of field-portable mass spectrometers has garnered interest from many research groups and organizations. Designing a field portable instrument entails more than the scaling down of current commercial systems. Additional considerations such as power consumption, vacuum requirements and ruggedization also play key roles. In this research, two avenues were pursued in the initial development of a portable system. First, micrometer-scale mass analyzers and other electrostatic components were fabricated using silicon on insulator-deep reactive ion etching, and tested. Second, the dimensions of an ion trap were scaled to the millimeter level and fabricated from common metals and commercially available vacuum plastics. This instrument was tested for use in ion isolation and collision induced dissociation for secondary mass spectrometry and confirmatory analyses of unknowns.

In addition to portable instrumentation, miniature mass spectrometers show potential for usage in process and reaction monitoring. To this end, a commercial residual gas analyzer was used to monitor plasma deposition and cleaning inside of a chamber designed for laser ablation and soft landing-ion mobility to generate metal-main group clusters. This chamber was also equipped for multiple types of spectral analysis in order to identify and characterize the clusters.

Finally, a portion of this research was dedicated to method development in sample collection and analysis for forensic study. A new method for the analysis of illicit chemistries collected via electrostatic lifting is presented. This method incorporates surface-enhanced Raman microscopy as a prescreening tool for nanoextraction and nanospray ionization mass spectrometry.

Copyright 2013

by

James D. Fox

ACKNOWLEDGEMENT

I would like to begin by thanking my advisor and mentor, Dr. Guido Fridolin Verbeck, IV, who has mentored me during my time at the University of North Texas. His guidance has produced a wealth of professional and personal growth that has enriched my experience as a chemist and prepared me for life beyond the academic setting. I would also like to thank Dr. Rob Petros, Dr. Teresa Golden and Dr. Thomas Scharf for taking the time to serve on my committee, as well as the McStay family for funding a very significant portion of my education. I would like to thank my colleagues in the Verbeck group and the Department of Chemistry; their friendship helped to alleviate the tedium and anxiety of the past five years. Additionally, I would like to thank Dr. Martin Gieda for offering sound counsel during the most difficult leg of this journey. I would like to thank my family, whose love and support have carried me through the years and helped to shape the man I have become. I am so blessed to have them. Finally, I would like to thank Kelsey Crain, who once told me “just put one foot in front of the other”.

TABLE OF CONTENTS

	Page
ACKNOWLEDGEMENT	iii
LIST OF FIGURES	vi
Chapters	
1. INTRODUCTION	1
1.1 Overview of Miniaturized Mass Spectrometers	1
1.2 Advantages of Ion Trap	2
1.3 Fabrication Methods for Miniaturized Instruments	6
1.4 Raman Microscopy	7
1.5 Plasma Deposition and Modification.....	8
1.6 References.....	9
2. THE UNDERLYING THEORY OF THE QUADRUPOLE ION TRAP	15
2.1 The Mathieu Function.....	15
2.2 The Quadrupole Field	16
2.3 Regions of Stability.....	20
2.4 References.....	28
3. DESIGN AND DEVELOPMENT OF A MINITURE CYLINDRICAL ION TRAP.....	30
3.1 Introduction.....	30
3.2 Experimental	31
3.3 Results and Discussion	35
3.5 References.....	40

4. MEMS ASEMBLED ION OPTICS: AN ADVANCE TO MINIATURIZATION AND ASSEMBLY OF ELECTRON ION OPTICS	42
4.1 Introduction.....	42
4.2 Experimental	50
4.3 Results and Discussion	54
4.5 References.....	57
5. SOFT LANDING-ION MOBILITY AND MONITORING PLASMA DEPOSITION IN SITU VIA MINIATURE MASS SPECTROMETRY.....	61
5.1 Introduction.....	61
5.2 Platform Design	62
5.3 Substrate Preparation	65
5.4 Soft Landing-Ion Mobility and Raman Spectroscopy	65
5.5 Plasma Deposition and Mass Spectrometry.....	71
5.7 References.....	86
6. SURFACE-ENHANCED RAMAN SCATTERING AS A PRE-SCREENING TOOL FOR MASS SPECTROMETRY	88
6.1 Introduction.....	88
6.2 Methods.....	90
6.3 Results.....	92
6.5 References.....	101
7. CONCLUSIONS AND FUTURE WORK.....	103

LIST OF FIGURES

FIG. 1— <i>Number of ions stored and number of traps as a function of trap radius on a 1.0 cm² footprint.....</i>	5
FIG. 2— <i>Four visual representations of ion trap arrays on a 1.0 cm² footprint with 0.5 cm, 0.05 cm, 0.005 cm and 0.0005 cm r₀.....</i>	6
FIG. 3— <i>Cross-section of the cylindrical ion trap showing the trapping electrode and endcaps. The dimensions r₀ and z₀ are indicated on the interior of the trap.....</i>	18
FIG. 4— <i>Stability diagram for the first (lower) and second (upper) stability regions (shaded in gray) in one dimension.....</i>	22
FIG. 5— <i>β_u lines (black) compared with boundary lines (red).</i>	23
FIG. 6— <i>First stability region for a quadrupolar ion trap in the axial (red) and radial (black) dimensions.....</i>	25
FIG. 7— <i>Stability limits for an r₀=0.5 mm ion trap running RF-only at 6.5 MHz as a function of mass.....</i>	26
FIG. 8— <i>Stability regions for an ion trap with a 6.5 MHz trapping frequency and an r₀ of 0.5 mm (black), 1.0 mm (red) and 1.5 mm (blue). Regions of one-dimensional stability have been omitted for clarity.</i>	27
FIG. 9— <i>Stability regions for an r₀=0.5 mm ion trap using a trapping frequency of 4.0 MHz (black), 6.0 MHz (red) and 8.0 MHz (blue).</i>	27
FIG. 10— <i>Cross sectional view of the miniature cylindrical ion trap: I) Vespel housing, II) filament, III) focusing lenses, IV) endcaps, V) trapping ring, VI) channeltron. Dimensions are listed in inches.</i>	33

FIG. 11— <i>Mass spectra of xylene product ions (105, 106, 107 m/z) versus absolute intensity (uV) for isolation times at 2, 4, 6, 8 and 10 ms.....</i>	35
FIG. 12— <i>Integrated ion signal for xylene at different isolation times.....</i>	36
FIG. 13— <i>Mass spectra of xylene product ions (91, 92 m/z) versus absolute intensity (uV) for CID times at 2-10 ms at 1 V.....</i>	37
FIG. 14— <i>Integrated signals from the mass spectra of xylene with incrementally longer CID times.....</i>	38
FIG. 15— <i>Mass spectra of xylene product ions (91, 92 m/z) versus absolute intensity (uV) at 0-1 V of CID energy at 10 ms CID time.....</i>	38
FIG. 16— <i>Integrated signals from the mass spectra of xylene at different CID voltages.....</i>	39
FIG. 17— <i>Schematic of a) wet chemical etching, b) LIGA and c) SIO-DRIE</i>	43
FIG. 18— <i>SEM image of the 250 μm diameter ion trap developed using chemical etching processes. Surface aberrations, edge effects and taper of the wall are illustrated.</i>	44
FIG. 19— <i>SEM image of the ion trap arra developed using LIGA: (a) tapering of the sidewalls in the square channel array; (b) heavy scalloping and irregularities on the edge of the arra are shown.</i>	46
FIG. 20— <i>SEM image of (a) the grid and (b) the cylindrical ion trap developed using the SOI DRIE process.</i>	48
FIG. 21— <i>SEM image of the Bradbury-Nelson Gate; electrode wires are 10 μm in width with 50 μm spacing.</i>	51
FIG. 22— <i>SEM image of the assembled Coaxial Ring Ion Trap (80x magnification); 500 μm i.d. ring electrodes, 75 μm i.d. endcap electrodes.</i>	52

FIG. 23—SEM image of the Reflectron Optics; rectangular elements are 1.0 mm high, 2.0 mm long, 0.05 mm thick with 0.5 mm spacing.....	53
FIG. 24—Data from the Bradbury-Neslon Gate alternating between 60V-60V and 60V-30V positions.....	55
FIG. 25—The signal distribution from the Einzel lens with both a 100 V and a 500 V ion beam.	56
FIG. 26—Spectrum obtained from a mixture of 10^{-4} torr He with 1% toluene on the coaxial ring ion trap (dotted line indicate V_{p-p}).	56
FIG. 27—Model depicting the multi-analysis platform consisting of the vacuum chamber (A), Raman microscope (B), quartz plasma tube (C), SLIM instrument (D), mass spectrometer (E), linear sample actuator (F) and MCT/A IR detector (G).....	63
FIG. 28—The soft landing-ion mobility cell.....	64
FIG. 29—The ion mobility spectrum of hafnium ablated in 5% O_2 in He at 5.0 torr.	66
FIG. 30—In situ Raman spectrum of HfO_2 and 50x micrograph of the particle analyzed.	68
FIG. 31—Ex situ Raman spectrum of HfO_2 and 50x micrograph of the particle analyzed.	69
FIG. 32—Micrograph of the silicon wafer. Panels A,D and G show 10x images of the 4,8 and 12 hour deposition surfaces respectively. Broad SEM images can be seen in B (4 hour, 607x), E (8 hour, 100x) and H (12 hour, 97x). Representative particles in the different section of the wafer can be seen in C (4 hour, 6284x), F (8 hour, 6996x) and I (12 hour, 4796x).	70
FIG. 33—The vacuum chamber equipped with the plasma tube (A), sample feed-through (B) and mass spectrometer (C).	72
FIG. 34—Mass spectra for the vacuum chamber with the mass spec valve closed (A), the valve open (B) and the valve open with the plasma ignited (C).	74

FIG. 35—Total ion counts for the mass spectra collected during the chamber's initial evacuation with the dry scroll pump	76
FIG. 36—Total ion counts (left) and O/O ₂ ratios (right) for the plasma exhaust as a function of RF power (top) and chamber pressure (bottom).	76
FIG. 37—Mass spectra of the acetylene buffer gas before plasma ignition (left) and after (right).	77
FIG. 38—Ion traces of the species of interest during the carbon deposition.....	78
FIG. 39—Raman spectrum of the carbon deposits collected from the plasma tube with an image of the deposited material inlaid.	80
FIG. 40—Raman spectrum of the carbon film deposited in the silicon wafer. A closer inspection of the 1500 cm ⁻¹ region is inlaid.	80
FIG. 41—Ion traces of the species of interest during oxygen plasma cleaning.	83
FIG. 42—Comparison of the ion counts at the beginning of each pump cycle and after an appreciable pumping time. The spectra were collected in the presence of the oxygen-containing plasma.....	84
FIG. 43—Raman spectrum of the carbon deposited after 72 hours of pumping via the rotary vane pump.	85
FIG. 44—Total ion counts for the caffeine peak in the mass spectra for samples lifted using 5-40 seconds of applied voltage.	93
FIG. 45—Microscope image of the aream mapped in the Raman analysis of cocaine and sand (bottom left). Contour map overlaid in the image (top left) showing areas of cocaine signal in grey and white (the threshold peak intensity for white is 12.23 a.u.). Three-dimensional plot of the Raman image with the microscope image overlaid (right).	94

FIG. 46— <i>Schematic diagram of a two-step lifting process where a) a primary lift containing both analyte (white) and matrix (grey) particles is covered with a gold-coated film and b) a secondary lift is performed to collect the analyte particles for SERS analysis, leaving the primary lift in tact.</i>	95
FIG. 47— <i>Raman spectrum of the caffeine standard on a) Mylar® film, b) 25 nm gold film, c) 60 nm gold film and d) 100 nm gold film.</i>	96
FIG. 48— <i>Comparisons of the full spectra for (a) caffeine on Mylar® and (b) caffeine on the 100 nm gold film.</i>	96
FIG. 49— <i>Raman spectrum for cocaine on a) Mylar® film, b) 25 nm gold film, c) 60 nm gold film and d) 100 nm gold film.</i>	97
FIG. 50— <i>Raman spectrum for crystal meth on a) Mylar® film, b) 25 nm gold film, c) 60 nm gold film and d) 100 nm gold film.</i>	98
FIG. 51— <i>Raman spectrum for MDMA on a) Mylar® film, b) 25 nm gold film, c) 60 nm gold film and d) 100 nm gold film.</i>	98
FIG. 52— <i>Comparison of the signal-to-noise ratios for the four samples on each of the films.</i> ..	99
FIG. 53— <i>Comparisons of ESI/MS (left) and NSI/MS (right) for caffeine (a,b), cocaine (c,d), MDMA (e,f) and methamphetamine (g,h).</i>	100

CHAPTER 1

INTRODUCTION

1.1 Overview of Miniaturized Mass Spectrometers

Over the past century, the field of mass spectrometry has grown from its roots in physics to encompass a broad array of areas in basic and applied research, bridging the fields of chemistry, physics, biology and more. While Thomas is typically credited with its invention (1), it was the work of Prout that sparked the intellectual fuse that still burns today (2). During the last two decades, the focus of many a research group has been on the miniaturization of different types of mass analyzers, and eventually, miniaturization of the mass spectral systems as a whole (3, 4). This work began in 1991 in two different lines of research. Like many other significant discoveries, the intent to build a miniature/portable instrument was not *a priori* for Kaiser et al. who developed quadrupole ion traps (QIT) of smaller dimensions in order to solve the issue of limited mass range common to instruments of that era (5). On the other hand, it was field deployability that spurred the development of a portable magnetic sector mass spectrometer (6). Since then, the prospect of portable or field-deployable mass spectrometers has been caught the attention of a broad cross section of the research community.

Since the turn of the century, a number of miniature mass analyzers have been developed. Miniature time-of-flight (TOF) instruments have been successfully developed for the analysis of peptides and oligonucleotides (7), as well as atomic composition (8). The appeal of the miniature TOF is undeniable, as it requires no radio frequency voltages or strong magnetic fields, leading to reduced power requirements for an individual instrument. As previously mentioned, magnetic sector instruments have also received attention (9, 10). Good resolution and mass

range has also been coaxed from small-scale linear quadrupoles (LQ) instruments (11, 12). However, there is a wealth of study on miniaturized quadrupole ion trap instruments (13-19), including rectilinear (20-23) and toroidal geometries (24). With the apparent bias for ion trap devices, it is important to look at the reasons such an instrument might be chosen.

1.2 Advantages of Ion Trap

The first thing one notes when reviewing the literature on miniature ion traps is that, in general, the geometry of the trap has been simplified from the standard Paul trap to a cylindrical ion trap. This particular geometry was first used for ion storage (25), and later as a mass analyzer (26). The effect of this geometry on the quadrupolar field and stability regions have been investigated (27). From here, references to miniature ion traps will refer to the cylindrical geometry unless otherwise noted.

When reducing the dimensions of a standard mass analyzer, there are a number of consequences and changes in the characteristic of the device that must be taken into consideration. This also extends to the components of the mass spectrometer that do not participate in ion separation. At first glance, the miniature ion trap provides the ability for tandem mass spec, lower vacuum and power requirements and a broader mass range than its other miniature counterparts (28). Looking closer reveals more. Consider the equations describing the operation of several typical mass analyzers in terms of resolving power:

$$\text{TOF} \quad R \propto \frac{L}{E_z} \quad (1.1)$$

$$\text{LQ} \quad R \propto \frac{1}{E_z} \left(\frac{L}{\pi r} \right)^2 \quad (1.2)$$

$$\text{Magnetic Sector} \quad R \propto \frac{B^2 r^2}{V} \quad (1.3)$$

$$R \propto D_Z t \quad (1.4)$$

Understandably, resolution in the TOF relies in the length (L) of the ion flight path and the field generated by the accelerating pulse (E_Z). In many commercial instruments, the path is lengthened via a reflectron, increasing the resolution. This idea has spread to miniaturized versions (29). The linear quad goes a step further where resolution is proportional to the square of the length (L) of the mass analyzer. In a similar fashion, the sector mass spec's resolution is proportional to the magnitude of the magnetic field (B) and voltage (V), but it is the square of the radius (r) of the sector that draws our attention. At first glance, it appears as though the quadrupole ion trap has broken free of the dimensional reliance on resolution, but in order to understand properly, the expression for the depth of the pseudopotential well (D_Z) needs to be examined (30):

$$D_Z = \frac{eV^2}{4mz_0^2\omega^2} \quad (1.5)$$

where e is elementary charge, V is the zero-to-peak radio frequency (rf) voltage applied to the field, m is the ion mass z_0 is the distance from the center of the trap to the endcap and ω is the angular frequency of the rf voltage. It should be noted that the overall dimensions of the ion trap are implicitly defined here as the radius of the trap is related to its length by

$$r_0^2 = 2z_0^2 \quad (1.6)$$

Now it appears that, in theory, as the dimensions of the ion trap decrease, the depth of the pseudopotential well (and thus, the resolution) increase. However, this apparent benefit comes at a cost. Consider the maximum number of ions that can be stored in an ion trap in a given event (31):

$$N_{\max} = \frac{3\epsilon_0 V^2}{4mz_0^4 \omega^2} \quad (1.7)$$

where ϵ_0 is the permittivity of free space. As the CIT size is reduced the number of ion stored in that trap is reduced. A typical 1.0 cm trap can hold approximately 10^6 – 10^7 ions and a 1.0mm trap will hold approximately 10^5 ions. This relationship between trap size and ion attenuation is detrimental to the successful development of small, single miniature ion traps. However, if the number of CITs is increased as the trap radius is reduced, then the total number of ions stored in all traps combined increases. Fig 1 shows the relationship of ions stored in all traps and number of traps versus trap radius. Assuming that the trap spacing is equal to trap diameter, it can be seen that in a 1.0 cm footprint, 2500 arrayed CITs (at 50 μm) is the beginning of increased ion storage as compared to a single CIT. Fig 2 is a simple representation of how smaller ion traps can be arrayed on a 1 cm \times 1 cm chip. With the arraying of multiple ion traps the perceived problem of signal attenuation inherent in miniaturization is avoided. Trap arraying has recently been explored by several groups (32-38).

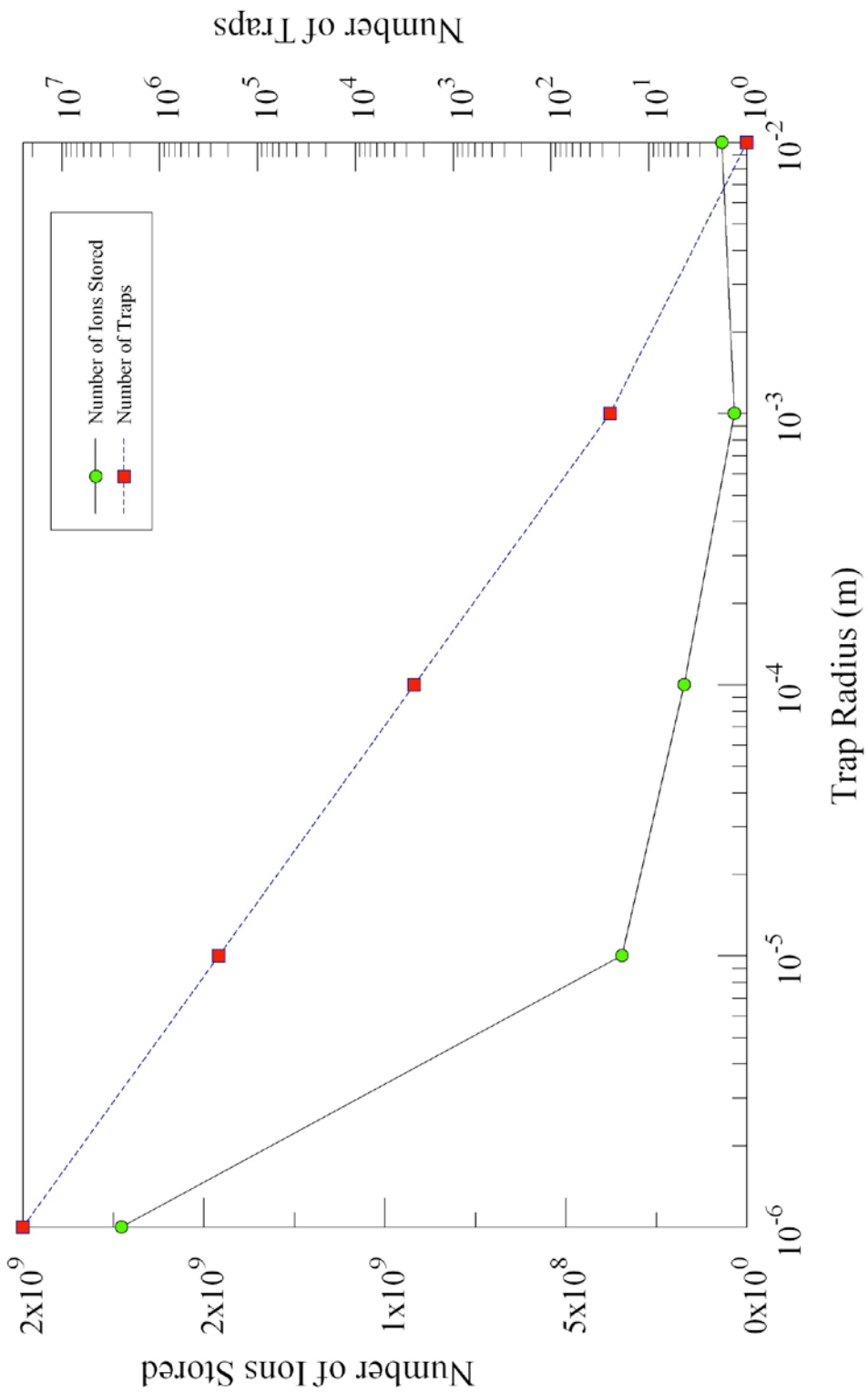


FIG. 1—Number of ions stored and number of traps as a function of trap radius on a 1.0 cm^2 footprint.

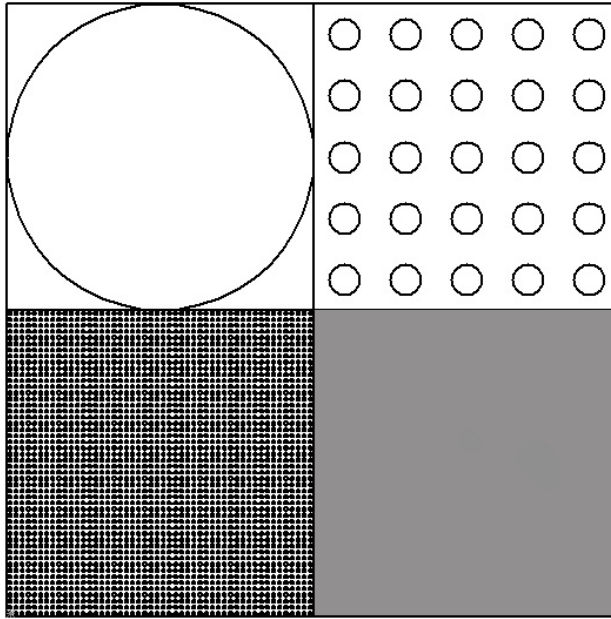


FIG. 2—*Four visual representations of ion trap arrays on a 1.0 cm² footprint with 0.5 cm, 0.05 cm, 0.005 cm and 0.0005 cm r₀.*

1.3 Fabrication Methods for Miniaturized Instruments

As the size of instrument components has decreased over the years, different methods of fabrication have been adapted to meet the demands of tighter dimensional tolerances and complexity of design. At the outset, and for simple components of centimeter-scale instruments, the use of stainless steel and classic machining techniques still provide an efficient route for manufacturing. For cylindrical ion traps, the overall geometry differs little from the average electrostatic lens, and the challenge in creating a trap essentially becomes polishing the surface to eliminate defects that would otherwise cause field aberrations, lowering the performance of the mass analyzer. By extension, the machining of TOF components of similar scale can follow the same convention. For a linear quadrupole, the use of conventional cylindrical rods as opposed to the more accurate hyperbolic rods lends itself to simple fabrication on a small scale via extrusions and polishing of the quadrupole rods. However, as previously discussed, the impetus

to create even smaller-scale or more complex components has necessitated more sophisticated methods.

Recently, several methods have been utilized in the manufacturing of small-scale devices, such as wet chemical etching (39-41), LIGA (from the German phrase "Lithographie, Galvanoformung, Abformung,") (42-45), and silicon on insulator-deep reactive ion etching (46-49). Each has been effectively used in the fabrication of micrometer-scale components, but defects on the etched surfaces prevent chemical etching and LIGA from manufacturing electrostatic components that can be effectively used in miniature mass spectrometers. Each of these methods is discussed further in Chapter 4.

1.4 Raman Microscopy

While the inelastic scattering of light was first postulated in 1923 (50), it was not until five years later that Sir Chandrasekhara Venkata Raman reported observing this phenomenon (51). The underlying theory was not well understood until later (52). While not specifically duplication the spectra obtained from infrared or microwave spectroscopies, this two-photon process allows for the observation of vibrational and rotational modes of molecules using visible or near-visible radiation (53), typically in the form of focused lasers. High-resolution spectra can be obtained using simple optics and without the need for Fourier transform methods. Much later in its lifetime, this effect was applied to samples on the microscopic scale with considerable success (54). In Raman microscopy, the laser is passed through the objective of an optical microscope and point-focused on the sample surface. The light reflected from the surface is simultaneously collected with the objective and, using either a beam splitter or switching optics, diverted to a spectrophotometer. This method allows for the examination of samples otherwise impossible to analyze with simple Raman techniques. Using conventional optics, the typical

spatial resolution obtained in these instruments is approximately 1.0 μm , although smaller resolution can be obtained with fine-tuning (55). To extend this idea, spatial resolution as low as 10 nm can be obtained via coupling to atomic force or scanning tunneling microscopy (56).

This method has wide ranging applications from analysis of analyte particles in complex matrices (57, 58), to the spectroscopic imaging of large biological (59) and inorganic (60) samples. Through the use of surface-enhanced Raman scattering (SERS) and some sophisticated chromophore/nanoparticle coupling, viable spectra have even been collected from single molecules (61). It has also been key in the study of carbon thin films (62, 63)

The coupling of Raman microscopy to other analytical methods acts synergistically to provide multifaceted analyses that can act as a qualitative confirmational or quick-screening tool to filter samples for further study. This approach is discussed at length in a later chapter

1.5 Plasma Deposition and Modification

In general, plasma can be viewed as low- and high-temperature, and both can be generated in distinctly different ways. High temperature plasmas are defined by the homogeneity of plasma particle energies. That is, the temperature of the electrons, ions and gas are all approximately the same (referred to as local thermodynamic equilibrium). In a low-temperature plasma, the temperature of the electrons are significantly higher than all other species in the gas (partial thermodynamic equilibrium), typically by two orders of magnitude or more (64).

Low-temperature plasmas have found many uses in basic research and industrial processing over the decades. It has recently been used in the semiconductor industry for the deposition of thin, dielectric films (65, 66) carbon films (67) and the growth of carbon nanotubes (68, 69). Additionally, such films have also been modified by low-temperature plasmas (70, 71).

Another critical use in industrial processes is surface cleaning, and it has been applicable on scale from large mechanical components (72) to microelectrical mechanical devices (73).

Plasma may be easily integrated into a vacuum system. For a low-temperature plasma, applying either a high DC or RF voltage between two electrodes or between an electrode and the sample at millitorr pressures will ignite and sustain the plasma. The benefit of using RF over DC is in the inductive properties of AC. For a simplified plasma system, copper electrodes can be placed around the exterior of an insulating portion of the vacuum chamber in order to generate plasma inside, eliminating the need for vacuum-compliant materials for the plasma system. This type of parallel-plate capacitatively-coupled plasma will be discussed in more detail in a later chapter.

The next chapters of this dissertation will discuss quadrupole ion trap theory and the design and development of a miniature instrument. The last chapters will be dedicated to applications of the instrumentation and methods mentioned above.

1.6 References

1. Griffiths J. A Brief History of Mass Spectrometry. *Analytical Chemistry*. [doi: 10.1021/ac8013065]. 2008 2008/08/01;80(15):5678-83.
2. Prout W. On the Relation between the Specific Gravities fo Bodies in their Gaseous State and the Weight of their Atoms. *Annals of Philosophy*. 1815;v. 6
3. Ouyang Z, Noll RJ, Cooks RG. Handheld Miniature Ion Trap Mass Spectrometers. *Analytical Chemistry*. 2009 Apr 1;81(7):2421-5.
4. Ethan RB, Cooks RG. Miniature mass analyzers. *J Mass Spectrom*. 2000;35(6):659-71.
5. Kaiser Jr RE, Graham Cooks R, Stafford Jr GC, Syka JEP, Hemberger PH. Operation of a quadrupole ion trap mass spectrometer to achieve high mass/charge ratios. *International Journal of Mass Spectrometry and Ion Processes*. 1991;106(0):79-115.
6. Sinha MP, Tomassian AD. Development of a miniaturized, light-weight magnetic sector for a field-portable mass spectrograph. *Rev Sci Instrum*. 1991;62(11):2618-20.

7. Cotter RJ, Fancher C, Cornish TJ. Miniaturized time-of-flight mass spectrometer for peptide and oligonucleotide analysis. *J Mass Spectrom.* 1999 Dec;34(12):1368-72.
8. Brinckerhoff WB, Cornish TJ, McEntire RW, Cheng AF, Benson RC. Miniature time-of-flight mass spectrometers for in situ composition studies. *Acta Astronaut.* 2003 Jan-Mar;52(2-6):397-404.
9. Li DT, Guo MR, Xiao YH, Zhao YD, Wang L. Development of a miniature magnetic sector mass spectrometer. *Vacuum.* 2011 Jun 5;85(12):1170-3.
10. Diaz JA, Giese CF, Gentry WR. Sub-miniature ExB sector-field mass spectrometer. *J Am Soc Mass Spectr.* 2001 Jun;12(6):619-32.
11. Clare AT, Gao L, Brkifá B, Chalker PR, Taylor S. Linear Ion Trap Fabricated Using Rapid Manufacturing Technology. *J Am Soc Mass Spectr.* 2010;21(2):317-22.
12. Arkin CR, Griffin TP, Diaz JA, Follistein DW, Curley CH, Floyd DP, et al. A small mass spectrometer system for in situ gas analysis. *Trac-Trend Anal Chem.* 2004 Apr;23(4):322-30.
13. Smith JN, Keil AD, Noll RJ, Cooks RG. Ion/molecule reactions for detecting ammonia using miniature cylindrical ion trap mass spectrometers. *Analyst.* 2011;136(1):120-7.
14. Moxom J, Reilly PTA, Whitten WB, Ramsey JM. Double resonance ejection in a micro ion trap mass spectrometer. *Rapid Commun Mass Sp.* 2002;16(8):755-60.
15. Moxom J, Reilly PTA, Whitten WB, Ramsey M. Analysis of volatile organic compounds in air with a micro ion trap mass analyzer. *Anal Chem.* 2003 Aug 1;75(15):3739-43.
16. Moxom J, Reilly PTA, Whitten WB, Ramsey JM. Sample pressure effects in a micro ion trap mass spectrometer. *Rapid Commun Mass Sp.* 2004;18(6):721-3.
17. Pau S, Pai CS, Low YL, Moxom J, Reilly PTA, Whitten WB, et al. Microfabricated quadrupole ion trap for mass spectrometer applications. *Phys Rev Lett.* 2006 Mar 31;96(12):-.
18. Zhu ZQ, Xiong CQ, Xu GP, Liu H, Zhou XY, Chen R, et al. Characterization of bioparticles using a miniature cylindrical ion trap mass spectrometer operated at rough vacuum. *Analyst.* 2011;136(7):1305-9.
19. Gao L, Li GT, Cooks RG. Axial CID and High Pressure Resonance CID in a Miniature Ion Trap Mass Spectrometer Using a Discontinuous Atmospheric Pressure Interface. *J Am Soc Mass Spectr.* 2010 Feb;21(2):209-14.
20. Graichen AM, Vachet RW. Multiplexed MS/MS in a Miniature Rectilinear Ion Trap. *J Am Soc Mass Spectr.* 2011 Apr;22(4):683-8.

21. Maas JD, Hendricks PI, Ouyang Z, Cooks RG, Chappell WJ. Miniature Monolithic Rectilinear Ion Trap Arrays by Stereolithography on Printed Circuit Board. *J Microelectromech S.* 2010 Aug;19(4):951-60.
22. Sokol E, Edwards KE, Qian K, Cooks RG. Rapid hydrocarbon analysis using a miniature rectilinear ion trap mass spectrometer. *Analyst.* 2008;133(8):1064-71.
23. Jiang J, Fei Q, Jin W, Li M, Pang XD, Li B, et al. Miniature rectilinear ion trap mass spectrometry. *Chinese J Anal Chem.* 2007 Sep;35(9):1387-90.
24. Lammert SA, Rockwood AA, Wang M, Lee ML, Lee ED, Tolley SE, et al. Miniature toroidal radio frequency ion trap mass analyzer. *J Am Soc Mass Spectr.* 2006 Jul;17(7):916-22.
25. Grebner TL, Neusser HJ. Laser produced ions stored in a cylindrical ion trap and detected in a reflectron time-of-flight mass spectrometer. *International Journal of Mass Spectrometry and Ion Processes.* 1994;137(0):L1-L6.
26. Wells JM, Badman ER, Cooks RG. A Quadrupole Ion Trap with Cylindrical Geometry Operated in the Mass-Selective Instability Mode. *Analytical Chemistry.* [doi: 10.1021/ac971198h]. 1998 1998/02/01;70(3):438-44.
27. Benilan M-N, Audoin C. Confinement d'ions par un champ électrique de radio-fréquence dans une cage cylindrique. *International Journal of Mass Spectrometry and Ion Physics.* 1973;11(5):421-32.
28. Ouyang Z, Gao L, Fico M, Chappell WJ, Noll RJ, Cooks RG. Quadrupole ion traps and trap arrays: geometry, material, scale, performance. *Eur J Mass Spectrom.* 2007;13(1):13-8.
29. Fox J, Saini R, Tsui K, Verbeck G. Microelectromechanical system assembled ion optics: An advance to miniaturization and assembly of electron and ion optics. *Rev Sci Instrum.* 2009 Sep;80(9):-.
30. Quadrupole mass spectrometry and its applications / Peter H. Dawson, editor. Amsterdam : New York: Elsevier Scientific Pub. Co. ; distributor for the U.S. and Canada, Elsevier/North-Holland, 1976.
31. Benilan MN, Audoin C. *Int J Mass Spectrom.* 1973;7:421-32.
32. Chu YQ, Xiao Y, Ling X, Ding CF. Analytical Performance of Printed Circuit Board Ion Trap Array Mass Analyzer with Electrospray Ionization. *Chinese J Anal Chem.* 2013 Jan;41(1):152-8.
33. Luo C, Ding CF. Optimization of Ion Trap Array Mass Analyzer by Computer Simulation. *Chinese J Anal Chem.* 2012 Jul;40(7):989-95.

34. Bowler R, Gaebler J, Lin Y, Tan TR, Hanneke D, Jost JD, et al. Coherent Diabatic Ion Transport and Separation in a Multizone Trap Array. *Phys Rev Lett.* 2012 Aug 20;109(8).
35. Li XX, Jiang GY, Luo C, Xu FX, Wang YY, Ding L, et al. Ion Trap Array Mass Analyzer: Structure and Performance. *Anal Chem.* 2009 Jun 15;81(12):4840-6.
36. Hensinger WK, Olmschenk S, Stick D, Hucul D, Yeo M, Acton M, et al. T-junction ion trap array for two-dimensional ion shuttling, storage, and manipulation. *Appl Phys Lett.* 2006 Jan 16;88(3).
37. Badman ER, Cooks RG. A parallel miniature cylindrical ion trap array. *Anal Chem.* 2000 Jul 15;72(14):3291-7.
38. Badman ER, Cooks RG. Cylindrical ion trap array with mass selection by variation in trap dimensions. *Anal Chem.* 2000 Oct 15;72(20):5079-86.
39. Jee SE, Lee PS, Yoon BJ, Jeong SH, Lee KH. Fabrication of microstructures by wet etching of anodic aluminum oxide substrates. *Chem Mater.* 2005 Aug 9;17(16):4049-52.
40. Kuo DS, Shou-Jinn C, Ko TK, Shen CF, Hon SJ, Hung SC. Nitride-Based LEDs With Phosphoric Acid Etched Undercut Sidewalls. *Photonics Technology Letters, IEEE.* 2009;21(8):510-2.
41. Jiang YR, Liu GZ, Zhou J. A novel process for circle-like 3D microstructures by two-step wet etching. *Journal of Micromechanics and Microengineering.* 2009 Jan;19(1).
42. Ehrfeld W, Schmidt A. Recent developments in deep x-ray lithography. *J Vac Sci Technol B.* 1998 Nov-Dec;16(6):3526-34.
43. Park DSW, Kim K, Pillans B, Lee JB. Polydimethylsiloxane-based pattern transfer process for the post-IC integration of MEMS onto CMOS chips. *Journal of Micromechanics and Microengineering.* 2004 Mar;14(3):335-40.
44. Goettert J, Datta P, Desta Y, Jin Y, Ling Z-g, Singh V, editors. *LIGA research and service at CAMD.* *Journal of Physics: Conference Series;* 2006. IOP Publishing.
45. Meyer P, Schulz J, Hahn L, Saile V. Why you will use the deep X-ray LIG(A) technology to produce MEMS? *Microsyst Technol.* 2008 Oct;14(9-11):1491-7.
46. Saini R, Jandric Z, Tsui K, Udeshi T, Tuggle D. Assembled micro-electromechanical-systems microcolumn from a single layer silicon process. *J Vac Sci Technol B.* 2004 Nov-Dec;22(6):3168-73.
47. Saini R, Jandric Z, Tsui K, Udeshi T, Tuggle D. Manufacturable MEMS microcolumn. *Microelectron Eng.* 2005 Mar;78-79:62-72.
48. Isakovic AF, Stein A, Warren JB, Narayanan S, Sprung M, Sandy AR, et al. Diamond kinoform hard X-ray refractive lenses: design, nanofabrication and testing. *J Synchrotron Radiat.* 2009 Jan;16:8-13.

49. Abdolvand R, Ayazi F. An advanced reactive ion etching process for very high aspect-ratio sub-micron wide trenches in silicon. *Sensor Actuat a-Phys.* 2008 May 28;144(1):109-16.
50. Smekal A. Zur Quantentheorie der Dispersion. *Naturwissenschaften*. 1923 1923/10/01;11(43):873-5.
51. Raman CV, Krishnan KS. A New Type of Secondary Radiation. *Nature*. 1928;121(3048):501.
52. Placzek G. Rayleigh-Streuung und Raman-Effekt. Leipzig: Akad. Verlagsges., 1934.
53. Lewis IR, Edwards H. *Handbook of Raman Spectroscopy: From the Research Laboratory to the Process Line*: Taylor & Francis, 2001.
54. Andersen ME, Muggli RZ. Microscopical techniques in the use of the molecular optics laser examiner Raman microprobe. *Analytical Chemistry*. [doi: 10.1021/ac00235a013]. 1981 1981/10/01;53(12):1772-7.
55. Adar F, Mamedov S, Whately A. Limits of Spatial Resolution of a Raman Microscope. *Microscopy and Microanalysis*. 2005;11(SupplementS02):728-9.
56. Schmid T, Opilik L, Blum C, Zenobi R. Nanoscale Chemical Imaging Using Tip-Enhanced Raman Spectroscopy: A Critical Review. *Angewandte Chemie International Edition*. 2013;52(23):5940-54.
57. Fox JD, Waverka KN, Verbeck GF. Gold-plating of Mylar lift films to capitalize on surface enhanced Raman spectroscopy for chemical extraction of drug residues. *Forensic Science International*. 2012 Mar 10;216(1-3):141-5.
58. Clemons K, Wiley R, Waverka K, Fox J, Dziekonski E, Verbeck GF. Direct Analyte-Probed Nanoextraction Coupled to Nanospray Ionization–Mass Spectrometry of Drug Residues from Latent Fingerprints. *Journal of Forensic Sciences*. 2013;58(4):875-80.
59. Zhang Y, Hong H, Cai WB. Imaging with Raman Spectroscopy. *Curr Pharm Biotechnol*. 2010 Sep;11(6):654-61.
60. Freye CE, Crane NA, Kirchner TB, Sepaniak MJ. Surface Enhanced Raman Scattering Imaging of Developed Thin-Layer Chromatography Plates. *Analytical Chemistry*. [doi: 10.1021/ac303710q]. 2013 2013/04/16;85(8):3991-8.
61. Zhang R, Zhang Y, Dong ZC, Jiang S, Zhang C, Chen LG, et al. Chemical mapping of a single molecule by plasmon-enhanced Raman scattering. *Nature*. [Letter]. 2013;498(7452):82-6.

62. Ferrari AC. Determination of bonding in diamond-like carbon by Raman spectroscopy. *Diamond and Related Materials*. 2002;11(3, Äì6):1053-61.
63. Currie M, Caldwell JD, Bezires FJ, Robinson J, Anderson T, Chun HD, et al. Quantifying pulsed laser induced damage to graphene. *Appl Phys Lett*. 2011 Nov 21;99(21).
64. Meichsner J. Low temperature plasmas. *Plasma Physics*: Springer; 2005;95-116.
65. Kshirsagar A, Nyaupane P, Bodas D, Duttagupta SP, Gangal SA. Deposition and characterization of low temperature silicon nitride films deposited by inductively coupled plasma CVD. *Applied Surface Science*. 2011;257(11):5052-8.
66. Ay F, Aydinli A. Comparative investigation of hydrogen bonding in silicon based PECVD grown dielectrics for optical waveguides. *Opt Mater*. 2004;26(1):33-46.
67. Stiegler J, Lang T, NygaÄörd-Ferguson M, von Kaenel Y, Blank E. Low temperature limits of diamond film growth by microwave plasma-assisted CVD. *Diamond and Related Materials*. 1996;5(3, Äì5):226-30.
68. Mori S, Suzuki M. Characterization of carbon nanofibers synthesized by microwave plasma-enhanced CVD at low-temperature in a CO/Ar/O₂ system. *Diamond and Related Materials*. 2009;18(4):678-81.
69. Choi YC, Bae DJ, Lee YH, Lee BS, Han IT, Choi WB, et al. Low temperature synthesis of carbon nanotubes by microwave plasma-enhanced chemical vapor deposition. *Synthetic Metals*. 2000;108(2):159-63.
70. Jones JD, Hoffmann WD, Jessep AV, Morris CJ, Verbeck GF, Perez JM. On the mechanism for plasma hydrogenation of graphene. *Appl Phys Lett*. 2010 Dec 6;97(23).
71. Bruser V, Heintze M, Brandl W, Marginean G, Bubert H. Surface modification of carbon nanofibres in low temperature plasmas. *Diamond and Related Materials*. 2004;13(4, Äì8):1177-81.
72. Petasch W, Kegel B, Schmid H, Lendenmann K, Keller HU. Low-pressure plasma cleaning: a process for precision cleaning applications. *Surface and Coatings Technology*. 1997;97(1, Äì3):176-81.
73. Stancu C, Teodorescu M, Galca AC, Dinescu G. Carbon layers cleaning from inside of narrow gaps by a RF glow discharge. *Surface and Coatings Technology*. 2011;205, Supplement 2(0):S435-S8.

CHAPTER 2

THE UNDERLYING THEORY OF THE QUADRUPOLE ION TRAP

2.1 The Mathieu Function

Émile Mathieu first proposed a model to describe the vibration of elliptical membranes in 1868 (1). Almost 150 years later, the principles derived from his equation have found applications in a plethora of other fields, demonstrating their utility in many different scenarios (2). One of the more prominent applications was pioneered by Wolfgang Paul (3, 4) and Hans Dehmelt (5, 6), which later led to their winning the Nobel Prize in 1989. The phenomenon and related technology remained largely esoteric until it was developed into an easily operated and accessible mass analyzer (7, 8).

The underlying theory of quadrupole mass analyzers has been a topic of great interest, and has been explored to a significant degree (9-15). However, to open a discussion on the theory of quadrupole ion traps, it is necessary to address the Mathieu Equation and how it relates to the phenomenon. The notation used in this chapter is adapted from March and Todd (15).

The canonical form of the Mathieu Equation is

$$\frac{d^2u}{d\xi^2} + (a_u - 2q_u \cos 2\xi)u = 0 \quad (2.1)$$

Here, u represents displacement, ξ is a dimensionless number representing $\Omega t/2$ (where Ω is frequency and t is time). The two variables, a_u and q_u , represent dimensionless stability parameters that will later allow for the trapping conditions of the quadrupole to be defined in less abstract terms. To begin, we must first take the second partial derivative with respect to t :

$$\frac{d^2}{dt^2} = \frac{d\xi}{dt} \frac{d}{d\xi} \left(\frac{d}{dt} \right) = \frac{\Omega^2}{4} \frac{d^2}{d\xi^2} \quad (2.2)$$

This leads us to

$$\frac{d^2u}{dt^2} = \frac{\Omega^2}{4} \frac{d^2u}{d\zeta^2} \quad (2.3)$$

It is here that through substitution and rearrangement, Eq. (2.1) becomes

$$\frac{d^2u}{dt^2} = -\left(\frac{\Omega^2}{4}a_u - \frac{2\Omega^2}{4}q_u \cos\Omega t\right)u \quad (2.4)$$

This modification to the Mathieu Equation will be paramount to the conversion of the abstract a_u and q_u values into physical values that define the trapping parameters of the quadrupole device.

2.2 The Quadrupole Field

In a quadrupole field, referenced to Cartesian coordinates, the magnitude of the field can be expressed as

$$\phi_{x,y,z} = A(\lambda x^2 + \sigma y^2 + \gamma z^2) + C \quad (2.5)$$

Here, it can be seen that the eponymous field derives its name from the field strength existing as a function of the square of the distance reference. A is a term representing the potential applied between electrodes of opposing polarity. The terms λ , σ and γ are weighing factors that act to independently scale the effect of the x , y and z coordinates respectively. C is a DC or RF potential that may be applied to the entire system in order to reference it to potential other than ground.

As with all electric fields, it is necessary that second differential of the field equal zero; i.e. that the Laplace equation must be satisfied:

$$\nabla^2 \phi_{x,y,z} = 0 \quad (2.6)$$

So, substituting the field equation, we get

$$\nabla^2 \phi = \frac{\partial^2 \phi}{\partial x^2} + \frac{\partial^2 \phi}{\partial y^2} + \frac{\partial^2 \phi}{\partial z^2} = 0 \quad (2.7)$$

Taking the second partial derivative of the x term, we find

$$\frac{\partial^2 \phi}{\partial x^2} = 2\lambda A \quad (2.8)$$

By extension, we know that the second derivatives for the y and z terms are $2\sigma A$ and $2\gamma A$

respectively. By substituting them into Eq. (2.7), we arrive at the expression

$$\nabla^2 \phi = A(2\lambda + 2\sigma + 2\gamma) = 0 \quad (2.9)$$

Because A is a non-zero term, Eq. (2.9) can be simplified to the following expression:

$$\lambda + \sigma + \gamma = 0 \quad (2.10)$$

An infinite number of combinations exist that satisfy this simple relationship. Applying *lex parsimoniae*, we will choose the simplest terms to describe this relationship in terms of a cylindrical quadrupole ion trap ($\lambda=\sigma=1$ and $\gamma=-2$), and show their relevance to the theory. However, in order to discuss the ion trap effectively, the Cartesian coordinates must be transformed into cylindrical polar coordinates using $x=r \cos \theta$ and $y=r \sin \theta$ (z remains unchanged). With this, Eq. (2.5) becomes

$$\phi_{r,z} = A(r^2 - 2z^2) + C \quad (2.11)$$

The r and z terms here refers to the axial and longitudinal displacement of the ion in the trap (Fig 3).

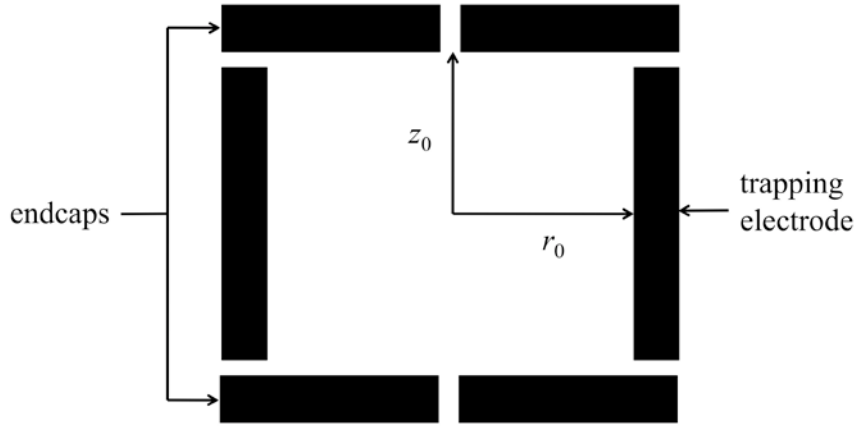


FIG. 3—*Cross-section of the cylindrical ion trap showing the trapping electrode and endcaps. The dimensions r_0 and z_0 are indicated on the interior of the trap.*

Now that the dimensions and potentials have been expressed, the next step is to define A and C in more concrete terms. We begin with the overall expression for the quadrupolar potential in terms of the electrodes of the trap:

$$\phi_o = \phi_{ring} - \phi_{endcaps} \quad (2.12)$$

The individual potentials are separated into their own expressions by setting the value of the other potential to zero

$$\phi_{ring} = A(r_0^2) + C \quad (2.13)$$

$$\phi_{endcaps} = A(-2z_0^2) + C \quad (2.14)$$

and then substituting them into Eq. (2.12):

$$\phi_0 = A(r^2 + 2z^2) \quad (2.15)$$

This allows for a simple rearrangement.

$$A = \frac{\phi_0}{r_0^2 + 2z_0^2} \quad (2.16)$$

Eq. (2.16) is then substituted into Eq. (2.11) to give

$$\phi_{r,z} = \frac{\phi_0(r^2 - 2z^2)}{r_0^2 + 2z_0^2} + C \quad (2.17)$$

From here, we can evaluate C . In terms of a quadrupole ion trap, C is the potential applied to the endcaps. Conventionally, the endcaps on the ion trap are grounded during normal operation. This provides a simple avenue for defining C mathematically by setting the radial potential to zero:

$$\phi_{0,z_0} = \phi_{endcaps} = \frac{\phi_0(0 - 2z_0^2)}{r_0^2 + 2z_0^2} + C = 0 \quad (2.18)$$

And therefore

$$\therefore C = \frac{2\phi_0 z_0^2}{r_0^2 + 2z_0^2} \quad (2.19)$$

And again, returning to Eq. (2.11) and substituting, we finally arrive at the expression

$$\phi_{r,z} = \frac{\phi_0(r^2 - 2z^2)}{r_0^2 + 2z_0^2} + \frac{2\phi_0 z_0^2}{r_0^2 + 2z_0^2} \quad (2.20)$$

We now have a concrete expression for the potential felt by the ions by the trap in terms of the dimensions of the trap itself. From here, the oscillating potential of the radio frequency voltage must be addressed. In order to do so, we consider ϕ_0 such that it is expressed as a function of time,

$$\phi_0 = (U + V \cos \Omega t) \quad (2.21)$$

where V is the zero-to-peak amplitude of the radio frequency voltage, whose angular frequency (Ω) is expressed in radians-per-second and U is a DC offset applied to the trap. Substituting into Eq. (2.20) yields

$$\phi_{r,z} = \frac{(U + V \cos \Omega t)(r^2 - 2z^2)}{r_0^2 + 2z_0^2} + \frac{2(U + V \cos \Omega t)z_0^2}{r_0^2 + 2z_0^2} \quad (2.22)$$

Now we resume the “divide and conquer” approach by considering the force acting upon the ions in the radial and longitudinal directions. Recall that force may be defined as either the product of mass and acceleration or charge and potential. With that in mind, consider the expression for force acting on the ion in the z direction:

$$F_z = -e \left(\frac{d\phi}{dz} \right) = e \frac{4\phi_0 z}{r_0^2 + 2z_0^2} = m \left(\frac{d^2 z}{dt^2} \right) \quad (2.23)$$

Now, substituting Eq. (2.21) gives

$$m \left(\frac{d^2 z}{dt^2} \right) = \frac{4e(U + V \cos \Omega t)z}{r_0^2 + 2z_0^2} \quad (2.24)$$

which we then rearrange and expand to find

$$\frac{d^2 z}{dt^2} = \left(\frac{4eU}{m(r_0^2 + 2z_0^2)} + \frac{4eV \cos \Omega t}{m(r_0^2 + 2z_0^2)} \right) z \quad (2.25)$$

We now arrive at a critical point in the derivation that will take us back to our initial discussion of the Mathieu Equation. Recall from the derivations that led to Eq. (2.4), the Mathieu function was expressed as a partial derivative of displacement (u) with respect to time (t), which is where we have arrived in Eq. (2.25). By changing u to z , we may now directly compare the results of Eq. (2.4) and (2.25):

$$\left(\frac{4eU}{m(r_0^2 + 2z_0^2)} + \frac{4eV \cos \Omega t}{m(r_0^2 + 2z_0^2)} \right) z = - \left(\frac{\Omega^2}{4} a_z - \frac{2\Omega^2}{4} q_z \cos \Omega t \right) z \quad (2.26)$$

Now, it can be seen that the dimensionless stability parameters are all that remain to be defined.

2.3 Regions of Stability

Addressing the two remaining variables in the Mathieu Equation presents the most challenging task yet. Referred to as the “characteristic numbers”, the values for a_u and q_u that provide solutions to the equation represent the two-dimensional boundaries that inside of which

represent “stability”; in pure mathematical terms, the entirety of Mathieu’s function is satisfied.

In the context of quadrupole mass analyzers, values inside the stability regions represent conditions of frequency, amplitude, mass and charge in which an ion is maintained in the oscillating field of the device. Typically, compendia on the theory of mass spectrometry represent the solutions to a_u and q_u as a polynomial. The polynomial equations for a_0 and b_1 , defining the lower and upper boundaries for the first stability region in a single dimension, are (2)

$$a_0 = -\frac{1}{2}q^2 + \frac{7}{128}q^4 - \frac{29}{2304}q^6 + \frac{68687}{18874368}q^8 + O(q^{10}) \quad (2.27)$$

$$\begin{aligned} b_1 = & 1 - q - \frac{1}{8}q^2 + \frac{1}{64}q^3 - \frac{1}{1536}q^4 - \frac{11}{36864}q^5 \\ & + \frac{49}{589824}q^6 - \frac{55}{9437184}q^7 - \frac{256}{113246208}q^8 + O(q^9) \end{aligned} \quad (2.28)$$

Where a_0 and b_1 represent sin and cosine elliptical solutions. Similar expressions exist for higher stability regions. Graphically, these equations can be represented in a_u and q_u space, using McLachlan’s values (Fig 4). It is interesting to note that while the regions of stability are symmetric about the a_u axis, only every third boundary line actually has symmetry.

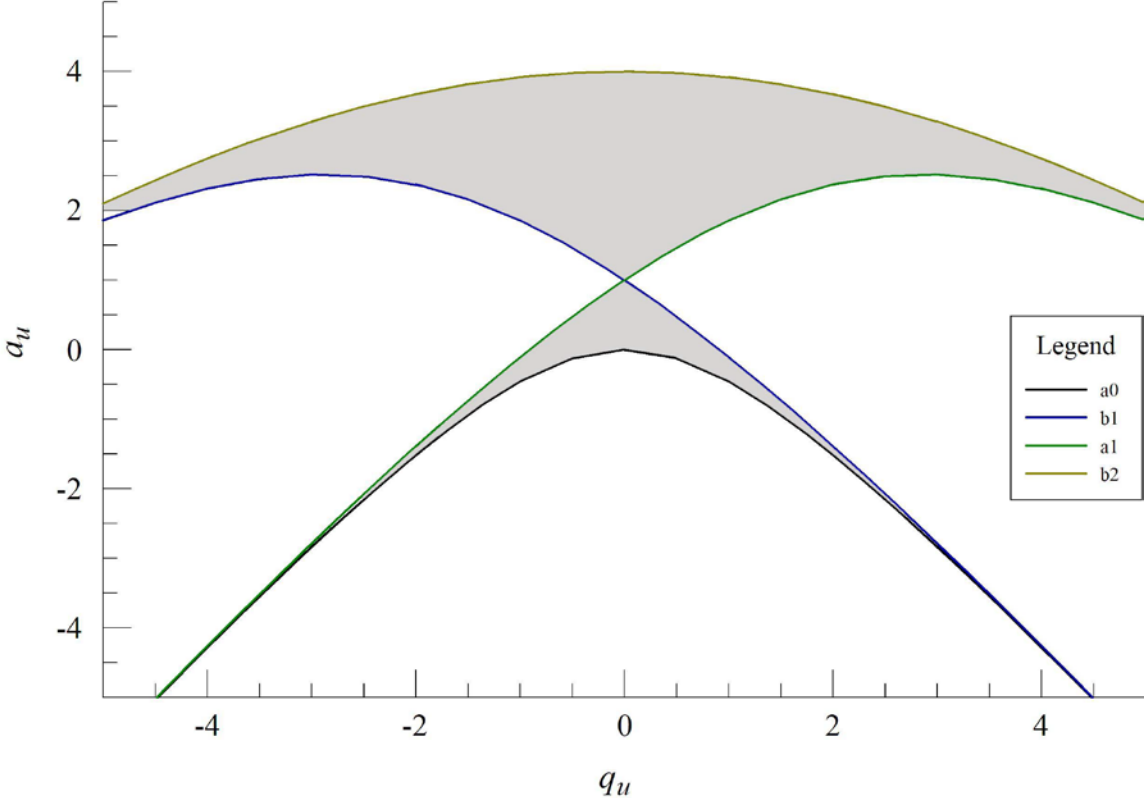


FIG. 4—*Stability diagram for the first (lower) and second (upper) stability regions (shaded in gray) in one dimension.*

In Eq. (2.27) and (2.28), as indicated by the final term in both equations, the polynomial is only a simple approximation of the boundary values. During the early decades after Mathieu first proposed the differential equation, the only way to approach the solutions were through brute force analytical methods. This has given way to far more accurate approximations through the use of matrix methods based on phase space dynamics (9) and higher order Runge-Kutta methods (16, 17). However, in order to provide insight into underlying mathematics of the solutions and shed light on the potential uses of Mathieu’s Equation, research still persists on ways to simplify the more rudimentary methods of integration (18). In any event, simple approximations will suffice for demonstrative purposes concerning the boundary values.

In addition to the boundary value approximations, there exists an exact solution to the non-integer values of the stability regions (referred to as β_u). However, the solution (a self-referential continued-fraction expression), requires an initial value of β_u to begin the expression:

$$\beta_u = \frac{a_u - \beta_u^2}{q_u + \frac{\beta_u^2 - 2\beta_u}{1 - \frac{a_u}{(\beta_u - 2)^2 - \frac{q_u^2}{((\beta_u - 2)^2(\beta_u - 4)^2)}}}} \quad (2.29)$$

where the initial value for β_u is

$$\beta_u = a_u - \frac{q^2(a_u - 1)}{2} \quad (2.30)$$

These can be seen compared to the boundary conditions in Fig 5.

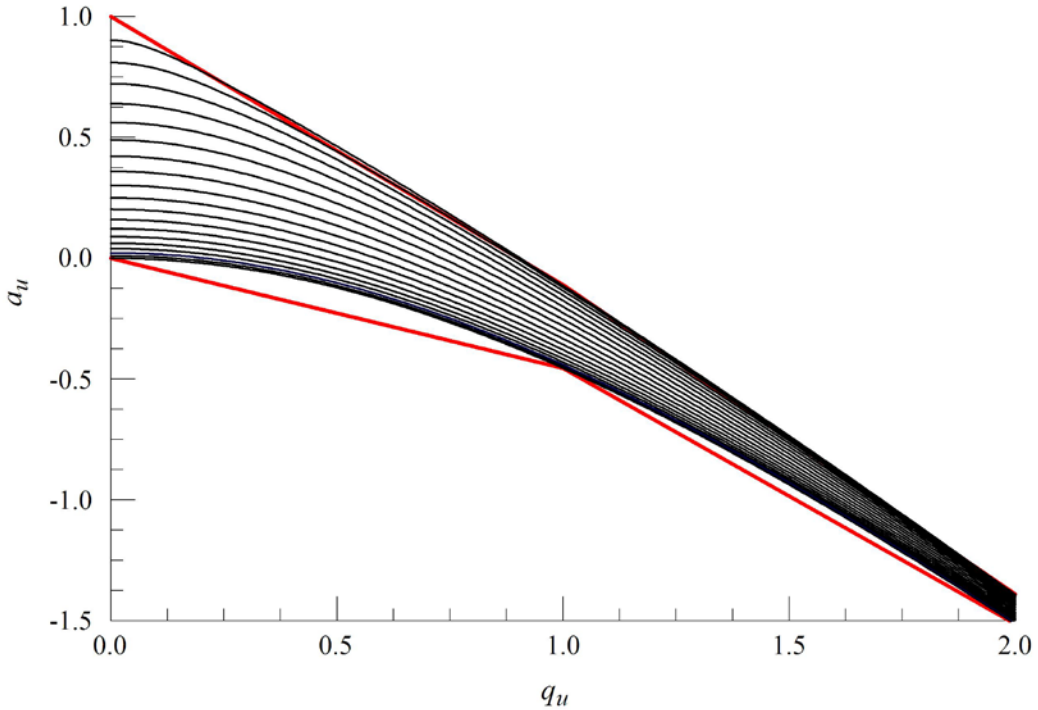


FIG. 5— β_u lines (black) compared with boundary lines (red).

Returning to our discussion of quadrupole theory, it will now be necessary to relate the dimensionless a_u and q_u space to one that has meaning for the purposes of quadrupole theory.

This can be accomplished by solving Eq. (2.26) for each value. Doing so yields

$$a_z = -\frac{16eU}{m(r_0^2 + 2z_0^2)\Omega^2} \quad (2.31)$$

and

$$q_z = -\frac{8eV}{m(r_0^2 + 2z_0^2)\Omega^2} \quad (2.32)$$

If the derivation were completed for the radial component of the equation (assuming a fixed z), the relationships would follow as

$$a_z = -2a_r \quad (2.33)$$

and

$$q_z = -2q_r \quad (2.34)$$

These also arise from the choice of values in Eq. (2.10)

Because both physical trap dimensions appear in Eq. (2.31) and (2.32), it is worth noting that early work on ion traps established that the relationship

$$r_0^2 = 2z_0^2 \quad (2.35)$$

provides the best quadrupolar distribution (19) and volume of stability (20), and thus when referring to trap dimensions, they are usually referenced in terms of r_0 .

We now have expressions relating the stability regions in a_u and q_u space to meaningful values pertaining to the operation of an ion trap. A graphical representation of the first stability region in both the axial and radial direction in terms of the AC (U) and DC (V) amplitudes can be seen in Fig 6. The asymmetry about the horizontal axis results from the solution to the Laplace Equation in (2.10) and from the derivation of the stability terms in Eq. (2.31) and (2.32).

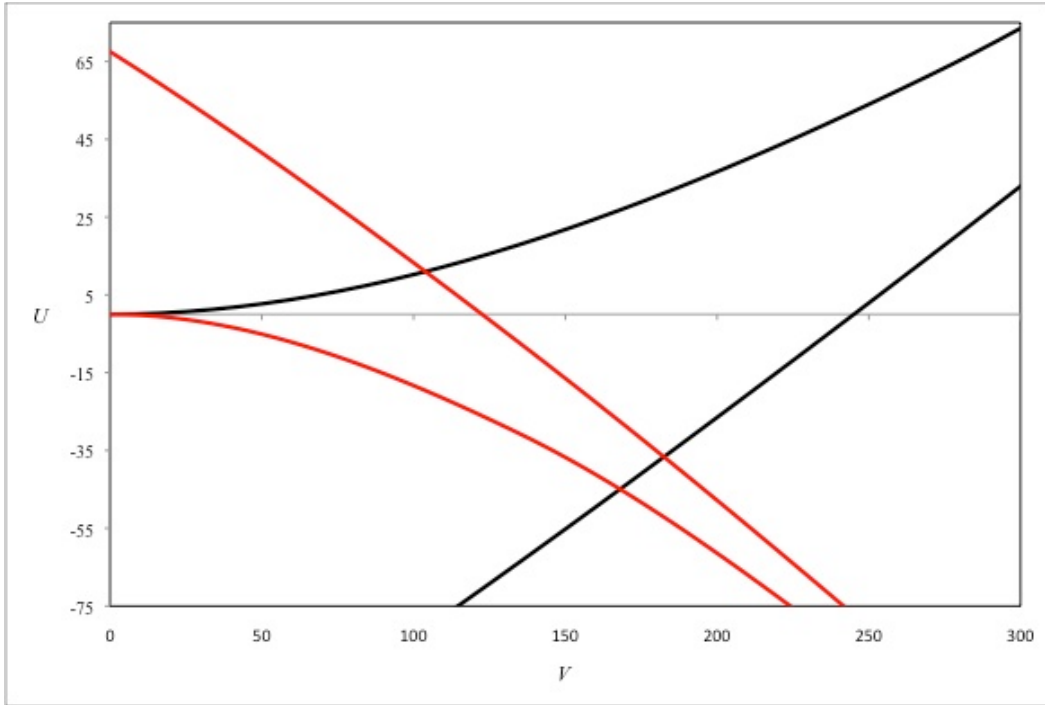


FIG. 6—First stability region for a quadrupolar ion trap in the axial (red) and radial (black) dimensions.

Now, the operation of ion trapping and ejection from the trap come into focus. For an RF only instrument (no DC offset applied radially), a low-amplitude RF voltage is applied to the trapping electrode. This low amplitude is selected such that it intersects with the stability regions of a broad mass range. After a time, the amplitude is increased in a linear fashion, such that as it approaches the limits of a single mass stability region, those ions are ejected from the trap. As a simple thought experiment, consider an ion trap, with $r_0=0.5$ mm, an RF frequency of 6.5 MHz and populated with singly-charged ions. The RF amplitude in which they will be ejected from the trap can be seen in Fig 7.

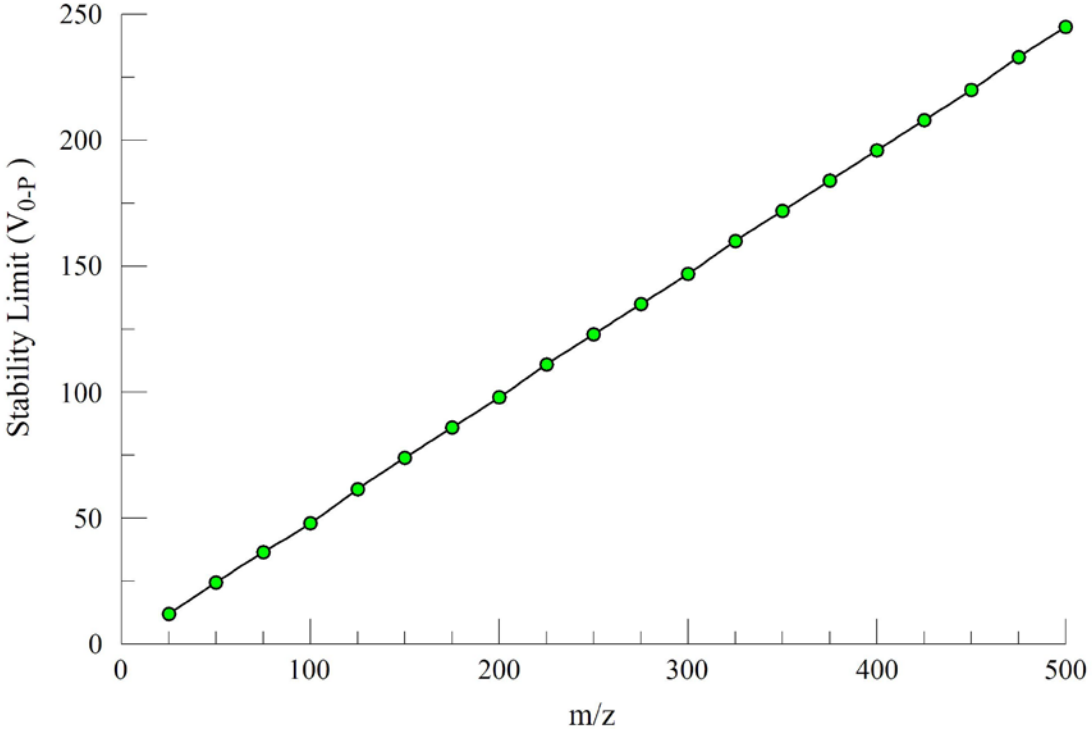


FIG. 7—*Stability limits for an $r_0=0.5$ mm ion trap running RF-only at 6.5 MHz as a function of mass.*

The various factors that are considered in Eq. (2.31) and (2.31) are intimately connected to the overall performance of an ion trap and must be considered when designing instrumentation such that mass range and power requirements are balanced in a desired fashion. Consider the same hypothetical trap mentioned above, but vary r_0 (Fig 8). While increasing trap volume also increases the volume of the stability region, the zero-to-peak voltage necessary for the ejection of a 250 m/z ion. A similar relationship can be seen in Fig 9 where the trapping frequency is varied. Physical limitations in power limit the upper end of the mass range for a given trap, and the reduced stability volume and low RF voltage near the origin of the diagram limit low-mass ion retention. Thus, a necessary balance must be found for optimal performance.

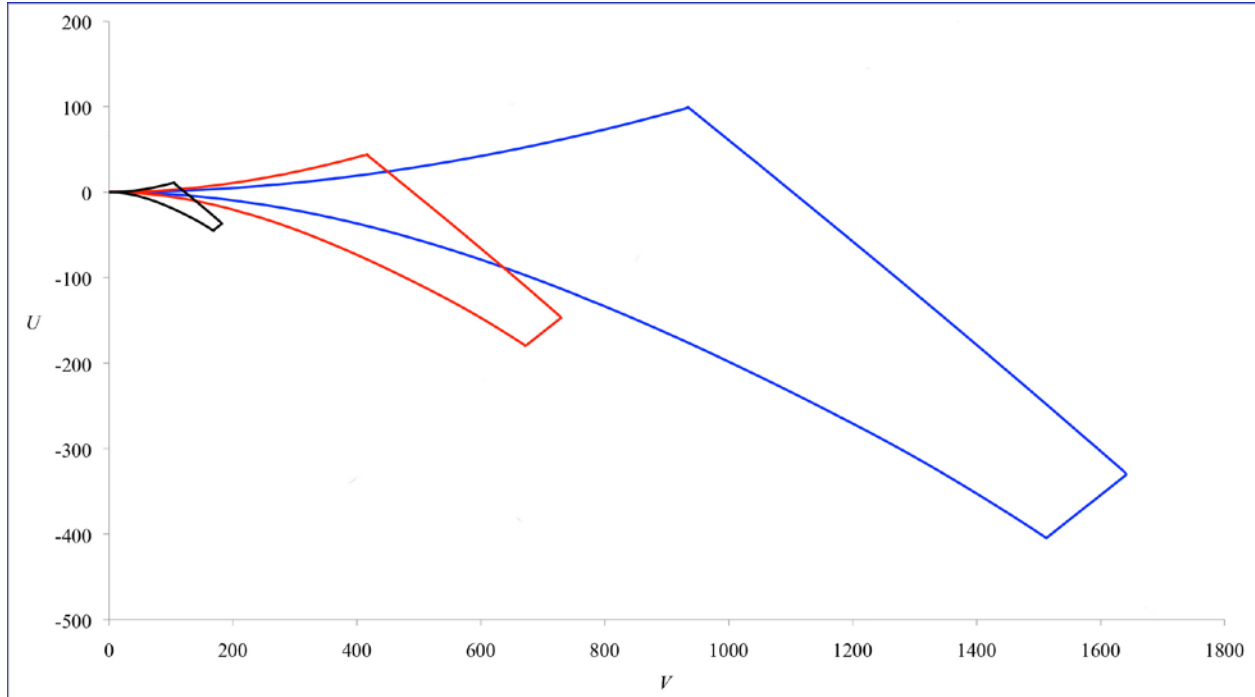


FIG. 8—*Stability regions for an ion trap with a 6.5 MHz trapping frequency and an r_0 of 0.5 mm (black), 1.0 mm (red) and 1.5 mm (blue). Regions of one-dimensional stability have been omitted for clarity.*

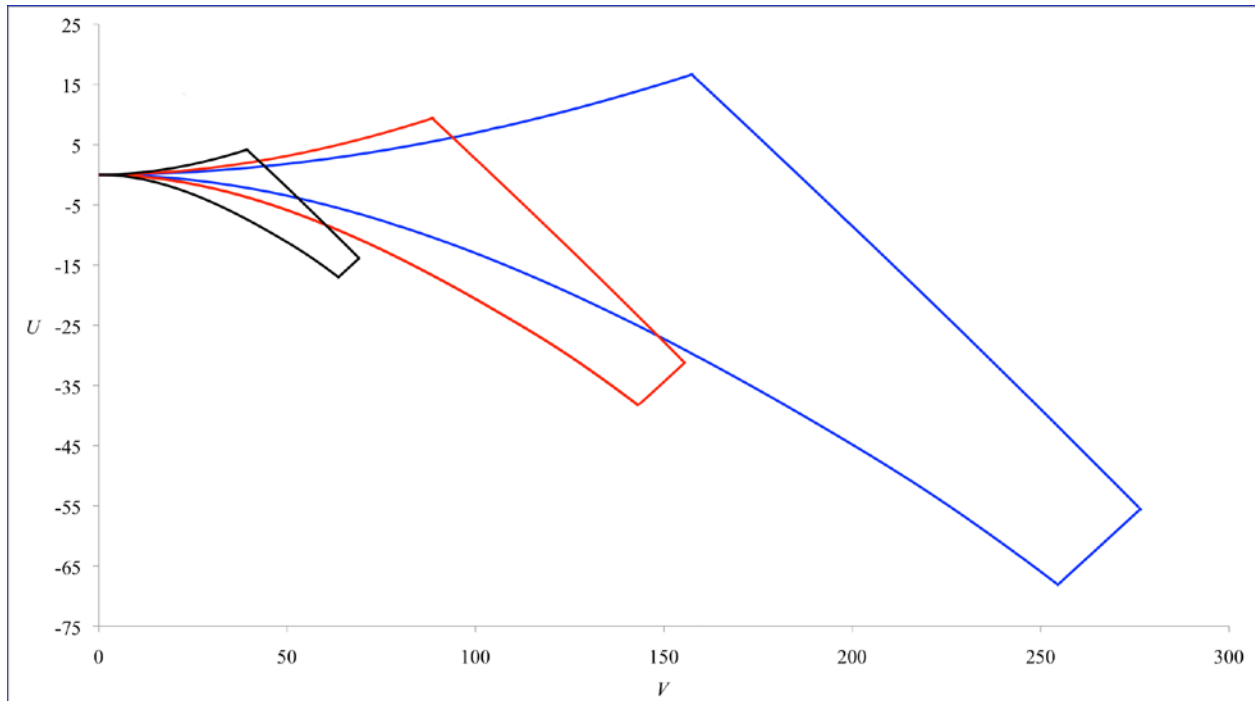


FIG. 9—*Stability regions for an $r_0=0.5$ mm ion trap using a trapping frequency of 4.0 MHz (black), 6.0 MHz (red) and 8.0 MHz (blue).*

This chapter has provided a brief primer on the underlying theory of quadrupole ion traps and their operation and is a necessary foundation on which to build practical experience. The application of these principals will be addressed in the following chapter, detailing the design and construction of such an instrument.

2.4 References

1. Mathieu É. Mémoire sur le mouvement vibratoire d'une membrane de forme elliptique. *J Math Pure Appl.* 1868;13:137-203.
2. McLachlan NW. Theory and Applications of Mathieu Functions. Oxford: Oxford University Press, 1964.
3. Paul W, Steinwedel H. Ein neues Massenspektrometer ohne Magnetfeld. *Zeitschrift für Naturforschung A.* 1953;8(7):448-50.
4. Paul W. Electromagnetic traps for charged and neutral particles. *Reviews of Modern Physics.* 1990;62(3):531-40.
5. Dehmelt HG. Radiofrequency Spectroscopy of Stored Ions I: Storage. In: Bates DR, Immanuel E, editors. *Advances in Atomic and Molecular Physics*: Academic Press; 1968;53-72.
6. Dehmelt HG. Radiofrequency Spectroscopy of Stored Ions II: Spectroscopy. In: Bates DR, Immanuel E, editors. *Advances in Atomic and Molecular Physics*: Academic Press; 1969;109-54.
7. Louris JN, Cooks RG, Syka JEP, Kelley PE, Stafford GC, Todd JFJ. Instrumentation, applications, and energy deposition in quadrupole ion-trap tandem mass spectrometry. *Analytical Chemistry.* [doi: 10.1021/ac00140a021]. 1987 1987/07/01;59(13):1677-85.
8. Stafford Jr GC, Kelley PE, Syka JEP, Reynolds WE, Todd JFJ. Recent improvements in and analytical applications of advanced ion trap technology. *International Journal of Mass Spectrometry and Ion Processes.* 1984;60(1):85-98.
9. Quadrupole mass spectrometry and its applications / Peter H. Dawson, editor. Amsterdam : New York: Elsevier Scientific Pub. Co. ; distributor for the U.S. and Canada, Elsevier/North-Holland, 1976.
10. Campana JE. Elementary theory of the quadrupole mass filter. *International Journal of Mass Spectrometry and Ion Physics.* 1980;33(2):101-17.

11. Dawson PH, Whetten NR. Ion Storage in Three-Dimensional, Rotationally Symmetric, Quadrupole Fields. I. Theoretical Treatment. *Journal of Vacuum Science and Technology*. 1968;5(1):1-10.
12. Dawson PH, Whetten NR. Ion Storage in Three-Dimensional, Rotationally Symmetric, Quadrupole Fields. II. A Sensitive Mass Spectrometer. *Journal of Vacuum Science and Technology*. 1968;5(1):11-8.
13. March RE. An Introduction to Quadrupole Ion Trap Mass Spectrometry. *J Mass Spectrom*. 1997;32(4):351-69.
14. March RE, Hughes RJ, Todd JFJ. *Quadrupole Storage Mass Spectrometry*: Wiley, 1989.
15. March RE, Todd JF. *Quadrupole Ion Trap Mass Spectrometry*. 2nd ed: Wiley, 2005.
16. Noshad H, Doroudi A. Computation of five stability regions in a quadrupole ion trap using the fifth-order Runge-Kutta method. *Int J Mass Spectrom*. 2009 Mar 15;281(1-2):79-81.
17. Noshad H, Kariman BS. Numerical investigation of stability regions in a cylindrical ion trap. *Int J Mass Spectrom*. 2011 Nov 1;308(1):109-13.
18. Frenkel D, Portugal R. Algebraic methods to compute Mathieu functions. *J Phys a-Math Gen*. 2001 May 4;34(17):3541-51.
19. Wuerker RF, Shelton H, Langmuir RV. Electrodynamic Containment of Charged Particles. *Journal of Applied Physics*. 1959;30(3):342-9.
20. Benilan M-NI, Audoin C. Confinement d'ions par un champ Electrique de radio-fquence dans une cage cylindrique. *International Journal of Mass Spectrometry and Ion Physics*. 1973;11(5):421-32.

CHAPTER 3

DESIGN AND DEVELOPMENT OF A MINITURE CYLINDRICAL ION TRAP

3.1 Introduction

In the past decade, much attention has been given to the miniaturization and ruggedization of analytical instrumentation in the effort to develop field-portable devices for real-time sampling and analysis (1). Mass spectrometry has been a major area of interest in this recent trend for its potential use in a number of applications ranging from environmental monitoring (2) to chemical weapons detection (3, 4). Miniaturization carries benefits conducive to portability such as reduced power requirements and simplification of the vacuum systems, e.g., via the use of chemical getter pumps. To date, a number of lab groups have had success in developing miniature instruments, including a sub-millimeter cylindrical ion trap (CIT) capable of collision induced dissociation and MSⁿ experiments (5), a portable rectilinear ion trap (6), a small toroidal ion trap (7), a coaxial ring ion trap (8) and a miniature time of flight (TOF) mass spectrometer (9).

Recalling the discussion in CHAPTER 1, the two greatest challenges in miniaturizing mass analyzers resolution and ion retention. Looking at the general equations for resolution in Eq. (1.1-4), and the expression for the depth of the pseudopotential well in Eq. (1.5) (10), it becomes clear the quadrupole ion trap is the only mass analyzer whose resolution may benefit from decreasing physical dimensions. However, this gain in resolution is offset by the loss in ion capacity as seen in Eq. (1.7) (11). It is also pertinent to point out that in order to maintain the same mass range, the frequency of the trapping voltage must also be increased (as discussed in CHAPTER 2). This also acts to offset the potential gains in resolution seen in the

aforementioned equations. The solution to this issue has been explored through the means of trap arraying (12-16). It is also worth noting that miniaturization of the trap allows the analyzer to be operated at elevated pressures while gaining or maintaining signal intensity (17) Thus, it can be seen that optimization of the miniaturized ion trap is a complex process, involving numerous factors in the trap's operation.

Looking at the other mass analyzers, it can be seen that the TOF and linear quad are both length dependent and therefore somewhat more difficult to miniaturize than the QIT while retaining resolution. A reflectron (18, 19) TOF has been proposed to lengthen the TOF in a more space-efficient manner (20). The CIT is easier to fabricate than hyperbolic ion traps (12), and as surface defects and abnormalities become increasingly problematic during miniaturization, ease of manufacturing must be considered. Also, when arraying multiple CITs, simple structures such as a cylinder versus a hyperbolic surface are desired for consistency. This geometry can be manufactured with precision using silicone-on-insulator (SOI) deep reactive ion etching (DRIE) (8). A miniature CIT has the advantage of reduced power and voltage requirements as the trap size is decreased (21). Currently, the CIT is the most favorable choice for miniaturization due to its independence from the length parameter and potential for expanding analysis via MSⁿ experiments. This dissertation will discuss the design and implementation of such an ion trap as well as preliminary data and plans for a self-contained deployable unit.

3.2 Experimental

A cross section of the instrument can be seen in Fig 10. The 0.5 mm r_o CIT (V), endcaps (IV) and focusing lenses (III) were machined from stainless steel and housed in a cylindrical casing (I) machined from Vespel® (DuPont, Wilmington, DE). MACOR spacers (Corning Inc., Corning, NY) were used to position the electrodes appropriately and 0.025 mm Kapton film

(DuPont, Wilmington, DE) was used to insulate the ion trap from the 0.381 mm endcaps. Ionization was accomplished via an ES-526 yttria-coated iridium disc cathode (II) (Kimball Physics, Wilton, NH). Ion detection was accomplished using a custom channeltron electron multiplier with a gain of 3.3×10^7 (VI) (De Tech Inc., Palmer, MA). The RF voltage and amplitude modulation voltage for the mass-selective instability scan was generated using an arbitrary function generator (Tektronix, Beaverton, OR) and amplified using an AR broadband amplifier (Amplifier Research, Bothell, WA). The assembly was mounted to a 2.75" conflat flange and housed in four-way cross (MDC, Hayward, CA). Vacuum was maintained by an MDP turbomolecular pump (Alcatel, Hingham, MA) backed by a DS 302 rotary-vane pump (Varian, Palo Alto, CA), and pressure was monitored using a MicroPiraniTM vacuum gauge (MKS, Andover, MA). The typical base pressure for the chamber was approximately 10^{-6} torr. Data was collected using a Tektronix 3034B oscilloscope (Tektronix, Beaverton, OR).

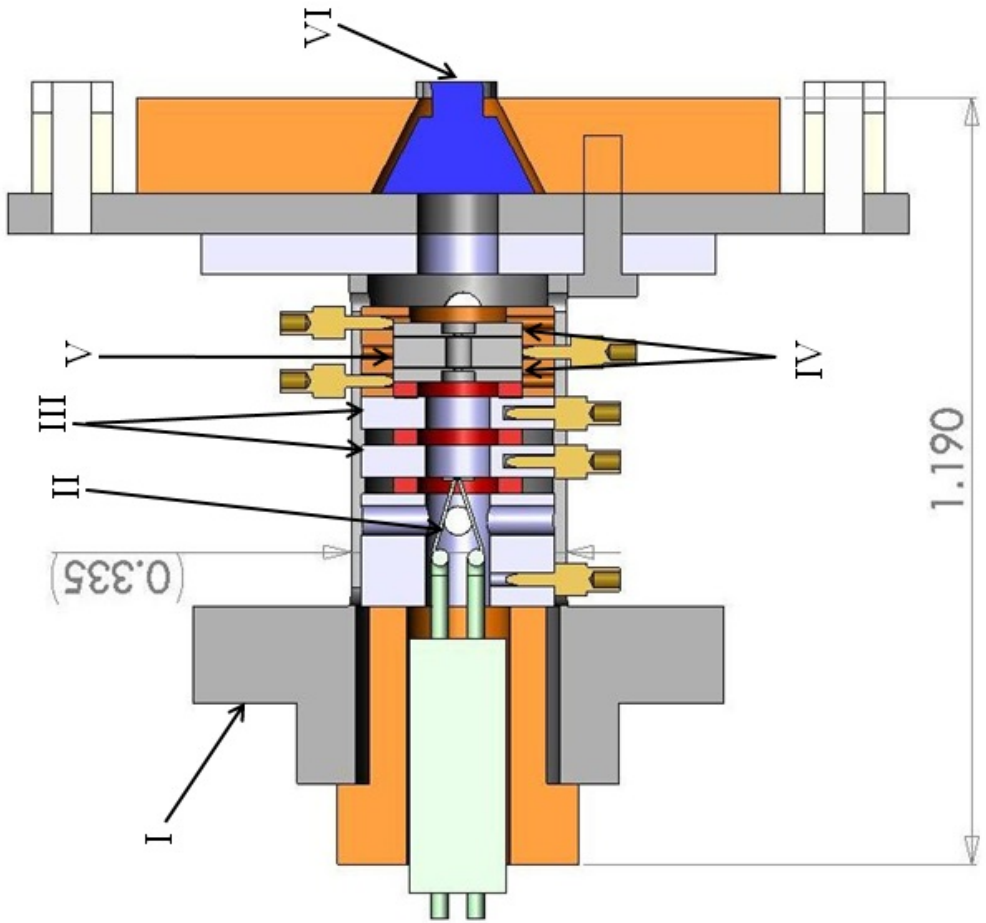


FIG. 10—*Cross sectional view of the miniature cylindrical ion trap: I) Vespel housing, II) filament, III) focusing lenses, IV) endcaps, V) trapping ring, VI) channeltron. Dimensions are listed in inches.*

The 0.5 mm r_0 ion trap was run at a trapping frequency of 4.3 MHz with an amplitude of 275 V_{0-p} and a 20 Hz repetition rate (similar to the condition see in Chapter 2, Fig 9 for 4.0 MHz). During each repetition, the ion source was opened and the trapping frequency was applied to the CIT for approximately 20 ms. Afterwards, the ion source was gated and the detector was brought to its operational voltage prior to and during the ejection sequence. The trap was calibrated using 1.0% SF₆ in helium (not shown), and the common SF₅⁺ and SF₃⁺ ions. For the initial experiments, the headspace of a liquid xylene sample was introduced to the vacuum chamber via a variable leak valve (MDC, Hayward, CA) until a pressure of approximately 10⁻⁴ torr was reached. Tests were performed to probe the isolation efficiency of the trap as a function of time, which was accomplished by modulating the amplitude of the RF voltage to eject ions with mass-to-charge ratios greater and lower than the singly charged xylene ions. Ion ejection during detection was accomplished by increasing the amplitude of the RF voltage in a normal mass-selective instability scan.

After isolation, collision-induced dissociation was accomplished by applying a tickle voltage to the endcaps to increase collision energy and fragmentation by increasing the depth of the potential well in the trap. In the first experiment, the voltage on the endcaps was held at 1 V and the time for CID was varied between 2 and 10 ms. In the second experiment, the isolation time was held constant, 10 ms, while the endcap voltage was varied between 0-1 V, in 100 mV increments, in order to examine the effect of CID voltage on ion signal. Data was collected, isolating the 106 m/z precursor ion and monitoring the range of 88-93 m/z for the 91 m/z product ion.

3.3 Results and Discussion

The mass spectra of the isolated xylene ions can be seen in Fig 11. The molecular ion peak at $106\text{ }m/z$ is most prominent, followed by the $[\text{M}+\text{H}]^+$ and $[\text{M}-\text{H}]^+$ ion peaks at 107 and $105\text{ }m/z$ respectively. As the isolation time increases, the total ion signal from the trap decreases as more xylene ions are lost during the trapping event (as seen in Fig 12).

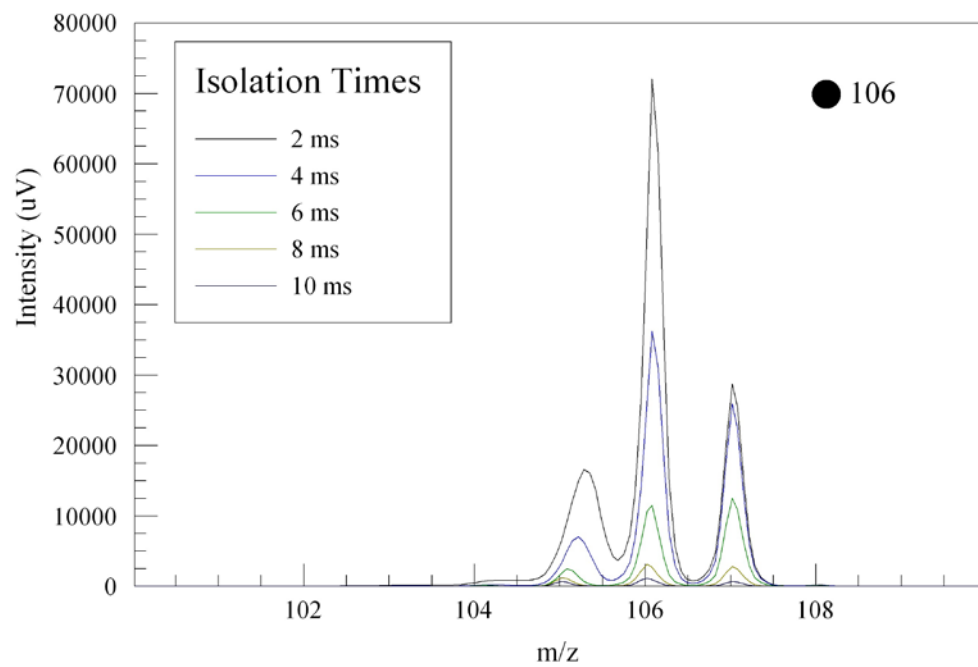


FIG. 11—*Mass spectra of xylene product ions (105, 106, 107 m/z) versus absolute intensity (uV) for isolation times at 2, 4, 6, 8 and 10 ms.*

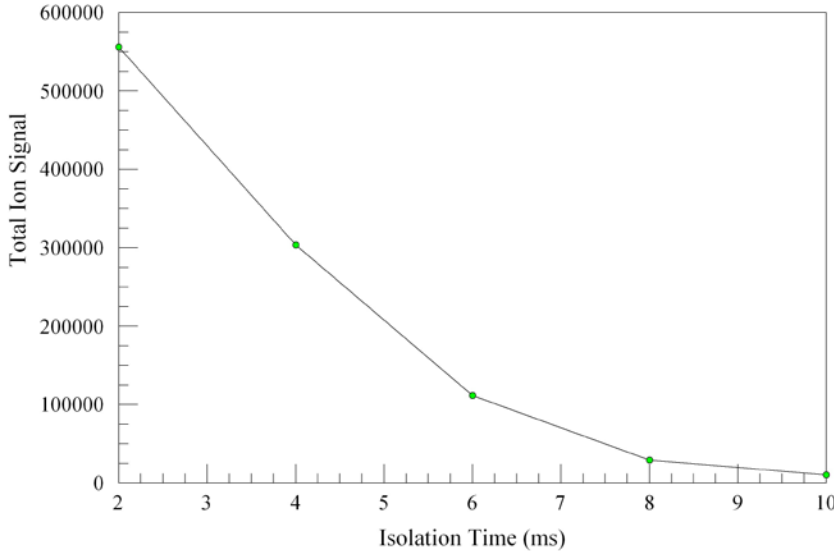


FIG. 12—*Integrated ion signal for xylene at different isolation times.*

The CID spectra of xylene as a function of collision time can be seen in Fig 13. Here, the loss of a methyl group from the ring is apparent from the prominent peak at $91\text{ }m/z$. Collision time plays a significant role in the retention of ions in the trap. This is evidenced by the large reductions in the integrated signal between 3-4 ms and 4-5 ms (Fig 14). After 6 ms, the signal is reduced to less than a tenth of its original intensity. The temperature of the product ions becomes significant so that the narrow well of the 0.5 mm r_0 ion trap and linear dampening cannot hold an appreciable amount of ions in the trap.

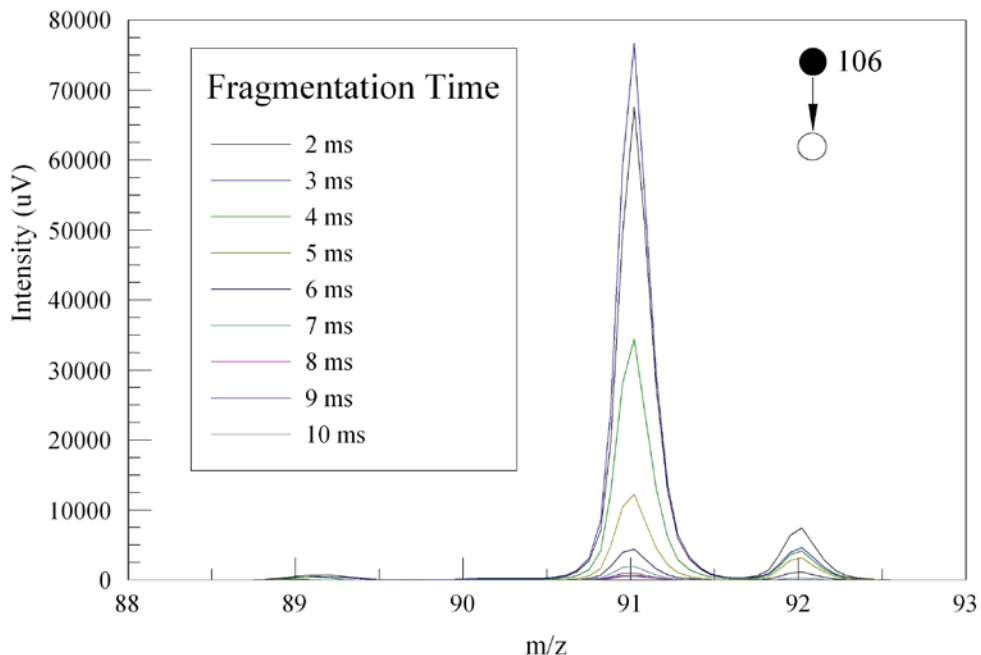


FIG. 13—*Mass spectra of xylene product ions (91, 92 m/z) versus absolute intensity (uV) for CID times at 2-10 ms at 1 V.*

Fig 15 shows the CID spectra of xylene with different tickle voltages applied to the end caps. No significant signal loss is observed until the endcap voltages exceed 400 mV (Fig 16). This will increase further product ions, requiring a lower q to see. However, lowering the q will lead to even more ion losses.

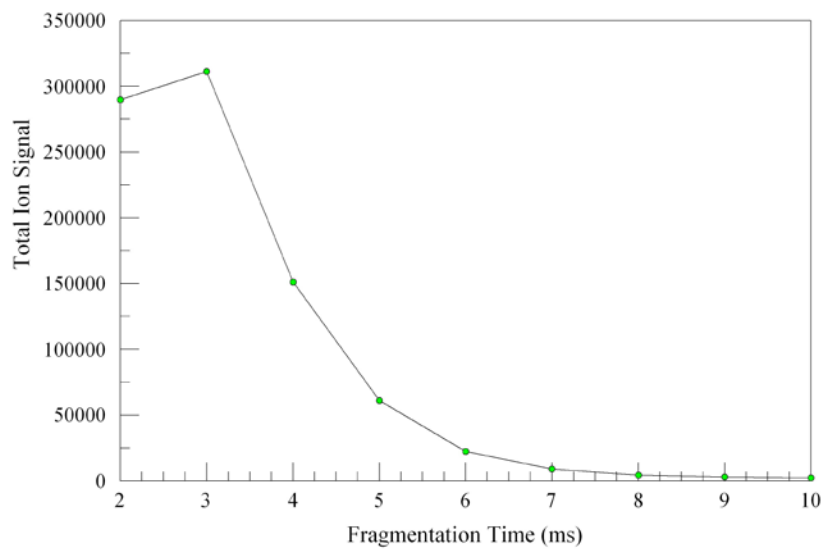


FIG. 14—Integrated signals from the mass spectra of xylene with incrementally longer CID times.

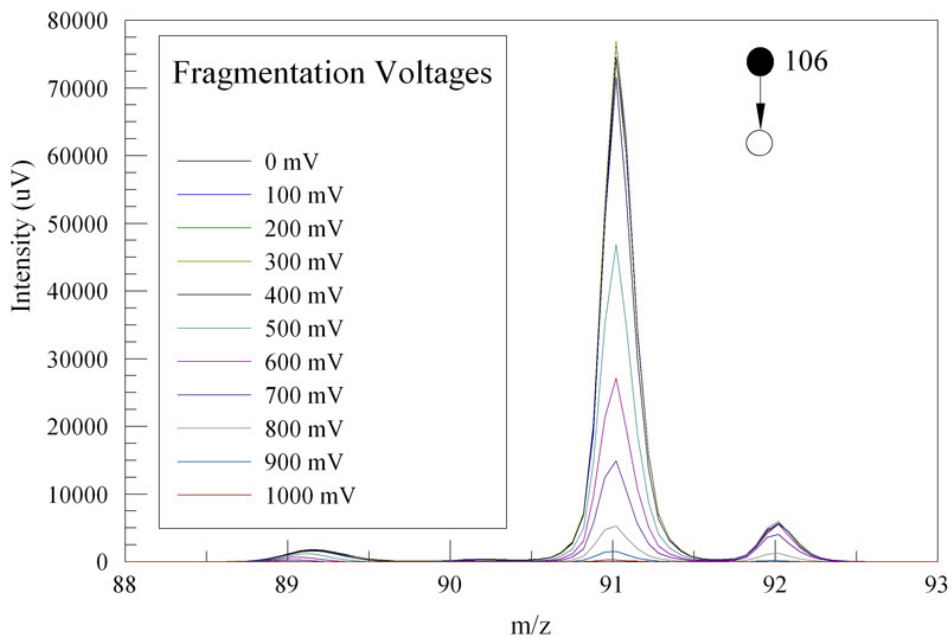


FIG. 15—Mass spectra of xylene product ions ($91, 92\text{ m/z}$) versus absolute intensity (μV) at 0-1 V of CID energy at 10 ms CID time.

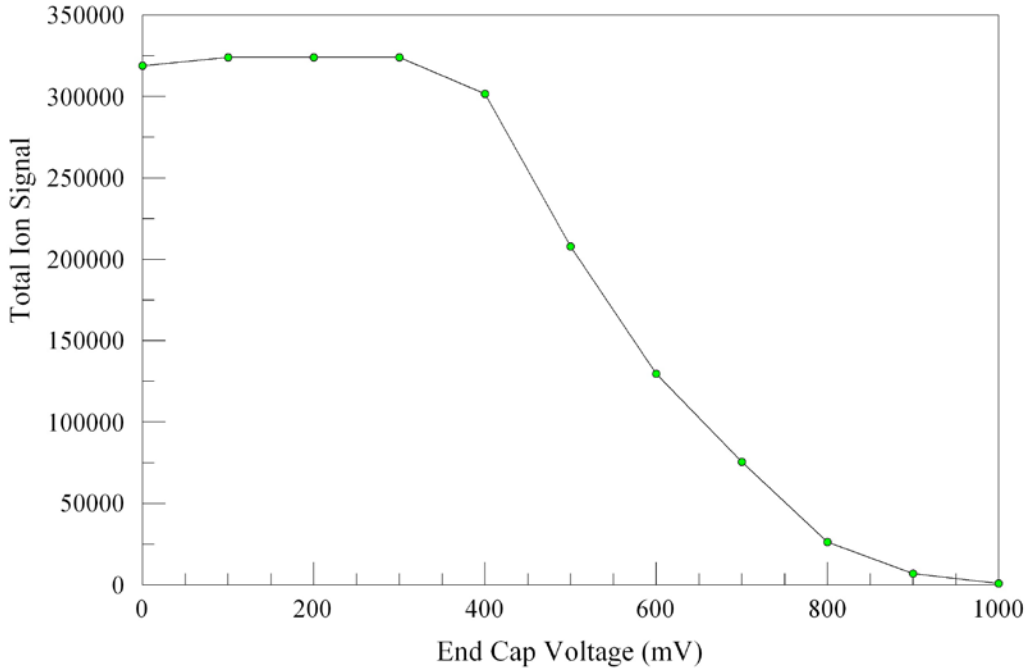


FIG. 16—*Integrated signals from the mass spectra of xylene at different CID voltages.*

The parameters that affect ion retention during CID have distinct windows in the fragmentation time and voltage in which the signal is maximized and produces spectra. While these experiments use a tickle voltage on the endcaps, other lab groups have worked with resonance ejection, where a resonant AC voltage is applied to one of the endcaps to achieve CID (22). Such an AC voltage can yield significant increases in mass resolution, but greatly complicates the electronics needed to miniaturize.

As previously mentioned, fabricating a large array of micro-scaled cylindrical ion traps has the potential to significantly increase signal strength, showing the most promise for the development of a ruggedized, field deployable instrument. Alignment is the biggest hurdle to overcome in the fabrications of CIT arrays. It is possible that multichannel detector and algorithm could be used to alleviate this problem. Next to alignment, the quality of the trap walls is also of concern; imperfections can cause aberrations in the field lines, which can be detrimental to the operation of the traps. SOI DRIE has become a method of choice for

fabricating micrometer-scale devices while minimizing surface defects (23, 24). This process, and others like it, will be key in future instrumental development.

3.5 References

1. Badman ER, Cooks RG. Special feature: Perspective - Miniature mass analyzers. *J Mass Spectrom.* 2000 Jun;35(6):659-71.
2. Arkin CR, Griffin TP, Diaz JA, Follistein DW, Curley CH, Floyd DP, et al. A small mass spectrometer system for in situ gas analysis. *Trac-Trend Anal Chem.* 2004 Apr;23(4):322-30.
3. Cotte-Rodriguez I, Handberg E, Noll RJ, Kilgour DPA, Cooks RG. Improved detection of low vapor pressure compounds in air by serial combination of single-sided membrane introduction with fiber introduction mass spectrometry (SS-MIMS-FIMS). *Analyst.* 2005;130(5):679-86.
4. Chen HW, Xu RF, Chen H, Cooks RG, Ouyang Z. Ion/molecule reactions in a miniature RIT mass spectrometer. *J Mass Spectrom.* 2005 Nov;40(11):1403-11.
5. Moxom J, Reilly PTA, Whitten WB, Ramsey M. Analysis of volatile organic compounds in air with a micro ion trap mass analyzer. *Anal Chem.* 2003 Aug 1;75(15):3739-43.
6. Gao L, Song QY, Patterson GE, Cooks RG, Ouyang Z. Handheld rectilinear ion trap mass spectrometer. *Anal Chem.* 2006 Sep 1;78(17):5994-6002.
7. Lammert SA, Rockwood AA, Wang M, Lee ML, Lee ED, Tolley SE, et al. Miniature toroidal radio frequency ion trap mass analyzer. *J Am Soc Mass Spectr.* 2006 Jul;17(7):916-22.
8. Fox J, Saini R, Tsui K, Verbeck G. Microelectromechanical system assembled ion optics: An advance to miniaturization and assembly of electron and ion optics. *Rev Sci Instrum.* 2009 Sep;80(9):-.
9. Brinckerhoff WB, Cornish TJ, McEntire RW, Cheng AF, Benson RC. Miniature time-of-flight mass spectrometers for in situ composition studies. *Acta Astronaut.* 2003 Jan-Mar;52(2-6):397-404.
10. Dawson PH. *Quadrupole Mass Spectrometry and Its Applications.* 2nd ed. New York: American Institute of Physics, 1995.
11. Benilan MN, Audoin C. *Int J Mass Spectrom.* 1973;7:421-32.
12. Badman ER, Cooks RG. Cylindrical ion trap array with mass selection by variation in trap dimensions. *Analytical Chemistry.* 2000 Oct 15;72(20):5079-86.

13. Cruz D, Chang JP, Fico M, Guymon AJ, Austin DE, Blain MG. Design, microfabrication, and analysis of micrometer-sized cylindrical ion trap arrays. *Rev Sci Instrum.* 2007 Jan;78(1):-.
14. Pau S, Pai CS, Low YL, Moxom J, Reilly PTA, Whitten WB, et al. Microfabricated quadrupole ion trap for mass spectrometer applications. *Phys Rev Lett.* 2006 Mar 31;96(12):-.
15. Chaudhary A, van Amerom FH, Short R, Bhansali S. Fabrication and testing of a miniature cylindrical ion trap mass spectrometer constructed from low temperature co-fired ceramics. *Int J Mass Spectrom.* 2006;251(1):32-9.
16. Van Amerom FH, Chaudhary A, Cardenas M, Bumgarner J, Short RT. Microfabrication of cylindrical ion trap mass spectrometer arrays for handheld chemical analyzers. *Chemical Engineering Communications.* 2007;195(2):98-114.
17. Moxom J, Reilly PTA, Whitten WB, Ramsey JM. Sample pressure effects in a micro ion trap mass spectrometer. *Rapid Commun Mass Sp.* 2004;18(6):721-3.
18. Gohl W, Kutscher R, Laue HJ, Wollnik H. *International Journal of Mass Spectrometry and Ion Physics.* 1983;14:411.
19. Mamyrin BA, Karatev VI, Shmikk DV, Zagulin VA. *Soviet Physics JETP.* 1973;37:45.
20. Cotter RJ, Fancher C, Cornish TJ. Miniaturized time-of-flight mass spectrometer for peptide and oligonucleotide analysis. *J Mass Spectrom.* 1999 Dec;34(12):1368-72.
21. Sokol E, Edwards KE, Qian K, Cooks RG. Rapid hydrocarbon analysis using a miniature rectilinear ion trap mass spectrometer. *Analyst.* 2008;133(8):1064-71.
22. Moxom J, Reilly PTA, Whitten WB, Ramsey JM. Double resonance ejection in a micro ion trap mass spectrometer. *Rapid Commun Mass Sp.* 2002;16(8):755-60.
23. Abdolvand R, Ayazi F. An advanced reactive ion etching process for very high aspect-ratio sub-micron wide trenches in silicon. *Sensor Actuat a-Phys.* 2008 May 28;144(1):109-16.
24. Yun SS, Jeong DH, Wang SM, Je CH, Lee ML, Hwang G, et al. Fabrication of morphological defect-free vertical electrodes using a (110) silicon-on-patterned-insulator process for micromachined capacitive inclinometers. *Journal of Micromechanics and Microengineering.* 2009 Mar;19(3):-.

CHAPTER 4

MEMS ASEMBLED ION OPTICS: AN ADVANCE TO MINIATURIZATION AND ASSEMBLY OF ELECTRON ION OPTICS

4.1 Introduction

Over the past six years, a large demand for microsensors has pushed the industry to start developing smaller instrument components. Among these components are small, low power ion sources such as field emitters which produce a high electron current with minimal power requirements. Due to current high-vacuum constraints, companies like MKS (Andover, MA), Air Squared (Broomfield, CO), Pfeiffer (Nashua, NH), Varian (Palo Alto, CA) and KNF Neuberger (Trenton, NJ) have produced portable low-vacuum roughing and high-vacuum turbo pumps, allowing mass spectrometric instruments to become smaller. Groups at Oak Ridge National Laboratory (1, 2), Brigham Young University (3, 4), Johns Hopkins (5, 6) and Purdue University (7, 8) have developed small mass selectors, such as the sub-millimeter ion trap, small toroidal ion trap, mini time of flight (TOF) and rectilinear ion trap mass spectrometers. Ion detection has also been made microscale with small channeltron (9) and microchannel plate (MCP) (10) detectors.

Recently, several methods have been utilized in the manufacturing of MEMS devices, a general schematic of which can be seen in Fig 17. The oldest and most familiar of these methods is wet chemical etching (11). This method has a broad range of applications and encompasses many different etchants and substrates. The effectiveness of this method in microfabrication is largely dependant on the ability of the etchant to

react with the substrate versus its ability to react with the masking or passivation layers.

Most etchants are isotropic, resulting in a nonselective etch that extends beneath masking layers (12). Those chemical agents and substrates that are considered to give anisotropic etches with this method still give rise to steeply angled sidewalls (13).

Inhomogeneity in etching leads to surface defects that can be detrimental to the functionality of MEMS optical components (Fig 18).

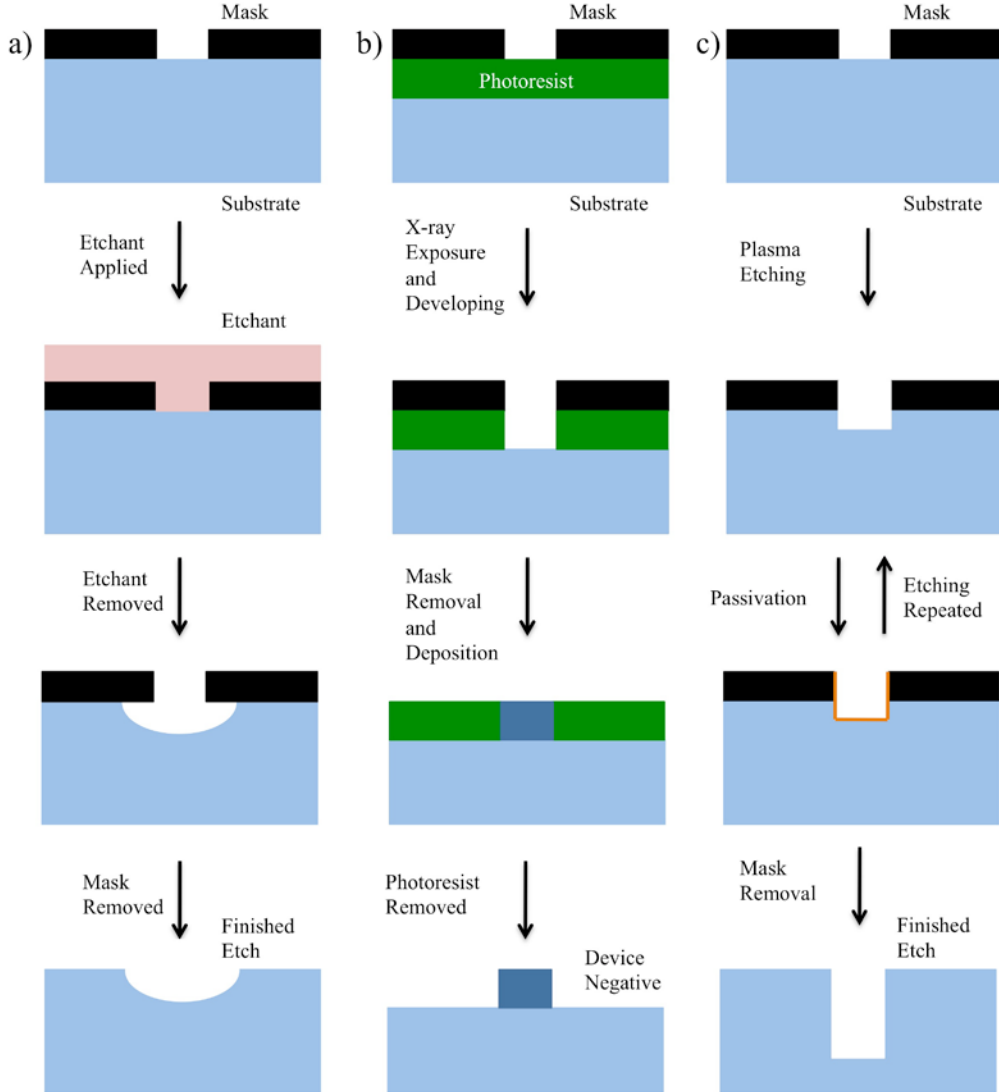


FIG. 17—*Schematic of a) wet chemical etching, b) LIGA and c) SIO-DRIE.*

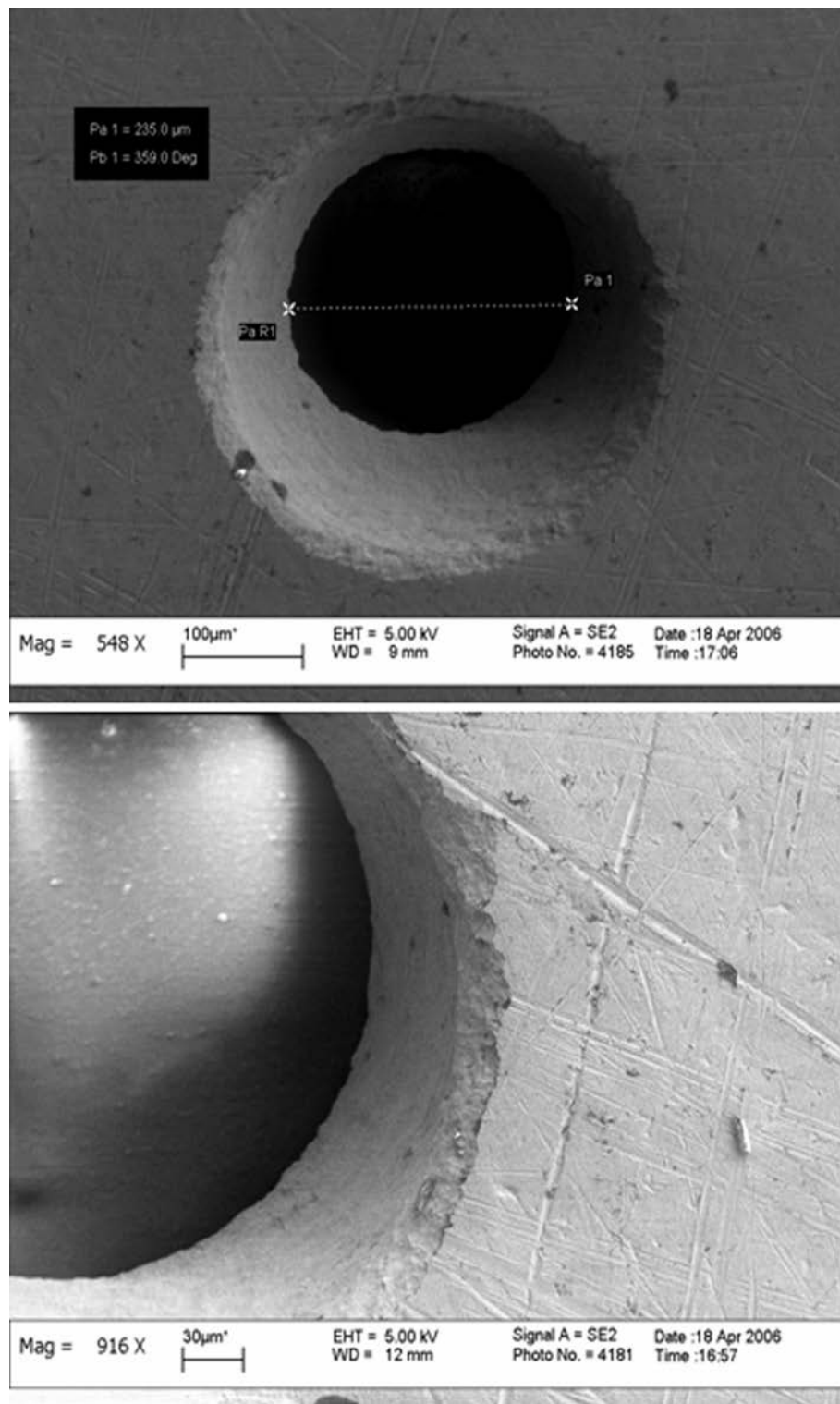


FIG. 18—SEM image of the 250 μm diameter ion trap developed using chemical etching processes. Surface aberrations, edge effects and taper of the wall are illustrated.

Another method is lithography, electroplating and molding, or “LIGA” (from the German phrase "Lithographie, Galvanoformung, Abformung,") (14), which is commonly seen as X-ray (15) and UV LIGA (16) (Fig 19). The process begins with the development of an intermediate mask that is used as a template on which the working mask is formed. This is accomplished by coating a substrate with a good X-ray absorbing material (in some cases, titanium), and a resist layer that can be altered via an electron gun. The electron gun is used to sketch the desired pattern onto the resist, which can then be removed with a chemical developer before electroplating with gold. This mask used as a template for lithography to be performed on the second resist-coated substrate. The process is repeated until a mask with the appropriate working depth is developed. The working mask is then used in the lithographic development of a structural negative. That negative is the form for the final product in the next electroplating process. Depending on the depth of the electroplating, the product can either be used as is, or as the molding for the mass production of a functional design. While LIGA produces structures with a considerable degree of precision (1.0 mm sidewall deviation per 1.0 mm structure height (17) and a 0.5 mm standard deviation in reproducibility (18)), the process involves numerous steps and can be quite complicated when producing microstructures that are to be assembled later into more complex devices.

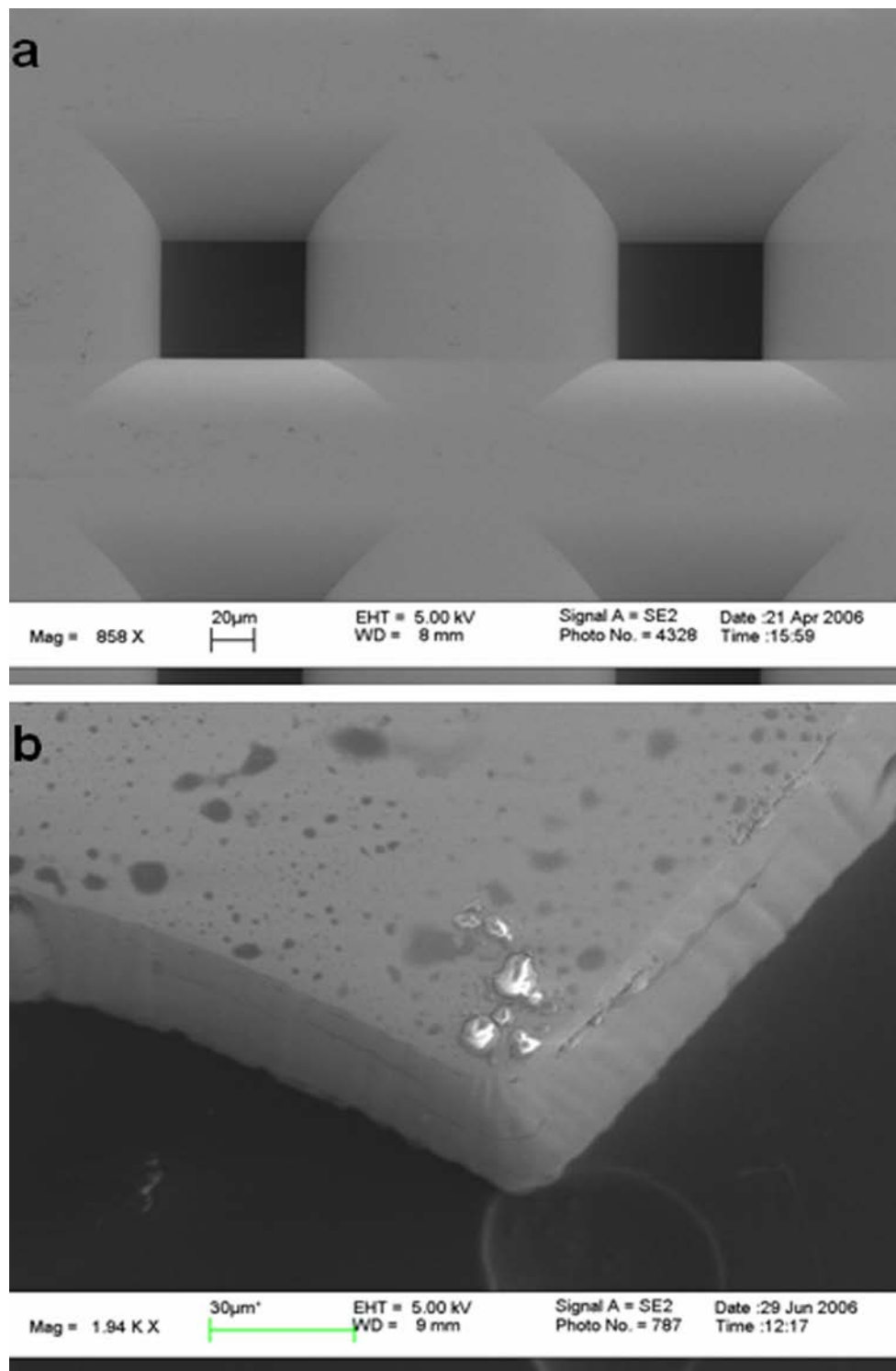


FIG. 19—SEM image of the ion trap arra developed using LIGA: (a) tapering of the sidewalls in the square channel array; (b) heavy scalloping and irregularities on the edge of the arra are shown.

A microfabrication method that has received much attention as of late is the deep-reactive ion etching (DRIE) of n-doped silicon-on-insulator (SOI). In this process, a silicon wafer, mounted on a buried oxide (BOX) layer, is used as the palette for design and fabrication. In work by Saini et al. (19, 20), the method begins by deep-reactive ion etching the top layer of the SOI and depositing a nitride layer to isolate each component to be fabricated. The etching process involves alternating steps of plasma etching and the deposition of a passivation layer. The passivation layer acts similarly to the resist used in LIGA, but reacts with the plasma that is directed onto it. Thus, as the etch depth increases, the passivation layer acts to protect the sidewalls, making DRIE a highly anisotropic process (21) (Fig 20). However, minute quantities of the passivation layer on the sidewalls are also destroyed during the plasma etching, leading to cyclic aberrations of only a few hundred nanometers, though recent improvements to the method have significantly reduced such defects (22, 23). The exact measure of these aberrations is proportional to the etch time, giving DRIE an advantage over LIGA (whose aberrations are proportional to etch depth). Once the palettes for the individual MEMS components are isolated, gold is deposited on the surface in the desired pattern, and then the top layer is etched until the oxide layer is reached. The back of the SOI wafer is then also etched according to the design of the structural side, and gold is deposited on the sidewalls to act as a conductor for the MEMS components. Finally, the oxide layer is partially dissolved using hydrofluoric acid, and the MEMS components can be extracted from (and even assembled on) the SOI wafer.

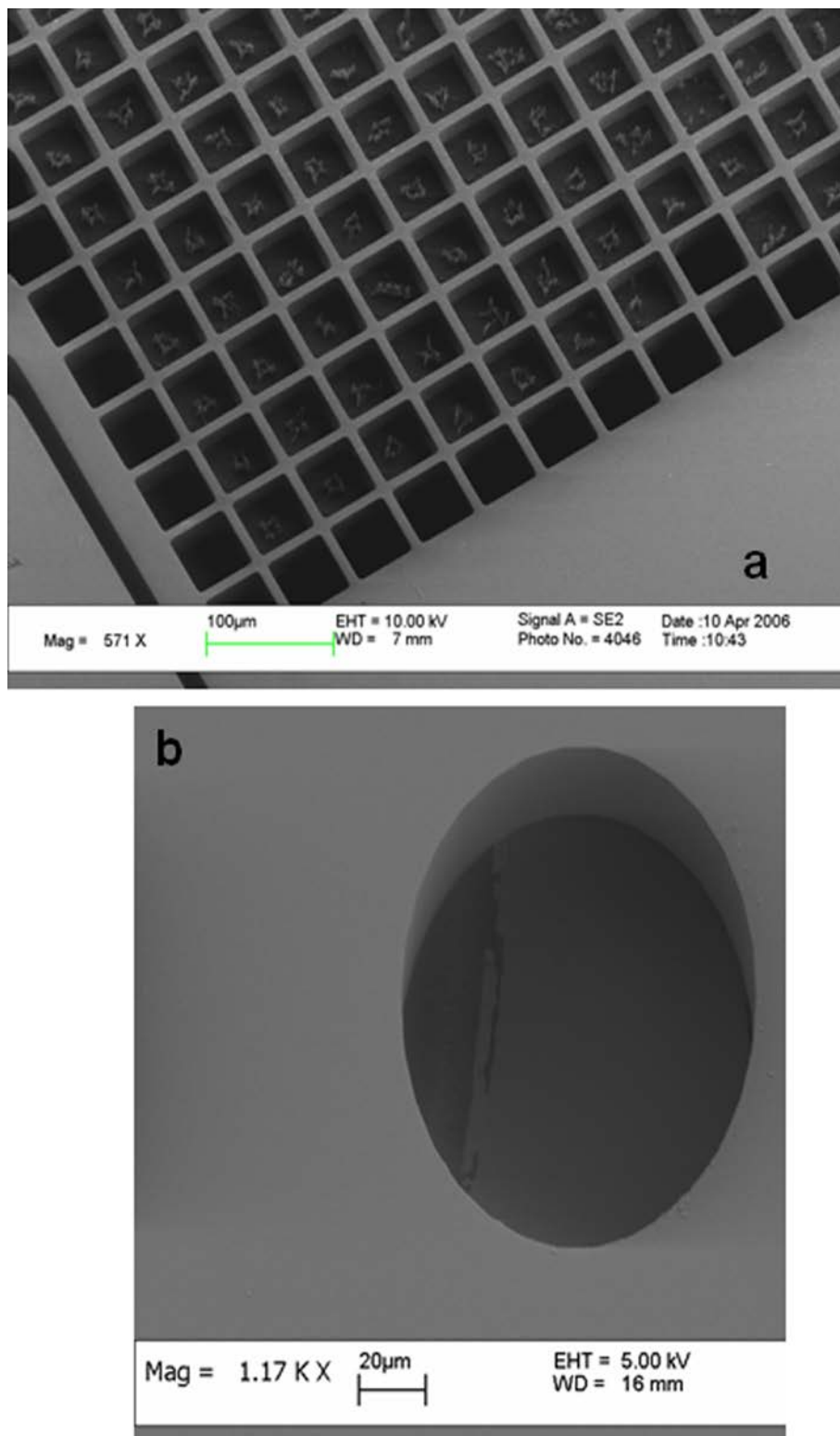


FIG. 20—SEM image of (a) the grid and (b) the cylindrical ion trap developed using the SOI DRIE process.

As the manufacturing processes have gradually become more refined, labs across the country have had success in developing miniature mass analyzers. This list includes Mike Ramsey and Bill Whitten developing the sub-millimeter cylindrical ion trap (24, 25), Graham Cooks and Griffin Analytical with the small rectilinear trap (26, 27), Milton Lee with the small toroidal ion trap (28), and Tim Cornish with the miniature TOF (29). Others are also trying to miniaturize the rotating-field MS and small sectors (30) with limited success. Because these devices show the most promise, we will focus on the problems that currently plague the quadrupoles, ion traps and TOFs.

Recall the discussion from CHAPTER 2 on resolution and ion attenuation: for ion traps, the max number of ions stored (N_{max}) is directly proportional to the depth of the pseudo-potential well (D_z) (31).

The reflectron (32, 33) has been proposed by our group and Cornish to increase the time-of-flight within a more confined space. On the other hand, the quadrupole ion trap (QIT) and cylindrical ion traps can have an increase in resolution within a miniature device and trapping time can be increased to increase resolution, but at the cost of attenuating the signal.

Due to the difficulties in the micromachining of ion optical components with small aberrations, it is necessary to incorporate new fabrication methods such as doped silicon MEMS. This technique allows for precise manufacturing of small ion optical components. Over the last six years, MEMS mass spectrometers have been at the forefront of portable mass spectrometry; linear quadrupoles (34), magnetic mass analyzers (35), rectilinear traps, cylindrical ion traps, and TOFs (36) are among the current list of microfabricated devices. Due to the overwhelming need by first responders,

the medical community, and environmentalists, an affordable precision mass analyzer is needed. Assembled MEMS would be an excellent way to bring all ion optical devices and vacuum components into a single, usable format for field portable mass spectrometers.

Recently, ion sources, mass analyzers, and detectors have been produced on a single MEMS package. The planar integrated miniature mass spectrometer (PIMMS) is one of the most recent mass sensors (37). Other planar etched mass analyzers based on the cylindrical ion trap array have also been developed (35, 38-40). These devices make use of the wafer's low defect surface, but are often confined to 2-D fabrication and are plagued with low resolution due to alignment errors and space-charge effects. Richard Syms' group has had success with 3-D assembly by utilizing the MEMS process to assemble small, well aligned linear quadrupole rods (41). The 3-D assembly has a marked advantage over the planar devices in that ion optics can be allowed to confine the ions and electrons in all directions. This helps eliminate losses and opens the door to better ion manipulation.

4.2 Experimental

The micromechanical ion optical components were fabricated using DRIE on highly n-doped (0.01 W-cm) SOI wafers with a 2.0 μm BOX later to form the micromechanical and electromechanical structures. The wafer were then diced and flip-chip bonded to an insulating substrate for components that operate at high voltages (>1 kV). An automated pick and place microassembly tool with MEMS end-effectors and high precision robotics was used to assemble the micro ion-optical devices. This assembly system provided a high degree of flexibility in terms of 3-D assembled

structures and assembly precision. Ion and electron-optical assemblies were tested for electrical breakdown from 760 to 1×10^{-7} torr. The mass spectrometers and ion lens assemblies were then tested for ion manipulation accuracy.

We designed, fabricated and tested four new MEMS based ion optical assemblies. This list included the Bradbury-Nielsen Gate, Coaxial Ring Ion Trap (Stacked Cylindrical Ion Trap), Reflectron Optics, and Einzel Lens.

The Bradbury-Nielsen gate was an ion optical switch that either allowed ions through the gate or steered them away with minimal potential difference between the alternating wires. Fig 21 shows the scanning electron microscope (SEM) image of the gate. The electrode wires were 10 μm in width with 50 μm spacing. This allowed an 80% transmission of the physical gate when the alternating potentials were set to the same value. The gate was mounted to an aluminum nitride pad with gold leads attached to the alternating sides. A 1 mm hole was drilled on the aft side for ion transmission. The Bradbury-Nielsen gate was positioned between a 70 eV electron source and a channeltron detector (Detector Technology, Inc, MA) set to amplify electron signal.

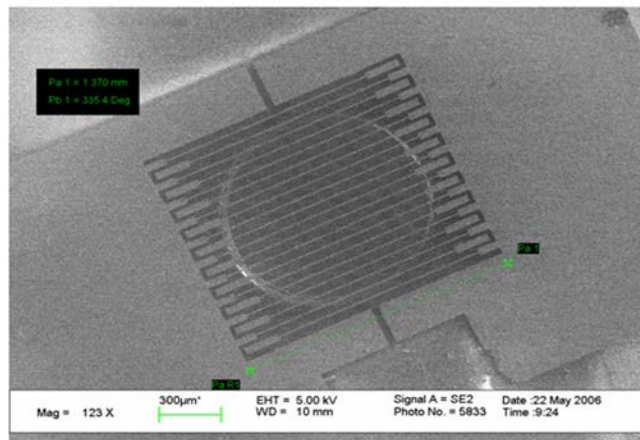


FIG. 21—SEM image of the Bradbury-Nelson Gate; electrode wires are 10 μm in width with 50 μm spacing.

The coaxial ring ion trap (CRITter) and reflectron optics were developed to produce mass selection ion optics and test the alignment capabilities of the fabrication process. Both devices (Figs 22 and 23) require critical tolerances to perform optimally. The coaxial ring ion trap consisted of five trapping rings with 500 μm i.d., and two endcaps with a 75 mm i.d. The rings had a thickness of 50 μm and were spaced 25 μm apart. The five trapping electrodes were electrically connected to apply the radio frequency (RF) trapping potential and the endcaps were electrically isolated and connected to ground. Ions were formed via electron impact (EI) at 70 eV within the trapping electrodes. Ions were ejected by ramping the $V_{\text{p-p}}$ at a constant frequency and were then collected by a channeltron detector.

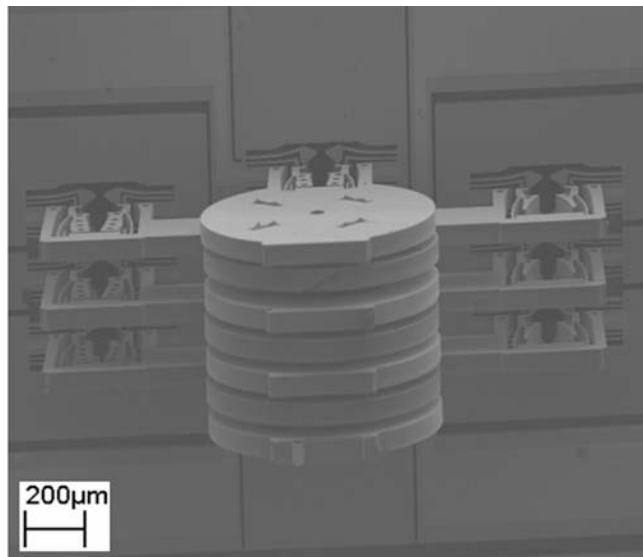


FIG. 22—*SEM image of the assembled Coaxial Ring Ion Trap (80x magnification); 500 μm i.d. ring electrodes, 75 μm i.d. endcap electrodes.*

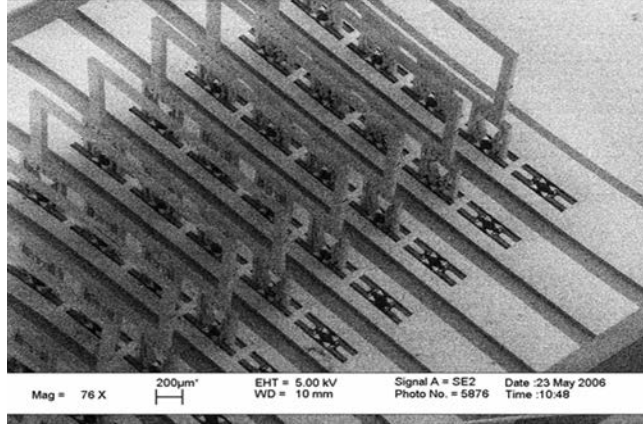


FIG. 23—SEM image of the Reflectron Optics; rectangular elements are 1.0 mm high, 2.0 mm long, 0.05 mm thick with 0.5 mm spacing.

The reflectron optic consisted of a series of fifteen optical elements. Each element was rectangular with a 1000 μm height and 2000 μm length. The elements were 50 μm thick and spaced at 500 μm . The individual reflectron lenses were resistively coupled to produce a voltage gradient from 100 to 500 V. Two orthonormal lenses were placed in front of the reflectron element with small bias differences to adjust the entrance angle of the ion beam. Ions were once again formed by an EI source and pulse-extracted into the reflectron optics. A channeltron detector was placed 5° off axis to collect the ion signal.

The final ion optic to discuss is an assembled MEMS Einzel lens. Einzel lenses consisted of three lens elements, with the first and third at the same potential, and the second with tunability. The Einzel lens was utilized to point focus a diffuse ion beam, typically to increase the ion current for analysis and detection. Our lenses were once again released from a 50 μm device layer. The elements had a 1000 μm o.d., a 250 μm i.d., and they were spaced 250 μm apart. The ion beam was created with a 70 eV EI source, and could produce an ion beam with 50-500 eV of translational energy. Lens 1 and 3 were electrically connected and set to ground, while lens 2 could range from

0-600 V. The ion beam was then focused into a 75 μm i.d. aperture placed before an electron multiplier detector. Data for both an approximate 100 eV and 500 eV ion beam were collected by monitoring the ion current through the final orifice by adjusting a second focusing electrode.

4.3 Results and Discussion

Initial characterization of the electrical performance of the assembled devices was performed, and the breakdown voltage exceeds 750 V. Though the trenches between connection pads are the closest electrode-electrode features and V_b should well exceed the 750 V at vacuums greater than 1×10^{-5} torr, the breakdown is believed to occur through the backside handle wafer via the buried oxide layer. Small defects have been observed in the backside etch, creating features that shorten the electrode gaps. With our current devices, 750 V is an adequate breakdown voltage for these ion optics.

The Bradbury-Nielsen gate was tested in the presence of a 70 eV electron beam. The open position applied a 60 V potential to both poles of the gate, creating a field-free region between alternating wires, and allowing the electron beam to pass through with a 20% physical attenuation. The gate was closed by changing one of the poles to a 30 V potential, creating a field capable of diverting the electron beam. Fig 24 shows five cycles of the gate operation. The rise time of the gate coincides to the rise time of the switching electronics. Rise time limited by the gate was not determined.

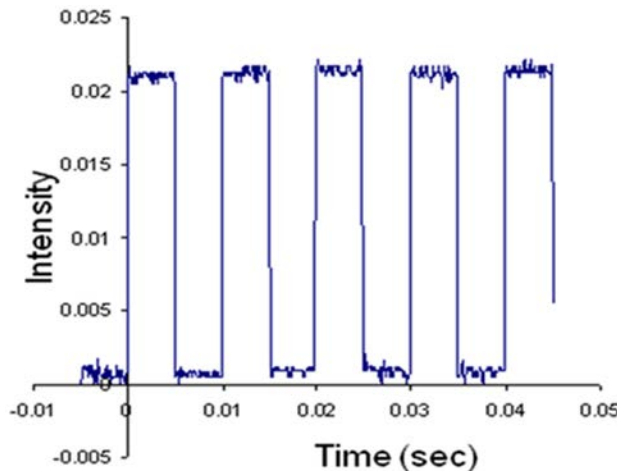


FIG. 24—*Data from the Bradbury-Nelson Gate alternating between 60V-60V and 60V-30V positions.*

The Einzel lens was characterized with a 100 eV and 500 eV ion beam of SF₆. Variation of the center electrode was 0-750 V. The resulting ion current is shown in Fig 25. Because the beam was produced by forming the ions in a 100 and 500 V potential difference grid region, a distribution of ion kinetic energy is expected. This accounts for the residual ion signal at the same lens potential greater than the ions' average kinetic energy. Utilizing this lens, a more accurate picture of the beams energy distribution can be determined. A working Einzel lens is a necessary component in miniaturization of mass analysis devices. Because small ion optical devices contain a lower ion presence due to space-charge and surface-charge effects, MEMS lenses can increase ion fluence into mass analyzers and detectors.

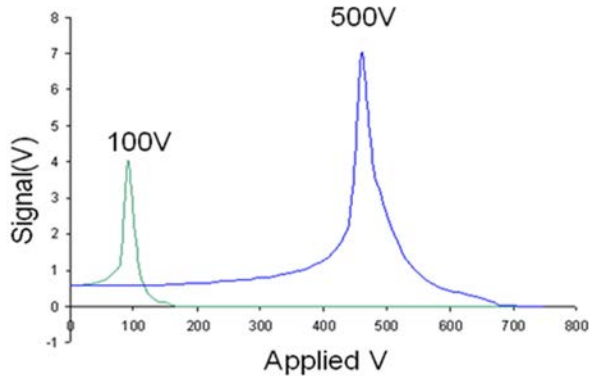


FIG. 25—*The signal distribution from the Einzel lens with both a 100 V and a 500 V ion beam.*

The coaxial ring ion trap was tested at 1×10^{-4} He with 1% toluene. The spectrum was collected by trapping at 8 MHz with a peak-to-peak voltage of 120 V, then ramping the V_{p-p} to scan out the trapped ions, and was collected for one minute (approximately 600 scans). Fig 26 shows the resulting spectrum. The coaxial-ring ion trap attained a peak width of 1.5 amu. The difficulty in increasing the resolution may come from concentric and perpendicular alignment errors, producing small aberrations in the trapping field. As the RF traps get smaller, contributions from small aberrations become more impactful in ion trap performance.

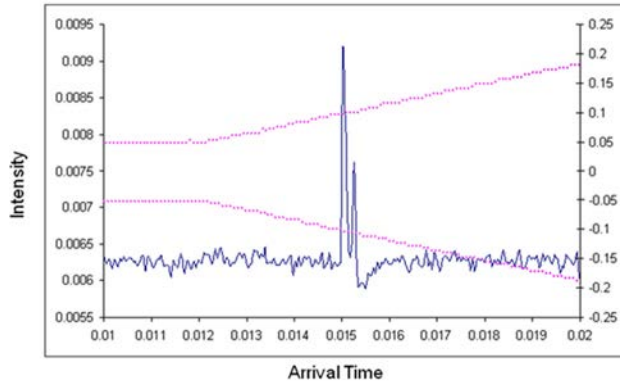


FIG. 26—*Spectrum obtained from a mixture of 10^{-4} torr He with 1% toluene on the coaxial ring ion trap (dotted line indicate V_{p-p}).*

The reflectron optics were also run with toluene at 1×10^{-7} torr. Signal was detected from the reflected optics, though no mass resolution was observed. Equation 3 in Chapter 1 best illustrates the difficulty of miniaturizing the TOF. Even with the reflectron optics, we expect no resolved peaks. The pulse extraction would have to be shorter with high attenuation values to start obtaining a resolved spectrum. We also propose increasing the path length by placing multiple reflectron optics, staggered to zig-zag the ion beam towards the detector (42). This could be accomplished on a small footprint device.

4.5 References

1. Kornienko O, Reilly PTA, Whitten WB, Ramsey JM. Electron impact ionization in a microion trap mass spectrometer. *Rev Sci Instrum.* 1999 Oct;70(10):3907-9.
2. Whitten WB, Reilly PTA, Ramsey JM. High-pressure ion trap mass spectrometry. *Rapid Commun Mass Sp.* 2004;18(15):1749-52.
3. Austin DE, Peng Y, Hansen BJ, Miller IW, Rockwood AL, Hawkins AR, et al. Novel Ion Traps Using Planar Resistive Electrodes: Implications for Miniaturized Mass Analyzers. *J Am Soc Mass Spectr.* 2008 Oct;19(10):1435-41.
4. Contreras JA, Murray JA, Tolley SE, Oliphant JL, Tolley HD, Lammert SA, et al. Hand-Portable Gas Chromatograph-Toroidal Ion Trap Mass Spectrometer (GC-TMS) for Detection of Hazardous Compounds. *J Am Soc Mass Spectr.* 2008 Oct;19(10):1425-34.
5. Brinckerhoff WB. Pulsed laser ablation TOF-MS analysis of planets and small bodies. *Appl Phys a-Mater.* 2004 Sep;79(4-6):953-6.
6. Hagan NA, Cornish TJ, Pilato RS, Van Houten KA, Antoine MD, Lippa TP, et al. Detection and identification of immobilized low-volatility organophosphates by desorption ionization mass spectrometry. *Int J Mass Spectrom.* 2008 Dec 1;278(2-3):158-65.
7. Gao L, Sugiarto A, Harper JD, Cooks RG, Ouyang Z. Design and Characterization of a Multisource Hand-Held Tandem Mass Spectrometer. *Analytical Chemistry.* [doi: 10.1021/ac801275x]. 2008 2008/10/01;80(19):7198-205.

8. Keil A, Talaty N, Janfelt C, Noll RJ, Gao L, Ouyang Z, et al. Ambient mass spectrometry with a handheld mass spectrometer at high pressure. *Analytical Chemistry*. 2007 Oct 15;79(20):7734-9.
9. Makas AL, Troshkov ML, Kudryavtsev AS, Lunin V. Miniaturized mass-selective detector with atmospheric pressure chemical ionization. *J Chromatogr B*. 2004 Feb 5;800(1-2):63-7.
10. Tanaka YT, Yoshikawa I, Yoshioka K, Terasawa T, Saito Y, Mukai T. Gamma-ray detection efficiency of the microchannel plate installed as an ion detector in the low energy particle instrument onboard the GEOTAIL satellite. *Rev Sci Instrum*. 2007 Mar;78(3).
11. Jee SE, Lee PS, Yoon BJ, Jeong SH, Lee KH. Fabrication of microstructures by wet etching of anodic aluminum oxide substrates. *Chem Mater*. 2005 Aug 9;17(16):4049-52.
12. Kuo DS, Chang SJ, Ko TK, Shen CF, Hon SJ, Hung SC. Nitride-Based LEDs With Phosphoric Acid Etched Undercut Sidewalls. *Ieee Photonic Tech L*. 2009 Apr 15;21(8):510-2.
13. Jiang YR, Liu GZ, Zhou J. A novel process for circle-like 3D microstructures by two-step wet etching. *Journal of Micromechanics and Microengineering*. 2009 Jan;19(1).
14. Ehrfeld W, Schmidt A, editors. *Recent developments in deep x-ray lithography*; 1998; Chicago, Illinois (USA). AVS.
15. Kupka R, Bouamrane F, Megert S. Microfabrication of massive parallel micromirror-lenses by X-ray LIGA technique: recent advances and prospects. *Microsyst Technol*. 2003 Dec;10(1):22-8.
16. Park DSW, Kim K, Pillans B, Lee JB. Polydimethylsiloxane-based pattern transfer process for the post-IC integration of MEMS onto CMOS chips. *Journal of Micromechanics and Microengineering*. 2004 Mar;14(3):335-40.
17. Goettl J, Datta P, Desta Y, Jin Y, Ling Z-g, Singh V, editors. *LIGA research and service at CAMD*. *Journal of Physics: Conference Series*; 2006. IOP Publishing.
18. Meyer P, Schulz J, Hahn L, Saile V. Why you will use the deep X-ray LIG(A) technology to produce MEMS? *Microsyst Technol*. 2008 Oct;14(9-11):1491-7.
19. Saini R, Jandric Z, Gammell J, Mentink SAM, Tuggle D. Manufacturable MEMS miniSEMs. *Microelectron Eng*. 2006 Apr-Sep;83(4-9):1376-81.

20. Saini R, Jandric Z, Tsui K, Udeshi T, Tuggle D. Assembled micro-electromechanical-systems microcolumn from a single layer silicon process. *J Vac Sci Technol B*. 2004 Nov-Dec;22(6):3168-73.
21. Isakovic AF, Stein A, Warren JB, Narayanan S, Sprung M, Sandy AR, et al. Diamond kinoform hard X-ray refractive lenses: design, nanofabrication and testing. *J Synchrotron Radiat*. 2009 Jan;16:8-13.
22. Abdolvand R, Ayazi F. An advanced reactive ion etching process for very high aspect-ratio sub-micron wide trenches in silicon. *Sensor Actuat a-Phys*. 2008 May 28;144(1):109-16.
23. Yun SS, Jeong DH, Wang SM, Je CH, Lee ML, Hwang G, et al. Fabrication of morphological defect-free vertical electrodes using a (110) silicon-on-patterned-insulator process for micromachined capacitive inclinometers. *Journal of Micromechanics and Microengineering*. 2009 Mar;19(3):-.
24. Moxom J, Reilly PTA, Whitten WB, Ramsey JM. Double resonance ejection in a micro ion trap mass spectrometer. *Rapid Commun Mass Sp*. 2002;16(8):755-60.
25. Moxom J, Reilly PTA, Whitten WB, Ramsey M. Analysis of volatile organic compounds in air with a micro ion trap mass analyzer. *Analytical Chemistry*. 2003 Aug 1;75(15):3739-43.
26. Gao L, Song QY, Patterson GE, Cooks RG, Ouyang Z. Handheld rectilinear ion trap mass spectrometer. *Analytical Chemistry*. 2006 Sep 1;78(17):5994-6002.
27. Sokol E, Edwards KE, Qian K, Cooks RG. Rapid hydrocarbon analysis using a miniature rectilinear ion trap mass spectrometer. *Analyst*. 2008;133(8):1064-71.
28. Lammert SA, Rockwood AA, Wang M, Lee ML, Lee ED, Tolley SE, et al. Miniature toroidal radio frequency ion trap mass analyzer. *J Am Soc Mass Spectr*. 2006 Jul;17(7):916-22.
29. Brinckerhoff WB, Cornish TJ, McEntire RW, Cheng AF, Benson RC. Miniature time-of-flight mass spectrometers for in situ composition studies. *Acta Astronaut*. 2003 Jan-Mar;52(2-6):397-404.
30. Diaz JA, Giese CF, Gentry WR. Sub-miniature ExB sector-field mass spectrometer. *J Am Soc Mass Spectr*. 2001 Jun;12(6):619-32.
31. Dawson PH. Quadrupole Mass Spectrometry and Its Applications. 2nd ed. New York: American Institute of Physics, 1995.
32. Gohl W, Kutscher R, Laue HJ, Wollnik H. International Journal of Mass Spectrometry and Ion Physics. 1983;14:411.

33. Mamyrin BA, Karatev VI, Shmikk DV, Zagulin VA. Soviet Physics JETP. 1973;37:45.
34. Geear M, Syms RRA, Wright S, Holmes AS. Monolithic MEMS quadrupole mass spectrometers by deep silicon etching. *J Microelectromech S*. 2005 Oct;14(5):1156-66.
35. Sillon N, Baptist R. Micromachined mass spectrometer. *Sensor Actuat B-Chem*. 2002 Mar 15;83(1-3):129-37.
36. Wapelhorst E, Hauschild JP, Muller J. Complex MEMS: a fully integrated TOF micro mass spectrometer. *Sensor Actuat a-Phys*. 2007 Jul 20;138(1):22-7.
37. Hauschild JP, Wapelhorst E, Muller J. Mass spectra measured by a fully integrated MEMS mass spectrometer. *Int J Mass Spectrom*. 2007 Jun 15;264(1):53-60.
38. Debatin M, Kroner M, Mikosch J, Trippel S, Morrison N, Reetz-Lamour M, et al. Planar multipole ion trap. *Phys Rev A*. 2008 Mar;77(3).
39. Blain MG, Riter LS, Cruz D, Austin DE, Wu GX, Plass WR, et al. Towards the hand-held mass spectrometer: design considerations, simulation, and fabrication of micrometer-scaled cylindrical ion traps. *Int J Mass Spectrom*. 2004 Aug;236(1-3):91-104.
40. Van Amerom FH, Chaudhary A, Cardenas M, Bumgarner J, Short RT. Microfabrication of cylindrical ion trap mass spectrometer arrays for handheld chemical analyzers. *Chemical Engineering Communications*. 2007;195(2):98-114.
41. Taylor S, Tindall RF, Syms RRA. Silicon based quadrupole mass spectrometry using microelectromechanical systems. *J Vac Sci Technol B*. 2001 Mar-Apr;19(2):557-62.
42. Wollnik H, Przewloka M. Time-of-flight mass spectrometers with multiply reflected ion trajectories. *International Journal of Mass Spectrometry and Ion Processes*. 1990;96(3):267-74.

CHAPTER 5

SOFT LANDING-ION MOBILITY AND MONITORING PLASMA DEPOSITION IN SITU VIA MINIATURE MASS SPECTROMETRY

5.1 Introduction

Over the past decade, the amount of time and effort focused on materials research has increased at an exponential rate, and the impetus for this research lies mainly in the perpetually growing demand for consumer and industrial technology (1, 2). Many metal compounds of the general structure M_xR_y (where R is a main group element) have been shown to have many useful catalytic (3, 4), tribological (5) or electronic properties (6, 7) which could be utilized in current and future technology. However, the number of possible metal/main group combinations and stoichiometries make the process of combing through the possible compounds a daunting task. This is compounded by the possibility of alteration of the deposited materials by high-pressure environments (8-10) or the need for post-synthesis modification (7, 11, 12). It is with that in mind that this multi-analysis platform was developed, providing the opportunity to synthesize, modify and analyze such compounds rapidly in situ. Soft landing-ion mobility (SLIM) has been shown to be a simple and robust method for isolating and collecting a number of such compounds (13, 14). Because of the potential for the collisional activation of rearrangements in the generated ions, it is necessary for the ion to be moved through the ion mobility cell in low-field conditions where the energy of the ion gained by collisions is less than the thermal energy of the buffer gas (15-18). It is with this in mind that a platform to perform this task has been proposed and development of said platform undertaken.

Utilizing laser ablation, gas-phase metal clusters can be generated in low vacuum, and metal/main group compounds can be synthesized by performing the same ablation in a vacuum chamber back-filled with an appropriate buffer gas. Soft landing-ion mobility is utilized to deposit selected clusters on a substrate of our choosing while also providing structural information on the selected compound. After deposition, Raman microscopy and multiple internal reflection infrared spectroscopy can be employed on the sample *in situ* for spectroscopic analyses. Additionally, plasma modification and mass spectrometry can also be utilized to further characterize the deposited material.

This chapter will discuss the conception of the platform and the initial work performed to bring it into operation.

5.2 Platform Design

The centerpiece of the analysis platform was a custom-made, stainless steel, cubic vacuum chamber equipped with five 2.75" CF flanges around the sides and three on the top. Also included was a recessed quartz window to allow for Raman microscopy to be performed *in situ*. The intended final configuration can be seen in Fig 27. Specific details on instrumental operation will be discussed in their respective section.

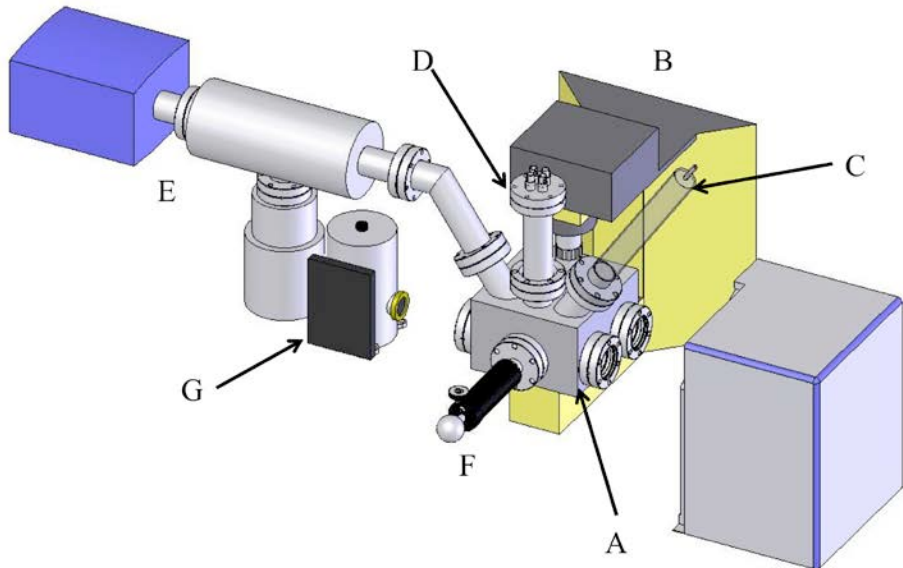


FIG. 27—Model depicting the multi-analysis platform consisting of the vacuum chamber (A), Raman microscope (B), quartz plasma tube (C), SLIM instrument (D), mass spectrometer (E), linear sample actuator (F) and MCT/A IR detector (G).

For sample generation, a SLIM cell was designed and assembled in-house (Fig 28). The instrument consisted of fifteen resistively-coupled stainless steel rings with an outer diameter of 0.95”, an inner diameter of 0.50” and a thickness of 0.24”. The final ring in the cell was a split-ring optic whose voltages could be controlled independently to steer ions before leaving the cell. The rings were spaced 0.08” apart using ruby beads (Alfa Aesar, Ward Hill, MA) and were held between two compression plates, mounted on 0.080” all-thread rails housed in ceramic sleeves (Omega Engineering, Stamford, CT). In a later iteration, a stainless steel repeller plate was incorporated into the instrument to propel ions into the ion mobility field. The entire instrument was mounted on a 2.75” CF flange with four electrical feed-throughs.

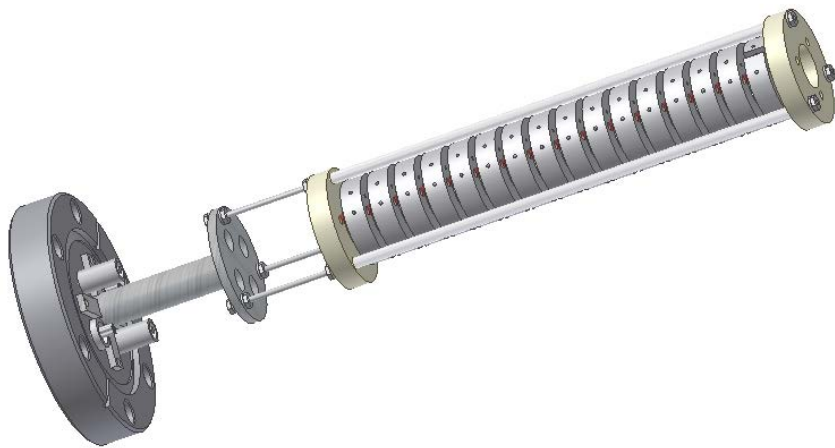


FIG. 28—*The soft landing-ion mobility cell.*

Ion clusters were generated via laser ablation. To accomplish this, the mobility was housed in a four-way cross containing 2.75" CF flanges for the SLIM cell and vacuum chamber, and 1.33" CF flanges for the sample holder and quartz window. Ion detection was accomplished by a Faraday plate situated on the linear sample actuator.

The vacuum chamber was situated on a laser platform constructed to offer lateral and altitudinal motion (longitudinal motion was provided by the linear sample actuator). This platform was constructed underneath a Raman microscope (Olympus, Center Valley, PA) equipped with a 2.05 cm-working distance microscope objective (Mitutoyo, Aurora, IL) in order to act as a heavy-load microscope stage. Raman analysis was accomplished with a T64000, triple grating spectrometer (Horiba, Edison, NJ).

Plasma modification and deposition was accomplished via a capacitatively-coupled plasma housed in a custom-made quartz tube, mounted on a CF flange, and linear quadrupole mass analyzer equipped with a low vacuum (100 mtorr) conductance limit (Inficon, Syracuse, NY) was utilized for mass spectral analysis during plasma deposition and modification. To

protect the mass spec during these experiments, it was connected orthogonally with respect to the plasma tube via 2.75" CF flange.

5.3 Substrate Preparation

Silicon wafers with 100 orientation (WaferNet, Inc. San Jose, California) were utilized as substrates for all deposition experiments. The wafers were cleaved to the desired dimensions using a glass cutter, and subsequently cleaned using the RCA-1 method (19) and etched. Briefly, the cleaved wafers were placed into a solution containing 3.9% ammonium hydroxide and 4.3% hydrogen peroxide. The solution was then heated to 70° C and stirred occasionally for 15 min. Afterwards, the wafers were collected, rinsed with DI water and then placed into a room temperature solution of 1.0% hydrofluoric acid to remove the oxide layer left by the RCA clean.

5.4 Soft Landing-Ion Mobility and Raman Spectroscopy

For the SLIM experiments, a hafnium rod (ESPI Metals, Ashland, OR) was used to create ion clusters. One end of the rod was ground at a 45° angle to facilitate ion transport into the SLIM field during the ablation event. The other end was firmly seated in an aluminum sleeve used as a linear feed-through. The sleeve was placed into the vacuum chamber via a 0.25" Ultra-Torr fitting (Swagelok, Solon, OH) mounted to a 1.33" CF flange such that the hafnium rod rested between the repeller plate and first compression ring of the mobility cell. The sample stage (mounted on the linear feed-through) was oriented just beyond the exit of mobility cell. Both the detector and silicon were affixed to the stage. For time-dependent deposition experiments, a glass housing was constructed for the silicon wafer such that only portions of it could be exposed to the ion packet during a deposition experiment.

The vacuum chamber was evacuated to the base pressure of the rough pump used (roughly 20 mtorr), and then it was back-filled with a mixture of 5% O₂ in He to a pressure of

5.0 torr. The repeller plate was biased at 200 V and a 180 V bias was applied to the entrance ring of the mobility cell. The terminal ring of the cell was grounded, giving the cell a field of 14.4 V/cm.

Laser ablation was performed with an 1064 nm Nd:YAG laser (Continuum, Santa Clara, CA) operated at discharge voltage of 1.15 kV and a repetition rate of 2.0 Hz. The beam was point-focused and rastered on the hafnium rod using a convex lens housed in a mount with x and y motion. The resulting ion signal was collected with the Faraday plate, then amplified and viewed on a digital oscilloscope. The resulting ion mobility spectrum can be seen in Fig 29.

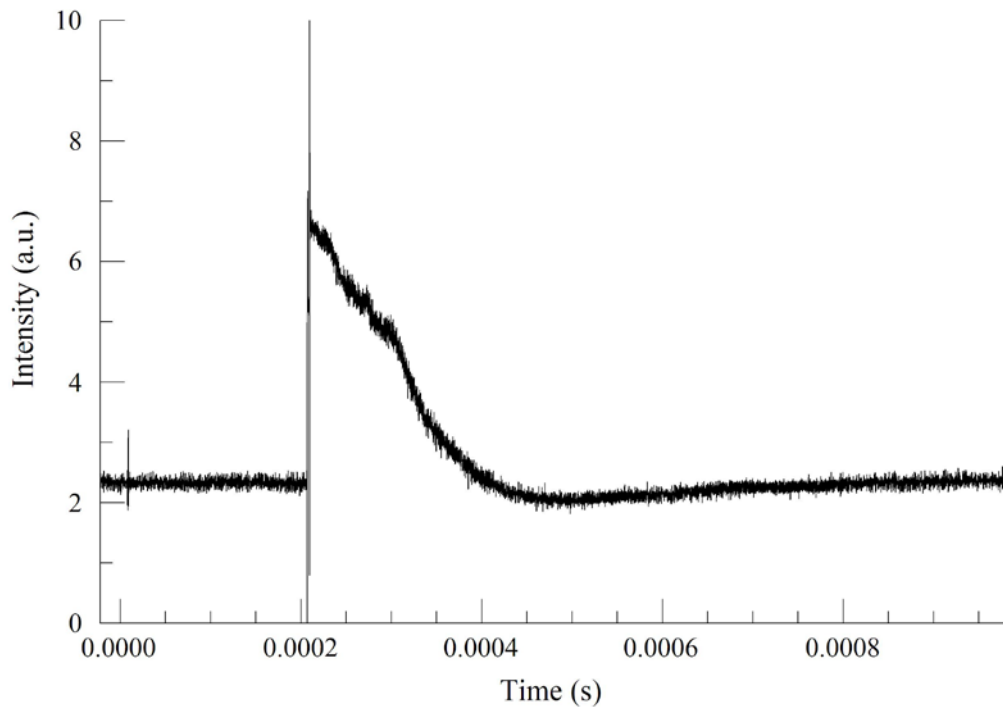


FIG. 29:—The ion mobility spectrum of hafnium ablated in 5% O₂ in He at 5.0 torr.

The small line at t=0 represents a small, instantaneous noise generated in the detector chain by sudden and intense electromagnetic field of the ablation even event. The ions arrive at the detector just shortly after the 2.0 ms mark. The broad and unresolved peak distribution represents Hf_n⁺ clusters and HfO₂⁺.

Once the ion signal was observed, the sample feed-through was moved to place a silicon substrate in line with the exit of the mobility cell. Soft landing deposition was performed on the wafer in three discreet segments with deposition times of 4, 8 and 12 h.

After the deposition, to test the viability of *in situ* Raman sampling, the sample stage was moved underneath the quartz window of the microscope and a suitable particle was found for Raman analysis on the 12-hour deposition partition. The Raman spectrum was collected from 174 to 1200 cm⁻¹ using a 532 nm diode laser for excitation and 10 s exposures. A micrograph and resulting spectrum can be seen in Fig 30. The most prominent peak in the Raman spectrum is the silicon phonon peak at 521 cm⁻¹. The most intense hafnia peak is the oxygen-dominated vibration seen at 489 cm⁻¹, and while the remaining non-silicon peaks are indicative of hafnia, their assignment is still the subject of study (20). The low-intensity peaks in the lower wave number region lack enough resolution for identification and this was an issue that persisted throughout the *in situ* measurements. There were two suspected causes.

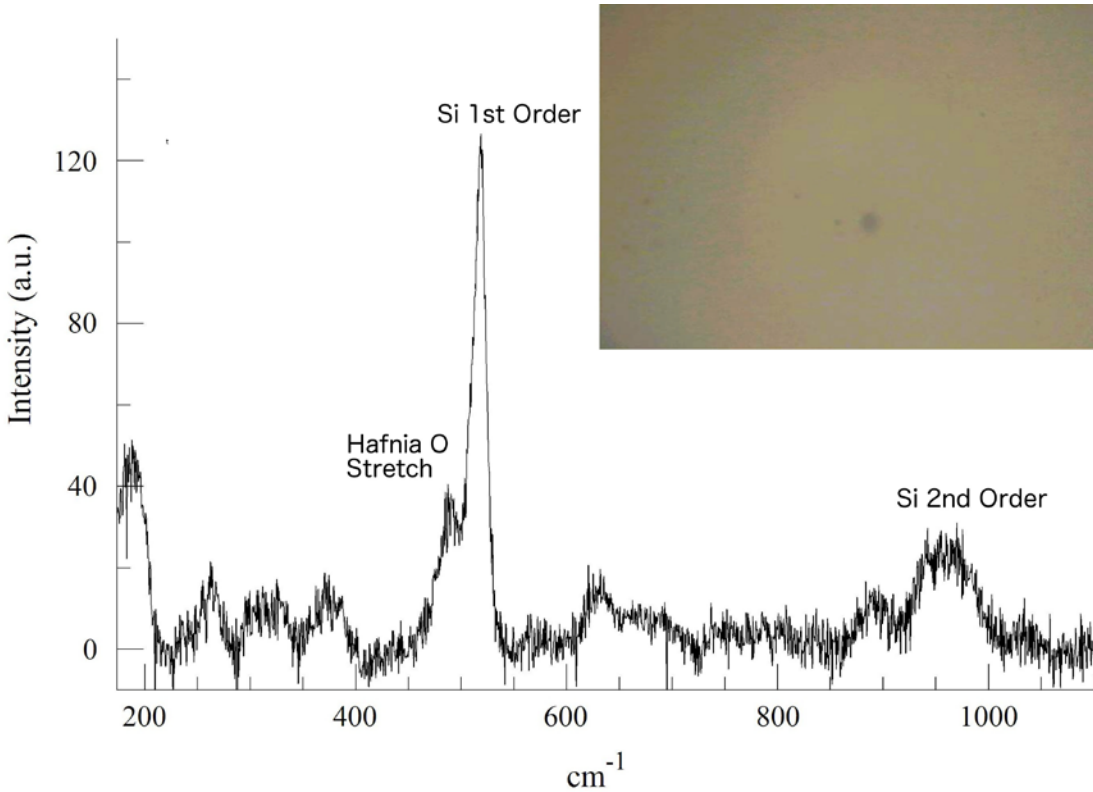


FIG. 30—*In situ* Raman spectrum of HfO_2 and 50x micrograph of the particle analyzed.

First, and most likely, there were significant losses to laser energy at the sample due to the reflective scattering of the quartz window in the vacuum chamber. Given that window rests roughly in the center of the 2.05 cm working distance of the microscope, these losses may occur to a significant degree on both the outgoing and incoming pass of the laser line. Secondly, vibrations from the rough pump propagate through the vacuum line to the chamber and, finally, are magnified by the arm of the sample stage feed-through. These issues were also evident in the micrograph, as an in-focus image was difficult to obtain.

In order to assess the sample directly, Raman spectra were collected from the sample outside of the vacuum chamber, using the same objective and laser conditions. A representative spectrum and micrograph of the particles analyzed can be seen in Fig 31.

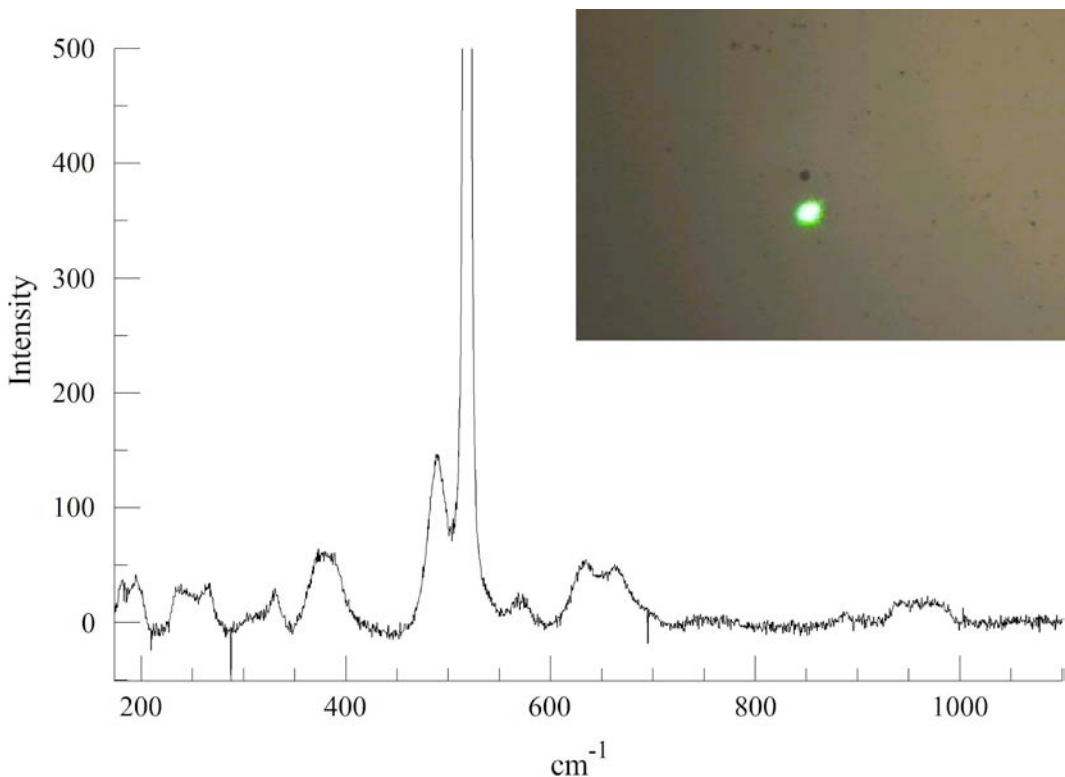


FIG. 31—*Ex situ Raman spectrum of HfO_2 and 50x micrograph of the particle analyzed.*

A rough assessment of particle size and coverage was performed at 10x magnification using the Raman microscope, and this was expanded upon using scanning electron microscopy to examine the different regions of the wafer (Fig 32).

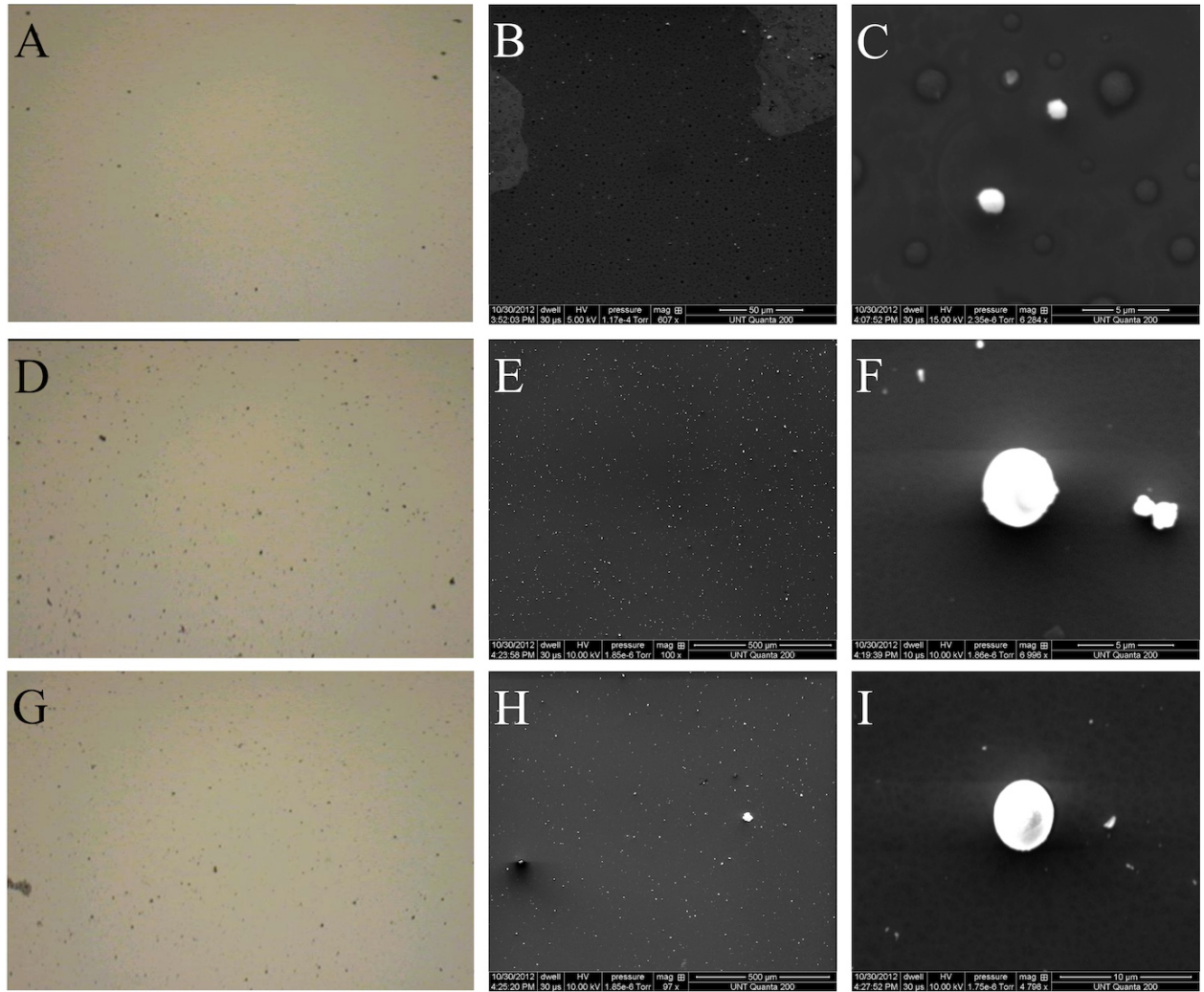


FIG. 32—*Micrograph of the silicon wafer. Panels A,D and G show 10x images of the 4,8 and 12 hour deposition surfaces respectively. Broad SEM images can be seen in B (4 hour, 607x), E (8 hour, 100x) and H (12 hour, 97x). Representative particles in the different section of the wafer can be seen in C (4 hour, 6284x), F (8 hour, 6996x) and I (12 hour, 4796x).*

It can be seen from the light micrographs in Fig 32 that between the 4- and 8-hour deposition times, particle coverage increased. Hafnia particles of 1 μm or less dominated the surface exposed to the mobility cell the least. At the 8-hour mark, the particles started to exhibit a broader size distribution, ranging from <1 to 2.5 μm . This trend continued at the 12-hour mark, yielding particles up to 5.0 μm in diameter.

5.5 Plasma Deposition and Mass Spectrometry

Both plasma experiments and mass spectrometry were tested independently of the ion mobility and Raman experiments. Due to its potential applicability of this system to surface science and semiconductor research, concerns were raised over the possible presence of residual pump oil in the vacuum chamber and its potential effects on future experiments. Before continuing to a complete assembly and use of the full multi-analysis platform, these concerns would need to be addressed.

To begin, the vacuum systems and all non-electronic components were disassembled and thoroughly cleaned with methanol and hexane (Sigma Aldrich, St. Louis, MO), and then baked at 100° C for one hour to remove any residual oil from the interior. The chamber was then reassembled to include the quartz plasma tube and mass spectrometer oriented orthogonal to one another. The sample stage was placed on the system such that the silicon wafer was normal to the flange of the plasma tube (Fig 33).

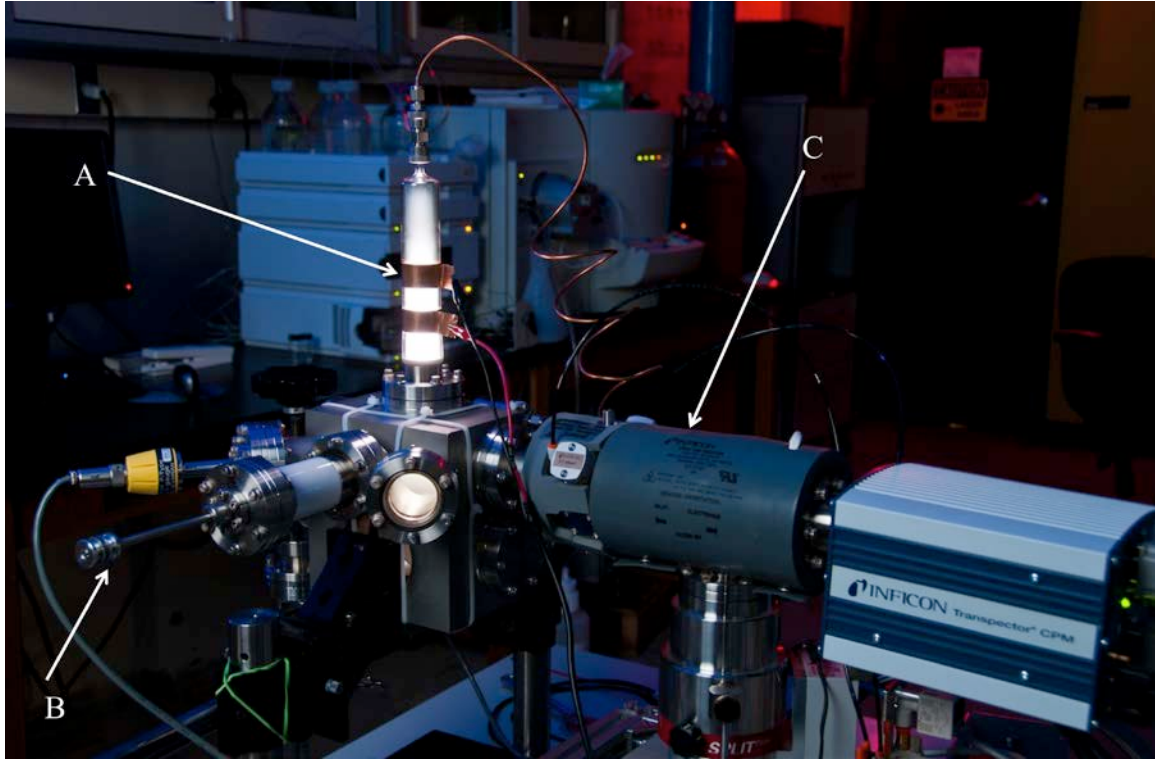


FIG. 33—The vacuum chamber equipped with the plasma tube (A), sample feed-through (B) and mass spectrometer (C).

The plasma was generated by evacuating the chamber to rough vacuum, back-filling with buffer gas to 50 mtorr (unless otherwise noted), and applying an amplified RF voltage to two copper sleeves (seen on the tube in Fig 33). For this research, an RF frequency of 19.3 MHz was chosen.

To begin the process of characterizing the plasma and mass spec functionality, the chamber was evacuated using an IDP-15 dry scroll pump (Agilent, Santa Clara, CA) and then filled to a pressure of 50 mtorr using a buffer gas containing 5% O₂ in He. An initial spectral scan from 1-50 m/z was collected for two minutes before the valve to the mass spectrometer was opened. After the scan, the valve was opened and another two-minute scan was collected. Finally, the plasma was ignited and a final two-minute scan was recorded. The results of these three scans can be seen in Fig 34.

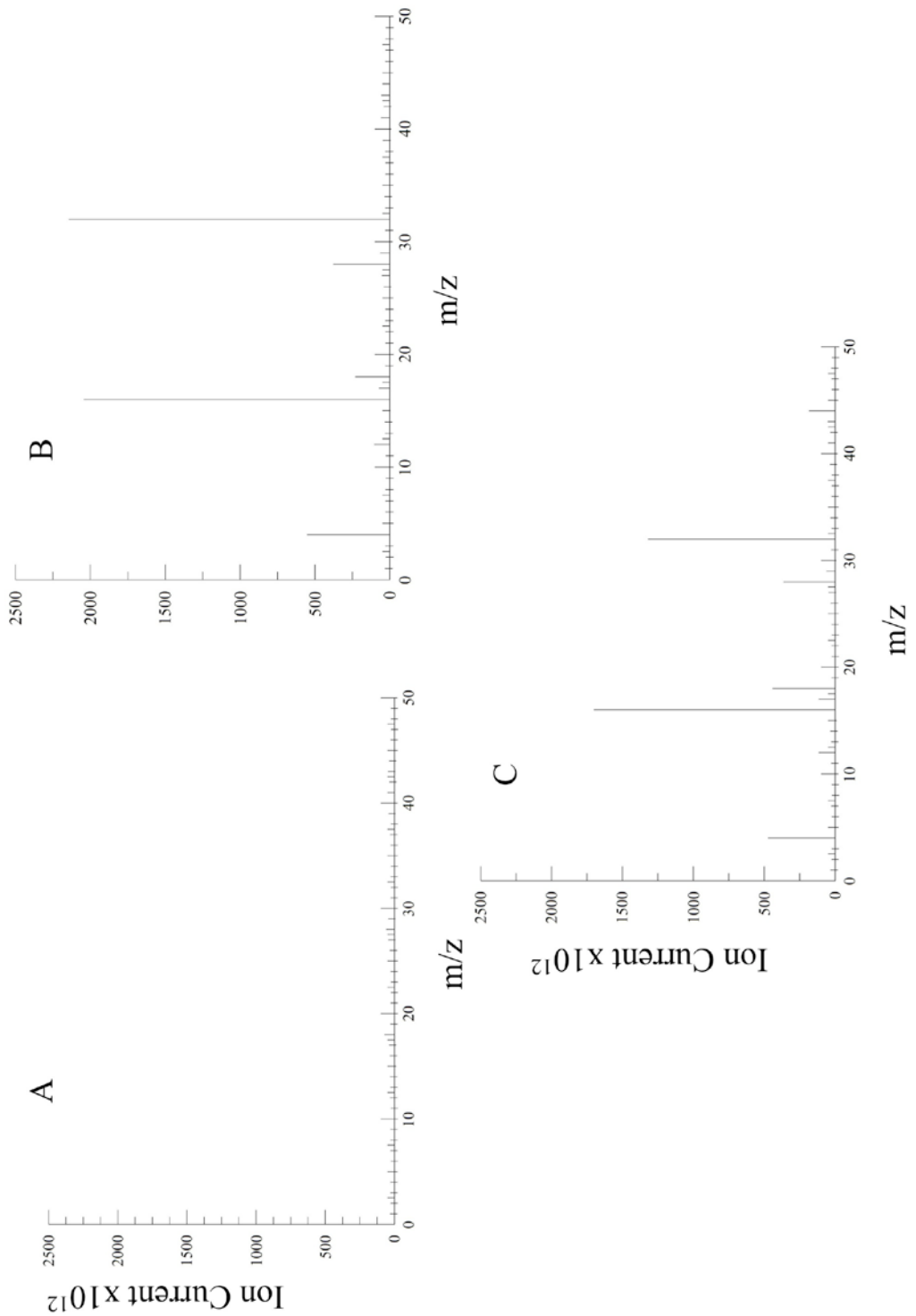


FIG. 34—Mass spectra for the vacuum chamber with the mass spec valve closed (A), the valve open (B) and the valve open with the plasma ignited (C).

As expected, the 100 mtorr conductance limit valve prevented any gas phase species from entering the mass spectrometer. When the valve was opened, He, O, O₂, H₂O and N₂ could be seen in the mass spectrum. Finally, when the plasma was ignited, a reduction of the oxygen species and a slight increase in the water signal was noted. The most notable feature in Fig 34 C is the peak at 44 m/z; the presence of carbon dioxide in the mass spectrum indicated that, while care had been taken to clean the components of the system, some carbon-containing species had been carried over. It is suspected that this arose from the chamber itself, as it was cleaned with soaked lint-free cloths and not submerged in a solvent bath.

The procedure for plasma ignition and mass spectral analysis mentioned above was carried out periodically over the course of 64 hours. The results can be seen in Fig 35.

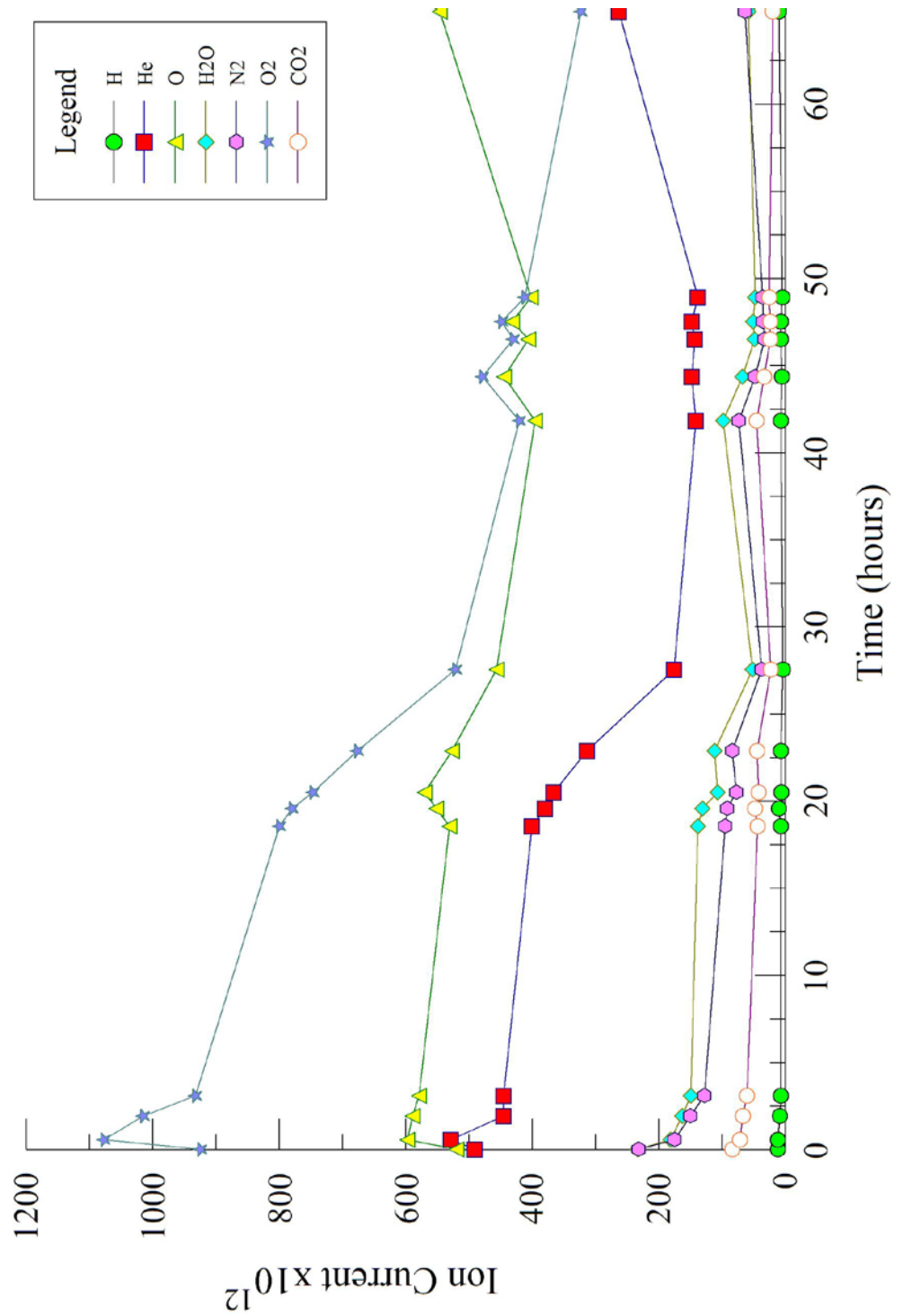


FIG. 35—Total ion counts for the mass spectra collected during the chamber's initial evacuation with the dry scroll pump

The relative total ion counts measured in the experiment track well with the He ion counts, indicating a relatively unchanging system aside from minor fluctuations in pressure altering the ion counts across the board with the exception of the three O data points near the twenty hour mark increasing where all others decreased. Noticing this trend, ion counts as a function of pressure and RF power (Fig 36) were examined. It should be noted that for the power-dependent data, no direct way of measuring V_{P-P} was available. Thus the RF power is referenced as the gain setting of the RF amplifier.

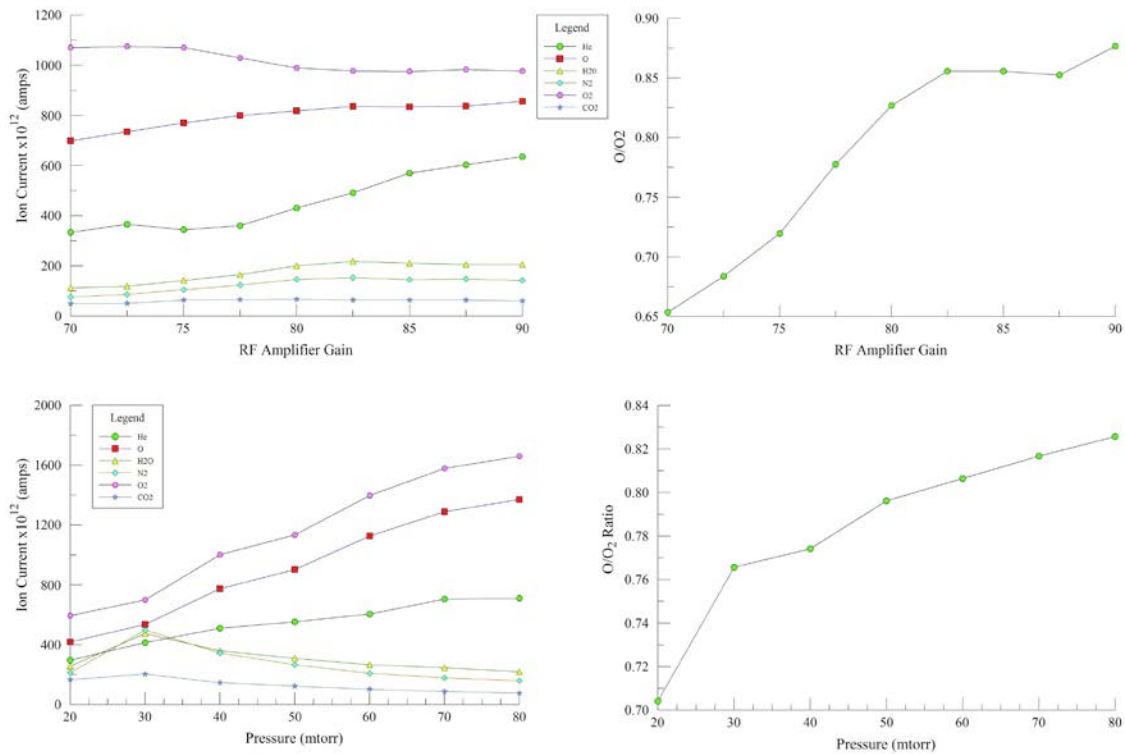


FIG. 36—Total ion counts (left) and O/O₂ ratios (right) for the plasma exhaust as a function of RF power (top) and chamber pressure (bottom).

The relationship between O/O₂ content and RF power may be inherently intuitive. As the RF power increases, more energy is imparted on the ionic species in the plasma, leading to higher energy collision and dissociation of polyatomic species, and thus, an increase in the O/O₂ ratio. Varying the pressure, however does not change the energy of the ionic species, but does

increase the rate of collisions, and thus, the probability for dissociation. Either of these factors could contribute to the variations in relative ion counts in Fig 35.

After the functionality of the plasma and mass spectrometer were assessed. The buffer gas was changed to 5% acetylene in He to perform carbon deposition on the silicon wafer. To accomplish this, a clean silicon wafer was placed on the sample stage and moved directly underneath the plasma tube. The chamber was back-filled to a pressure of 50 mtorr with the acetylene-containing buffer gas). Mass spectra were collected with the plasma off and ignited (Fig 37). Without the plasma, the mass spectrum of acetylene is clearly seen. After ignition, the acetylene signal at 26 m/z falls dramatically, and the remaining fragment peaks descend into the background noise. This is expected when considering the relative instability of the acetylene molecule and the energy of the plasma.

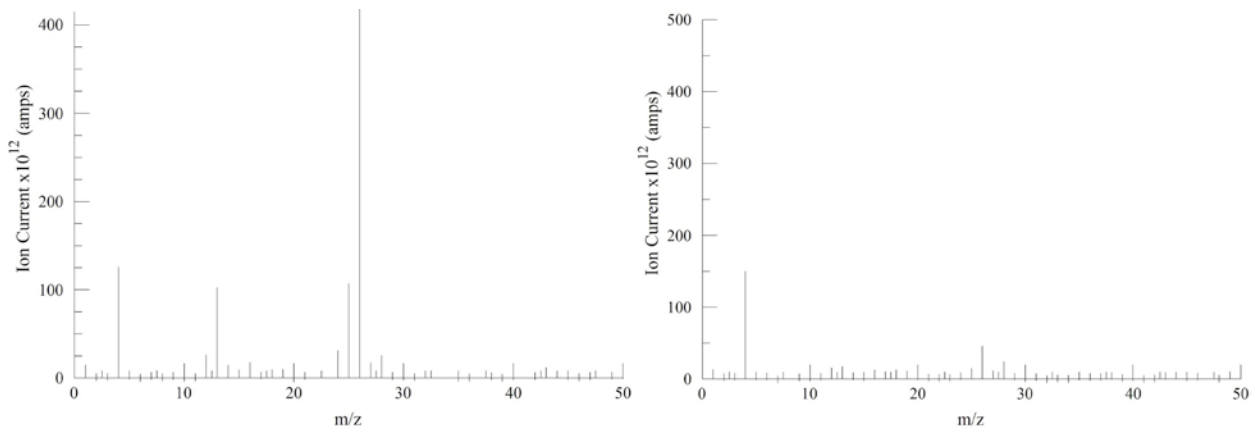


FIG. 37—Mass spectra of the acetylene buffer gas before plasma ignition (left) and after (right).

Acetylene deposition was performed for 30 minutes. The mass spectral trace of the process can be seen in Fig 38. After the plasma was shut off, a significant about of carbon buildup was noted on the interior of the plasma tube. The deposited material near the copper sleeves appeared to have some degree of crystal structure, so after the deposition, the plasma flange was removed and a small amount of the material was collected for Raman analysis

(Fig 39) which revealed a large presence of sp^2 hybridized carbon with little hydrogen content (21, 22). The silicon wafer was also removed from the chamber for Raman analysis (Fig 40). Results were similar to the spectrum of the material collected from the plasma tube.

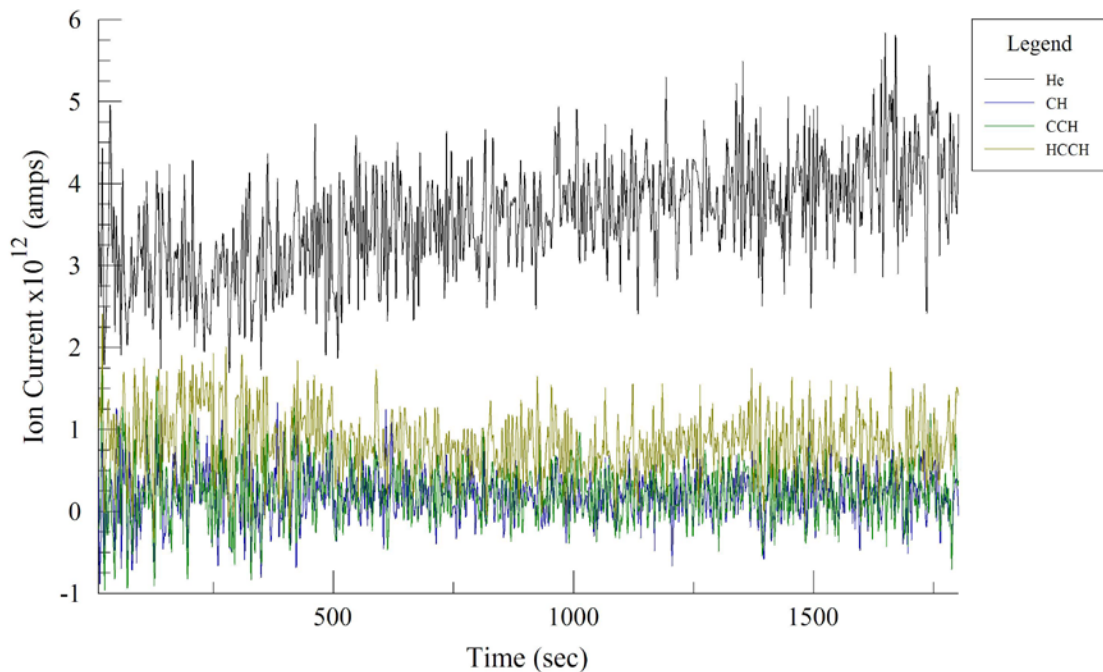


FIG. 38—*Ion traces of the species of interest during the carbon deposition.*

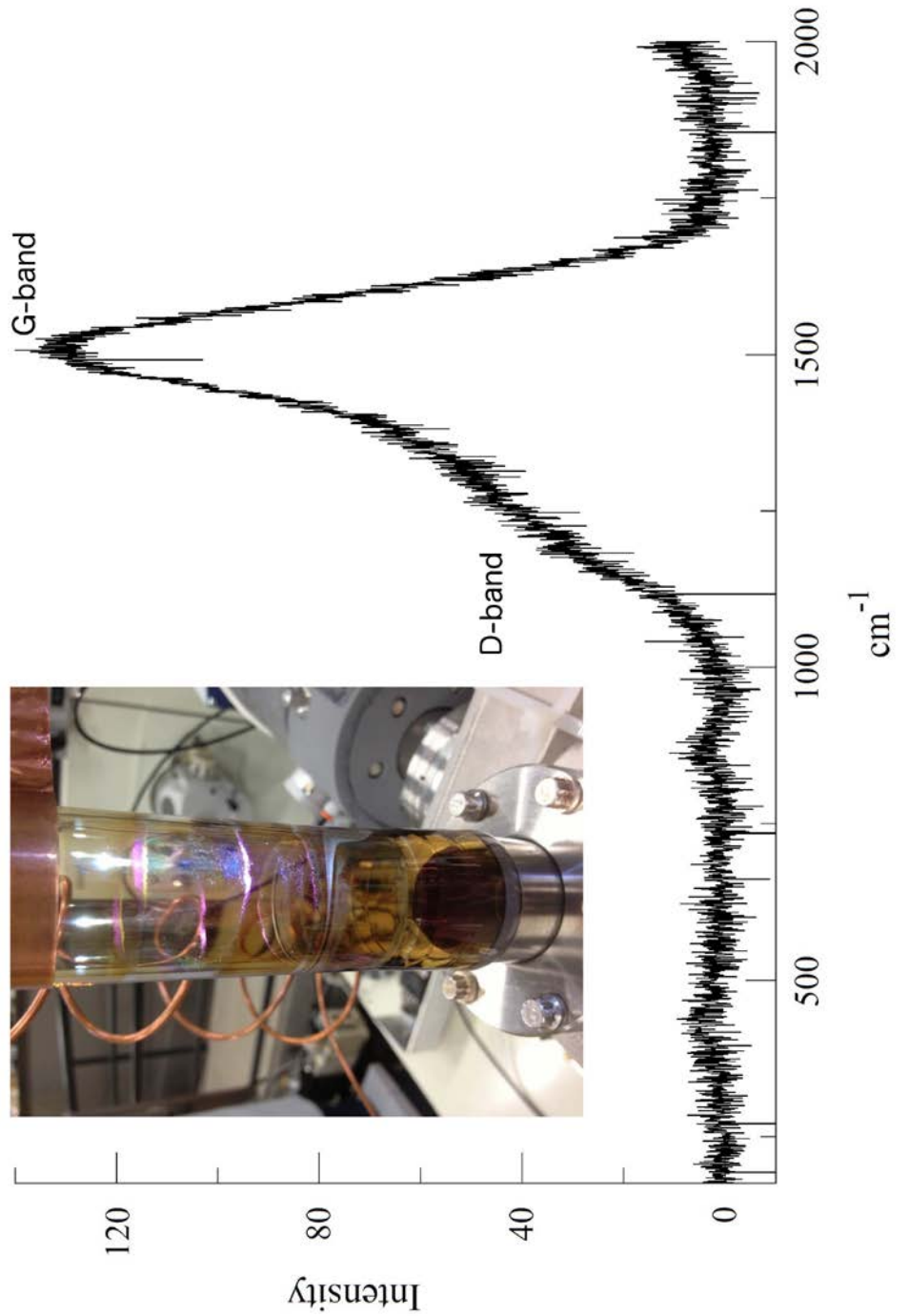


FIG. 39—Raman spectrum of the carbon deposits collected from the plasma tube with an image of the deposited material inlaid.

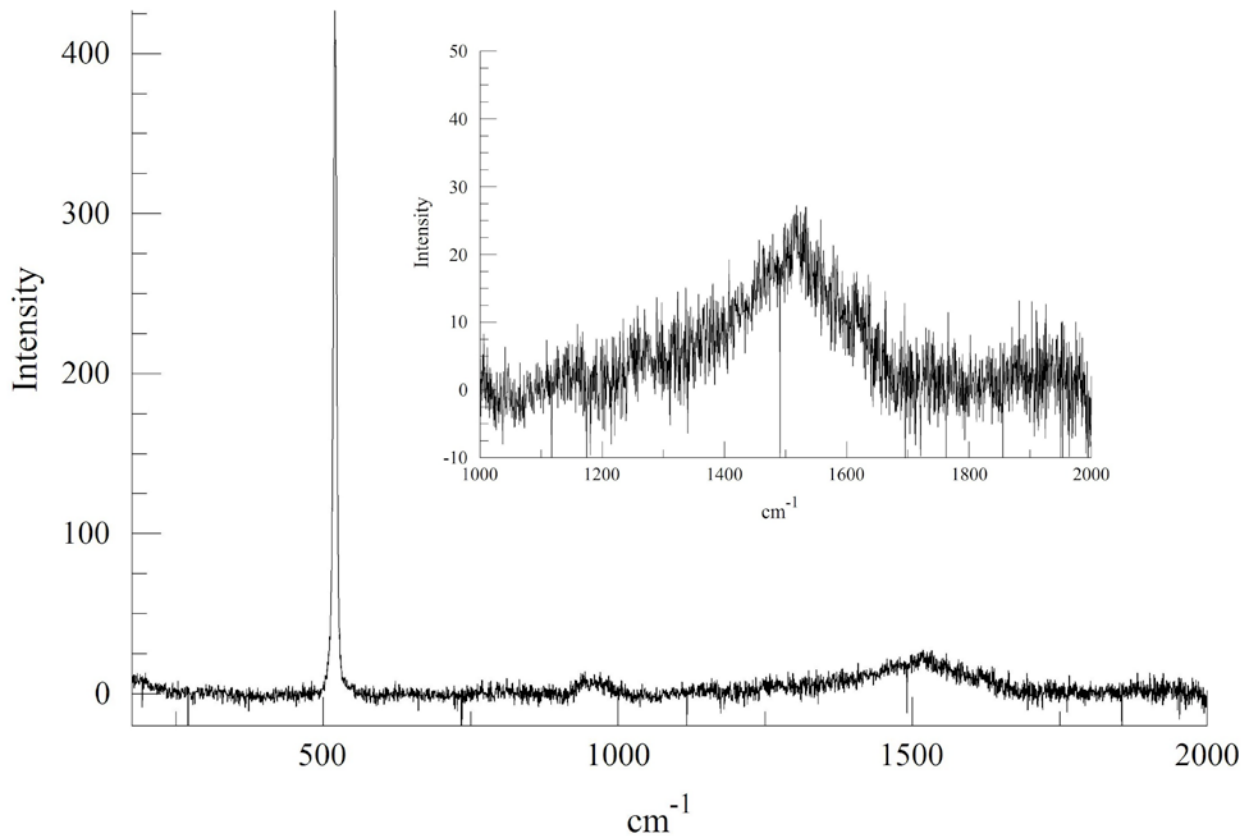


FIG. 40—*Raman spectrum of the carbon film deposited in the silicon wafer. A closer inspection of the 1500 cm^{-1} region is inlaid.*

Before resuming work with chamber, the plasma tube was soaked in a solution of 5% acetic acid for one hour, rinsed with DI water and then the remaining carbon residue was removed with a soft-bristled brush. The tube was then cleaned with methanol and hexane and baked before being placed back on the chamber. Before loading a new silicon wafer onto the sample stage, the gas was changed back to the helium/oxygen mixture used in the initial run and the plasma was ignited. This time, the plasma was used to clean and stray carbon from the remaining deposition. An ion trace of the cleaning process can be seen in Fig 41. The process was allowed to run until all of the ion counts returned to a nominal value (approximately 90 minutes). During that time, three distinct events appear to take place. First, water, nitrogen

and carbon dioxide concentrations increase in the plasma exhaust. It is likely that when the chamber was dismantled for sample collected, water and nitrogen adsorbed to the amorphous carbon left on the interior of the chamber. The next event occurs between 2000 and 3000 seconds, where the aforementioned species begin to decline in concentration as the O and O₂ signals begin to rise. During this time, most of the remaining carbon is removed from the chamber. Finally, at the 3500 s mark the values of the oxygen species resume their nominal values in relation to the He signal and the plasma cleaning is complete.

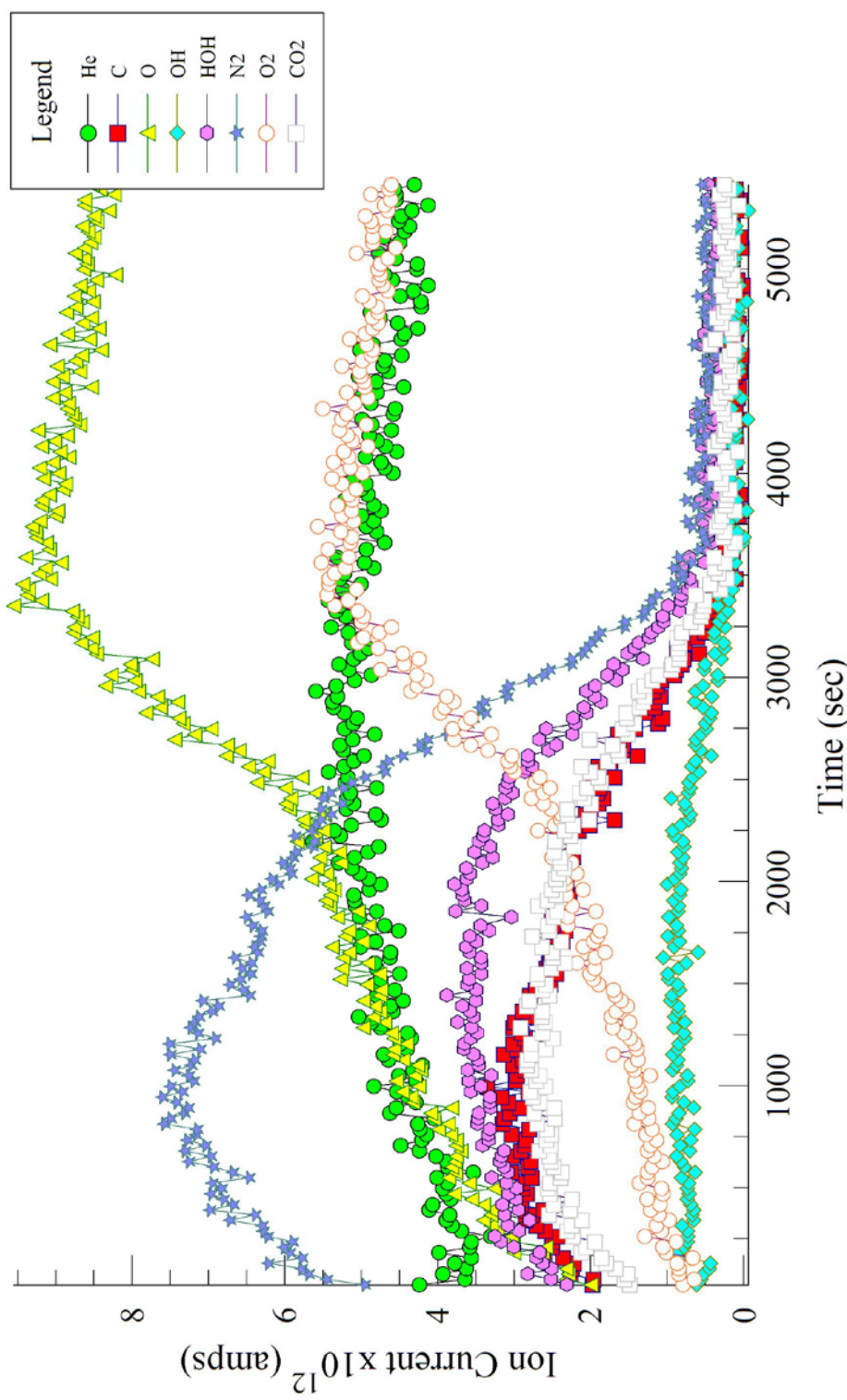


FIG. 41—Ion traces of the species of interest during oxygen plasma cleaning.

For the last phase of experimentation, the dry scroll pump was removed from the system and replaced with a rotary vane pump. Upon reaching the base pressure of the pump, the chamber was filled with the oxygen containing buffer gas to a pressure of 50 mtorr. Mass spectra were collected before and after plasma ignition. Then, the pump was allowed to run continuously for 72 hours (with a new silicon wafer on the sample stage). After that time, the acetylene deposition experiment was repeated. For comparative purposes, a summary of the ion counts in the mass spectra taken with the two pumps can be seen in Fig 42. It can be seen that the overall ion counts are lower for the rotary vane pump, with the exception of water and carbon containing species in the oil pump data after 72 hours, indicating a significant degree of contamination emanating from the pump itself.

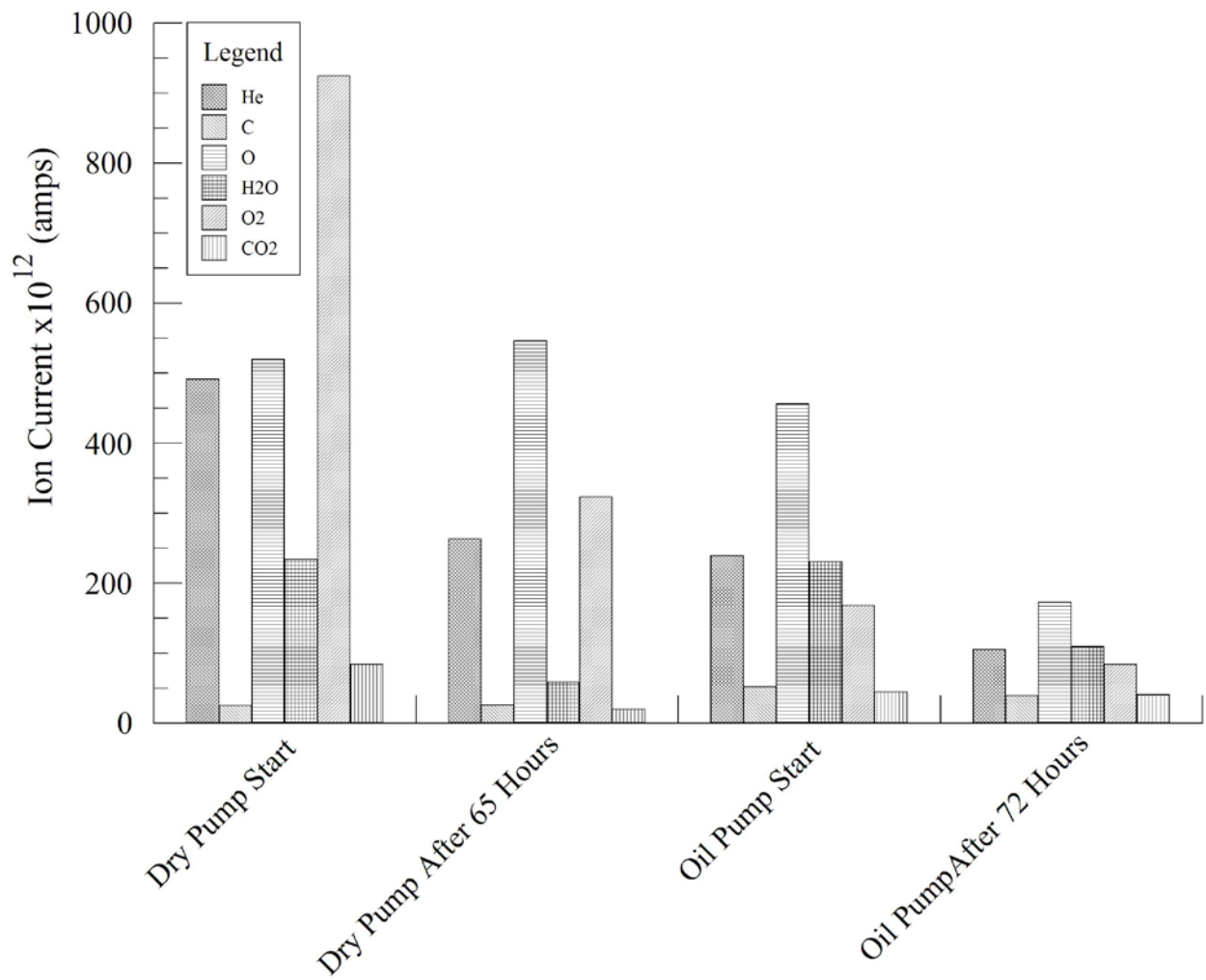


FIG. 42—Comparison of the ion counts at the beginning of each pump cycle and after an appreciable pumping time. The spectra were collected in the presence of the oxygen-containing plasma.

The silicon wafer with the deposited carbon was removed from the chamber for Raman analysis. The results can be seen in Fig 43. The results are far more dramatic than those seen in the mass spectra. With a 532 nm excitation line, the broad baseline rise and fall are indicative of fluorescence arising from oil contamination in the surface of the wafer.

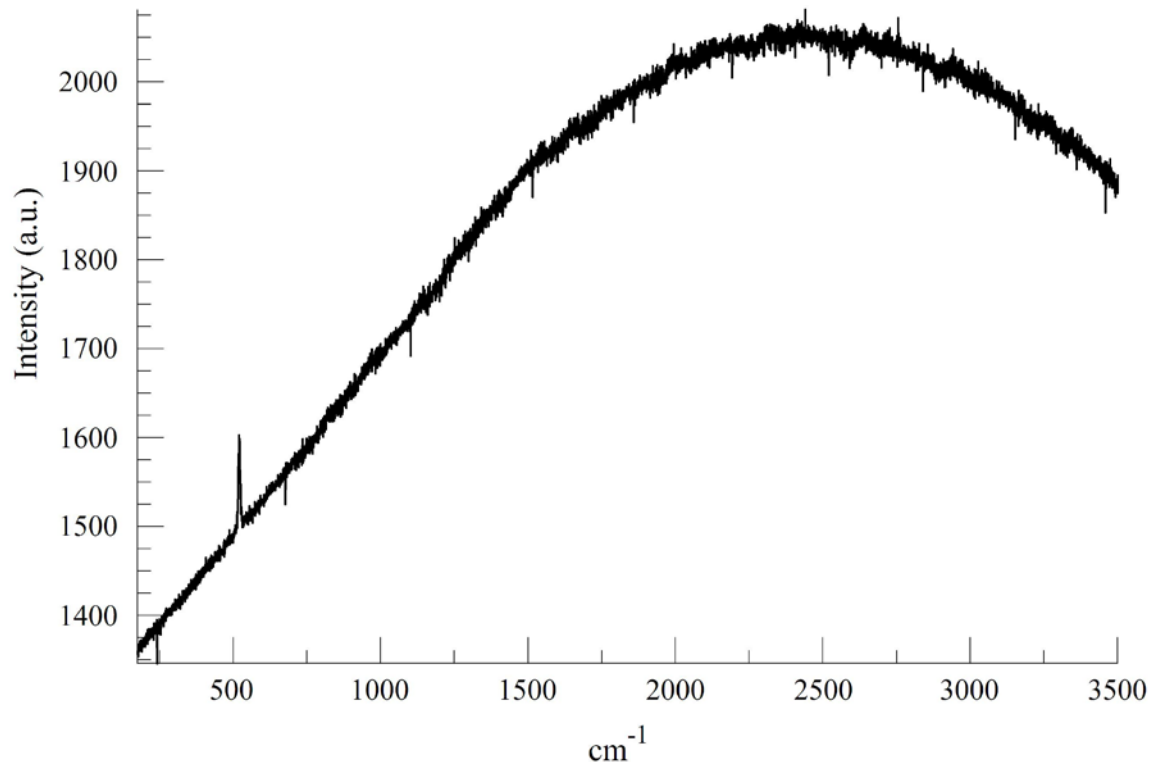


FIG. 43—Raman spectrum of the carbon deposited after 72 hours of pumping via the rotary vane pump.

5.7 References

1. Davila SJ, Birdwell DO, Verbeck GF. Drift tube soft-landing for the production and characterization of materials: Applied to Cu clusters. *Rev Sci Instrum.* 2010 Mar;81(3).
2. Hanley L, Sinnott SB. The growth and modification of materials via ion-surface processing. *Surf Sci.* 2002 Mar 10;500(1-3):500-22.
3. Wang H, Yan S, Salley SO, Ng KYS. Hydrocarbon Fuels Production from Hydrocracking of Soybean Oil Using Transition Metal Carbides and Nitrides Supported on ZSM-5. *Industrial & Engineering Chemistry Research.* [doi: 10.1021/ie3000776]. 2012 2012/08/01;51(30):10066-73.
4. Sotok T, Schmidt T, Hronec M. Hydrogenolysis of polyalcohols in the presence of metal phosphide catalysts. *Applied Catalysis A: General.* 2013;459(0):26-33.
5. Abate F, D'Agostino V, Di Giuda R, Senatore A. Tribological behaviour of MoS₂ and inorganic fullerene-like WS₂ nanoparticles under boundary and mixed lubrication regimes. *Tribology - Materials, Surfaces & Interfaces.* [doi:10.1179/175158310X12678019274282]. 2010;4(2):91-8.
6. Amano H. Progress and Prospect of the Growth of Wide-Band-Gap Group III Nitrides: Development of the Growth Method for Single-Crystal Bulk GaN. *Japanese Journal of Applied Physics.* 2013;52.
7. Peng J-W, Liu P-C, Lee S. Reversible band gap tuning of metal oxide films using hydrogen and oxygen plasmas. *Thin Solid Films.* 2013;531(0):81-7.
8. Casari CS, Bassi AL, Ravagnan L, Siviero F, Lenardi C, Barborini E, et al. Gas exposure and thermal stability of linear carbon chains in nanostructured carbon films investigated by in situ Raman spectroscopy. *Carbon.* 2004;42(5-6):1103-6.
9. Xu H, Chen Y, Xu W, Zhang H, Kong J, Dresselhaus MS, et al. Modulating the Charge-Transfer Enhancement in GERS using an Electrical Field under Vacuum and an n/p-Doping Atmosphere. *Small.* 2011;7(20):2945-52.
10. Dao Y, Sayers DE, Nemanich RJ. Phase stabilities and surface morphologies of (Ti_{1-x}Zrx)Si₂ thin films on Si(100). *Journal of Applied Physics.* [Article]. 1995;78(11):6584.
11. Sakamoto M-a, Kusano E, Matsuda H. Structure modification of titanium oxide thin films by rf-plasma assistance in Ti, Al₂O₃ reactive dc and pulsed dc sputtering. *Thin Solid Films.* 2013;531(0):49-55.

12. He L, Wu Z, Li Z, Ju J, Ou Q, Liang R. Surface work function of indium tin oxide treated using plasma immersion ion implantation. *Journal of Physics D: Applied Physics*. [doi:10.1088/0022-3727/46/17/175306]. 2013;46(17):175306-10.
13. Hadjar O, Wang P, Futrell JH, Dessiaterik Y, Zhu ZH, Cowin JP, et al. Design and performance of an instrument for soft landing of Biomolecular ions on surfaces. *Analytical Chemistry*. 2007 Sep 1;79(17):6566-74.
14. Verbeck G, Hoffmann W, Walton B. Soft-landing preparative mass spectrometry. *Analyst*. [10.1039/C2AN35550G]. 2012;137(19):4393-407.
15. Wannier GH. Motion of Gaseous Ions in Strong Electric Fields. *Bell Syst Tech J*. 1953;32:85.
16. McDaniel EW, Moseley JT. Tests of the Wannier Expressions for Diffusion Coefficients of Gaseous Ions in Electric Fields. *Phys Rev A*. 1971;3(3):1040-4.
17. Mason EA, McDaniel W. *Transport properties of ions in gases*: Wiley, 1988.
18. Verbeck GF, Ruotolo BT, Gillig KJ, Russell DH. Resolution equations for high-field ion mobility. *J Am Soc Mass Spectr*. 2004 Sep;15(9):1320-4.
19. Reinhardt K, Kern W. *Handbook of Silicon Wafer Cleaning Technology*, 2nd Edition: Elsevier Science, 2008.
20. Li CW, McKerns MM, Fultz B. Raman spectrometry study of phonon anharmonicity of hafnia at elevated temperatures. *Phys Rev B*. 2009 Aug;80(5).
21. Ferrari AC. Determination of bonding in diamond-like carbon by Raman spectroscopy. *Diamond and Related Materials*. 2002;11:1053-61.
22. Casiraghi C, Ferrari AC, Robertson J. Raman spectroscopy of hydrogenated amorphous carbons. *Phys Rev B*. 2005;72(8):085401.

CHAPTER 6

SURFACE-ENHANCED RAMAN SCATTERING AS A PRE-SCREENING TOOL FOR MASS SPECTROMETRY

6.1 Introduction

Raman spectroscopic methods are conventionally utilized for spectral analysis of small and large compounds in limited amounts due to its nondestructive nature and limited-to-no sample preparation time. The methods employed provide increased sensitivity of analyte detection and have been advanced to provide ultra-trace detection of analytes by modifying the surface which analytes are absorbed or adhered to for analysis (1). Surface enhanced Raman scattering (SERS) provides improved peak signal intensity from samples analyzed (2, 3). SERS has been implemented in a wide range of analytical applications utilizing and experimenting with various metal substrates (4). For single particle analysis, colloidal silver solutions have been utilized and shown to enhance detection of analytes (5). SERS has been employed in many types of small and large molecule analysis as well as various types of applications involving bioselective species (1, 6). Selective capture of particular disease causing bacteria by antibody production has been shown using SERS exhibiting an increased cell readout of 630 to 740 cells/mL in the appropriate buffer solution (7) and chemical change induction of bacteria by antibiotics has been monitored using a developed SERS-active substrate for analysis (8). It has also been incorporated in the characterization of various illicit drugs in trace and ultra-trace amounts. The spectroscopic method is versatile in accommodating various drug analysis procedures. The detection of cocaine in solid particle mixtures has been performed using Raman spectroscopy implementing principal component analysis to facilitate quantitation (9). It has

also been implemented to detect substances through other complex substrates (such as a nail varnish matrix) (10). The heightened attention of the SERS method has led to the research and development of methods that improve illicit drug analysis, such as the use of silver colloids to analyze amphetamine sulfate (11), ecstasy (12), and various opiates (13). The use of silver halide matrices has been implemented for the detection of amphetamine in confiscated drug tablets (14). The coupling of the SERS method with other instrumental methods has been developed as well to advance the improvement of drug analysis especially when dealing with biological matrices (1). This makes it ideal for pharmaceutical drug analysis due to the fact that no sample preparation is required and that analysis of samples can be done in either the solution based or physical form of the analytes in a steadfast manner (15, 16). Increased sensitivity can still be achieved while avoiding this issue. The SERS technique has also been implemented in the procedure for cleaning pharmaceutical manufacturing equipment in order to verify cleaning by industrial standards (17). The coupling of SERS with nanomanipulation has been implemented to provide supplementary characterization of drug analytes. This coupled method has been done to characterize drug analytes on 50 nm gold-plated electrostatic lifts to verify their adherence to the lift via electrostatic lifting (18). Spectra of these drug analytes have been collected in our lab using SERS to provide parallel verification with nanospray ionization/mass spectrometry (NSI/MS) in other experiments.

Electrostatic dust lifting is a method that is utilized in the lifting of prints from many types of surfaces. Surfaces range from a tabletop to the body of a deceased. The electrostatic lifting process involves the use of a high voltage instrument to apply an adjustable voltage to the metallic side of a Mylar film to lift dust particulates off a surface. Normally the use of the electrostatic lifting process is reserved for crime scene investigations to record prints left on a

surface (19). Results with the electrostatic dust lifter are usually achieved with ease and great success as compared with other dust print lifting devices (20). The technique of lifting dust prints has been modified to lift drug particulates in our lab. The chemical extraction of drug analytes from these electrostatic lifts are being performed with nanomanipulation as opposed to the traditional photography utilized in the recording of ridge detail. The electrostatic films were coated beforehand with gold to enhance peak signal intensity of the drug analytes present in the soil matrix for the performance of SERS.

The gold-plating of the electrostatic films for spectral enhancement used in SERS allows for the desired analyte to be detected among a background matrix. The combination of electrostatic lifting with SERS provides an inventive approach to performing trace and ultra-trace analyses of drug particulates. The approach is fast and effective, eliminating the need for sample preparation.

6.2 Methods

For the electrostatic lifts, Mylar® film (DuPont Wilmington, DE) was used as the lifting substrate and a Pathfinder lifter (CSI Equipment ltd. Woburn Sands, England) was used to apply voltage to the films during the lifting procedures. Mass spectral analysis was performed using a TSQ 7000 triple-quad mass spectrometer (Thermo Scientific Waltham, MA). For SERS, gold was deposited on the films in 25, 60 and 100 nm layers using chemical vapor deposition. Raman SERS spectra were obtained using a T64000 triple-grating Raman instrument (HORIBA Jobin Yvon Inc. Edison, NJ), which focused on the sample surface through a 100x microscope objective. Excitation was accomplished with a 532 nm diode-pumped solid-state laser (QED Lasers), attenuated to approximately 34 mW. Backscattered light was captured with the

objective, guided through the spectrometer and detected using a liquid nitrogen cooled CCD camera.

Caffeine was used to validate the lifting procedure and to probe the effectiveness of the gold-coated films for use in SERS analysis. In order to determine the optimum time to apply the lifting voltage, a small quantity of pure caffeine (<0.003 g) was placed on clean countertop and a 1.0 in² sheet of Mylar® was placed over it. Then, voltage was applied via the lifter. The lifted material was then rinsed from the film using 1.0 mL of electrospray solvent (a 50/50 mix of methanol and water with 1.0 % acetic acid). The resulting solution was diluted 1/100 with additional electrospray solvent, and then analyzed via NSI/MS. This was repeated six times, allowing for incrementally longer periods of lifting voltage to be applied. For nanoextraction NSI/MS, 10 µl of electrospray solvent was loaded into a coated capillary tip, and then placed into a pressure injector on the nanomanipulator (Zyvex Richardson, TX). The tip of the capillary was positioned approximately 1 µm away from an analyte crystal, and solvent was injected onto the crystal at a pressure of 23 psi. After allowing 10 sec for the crystal to dissolve, the solution was aspirated into the capillary at a pressure of 60 psi. The resulting solution was analyzed via NSI/MS. For validation of the SERS analysis, a small quantity of pure caffeine (<0.003 g) was placed on clean countertop and a 1.0 in² sheet of Mylar® was placed over it. Voltage was then applied to the film with the lifting apparatus for twenty seconds in order to retrieve the caffeine. The sample was then observed under the Raman microscope, and particles of approximately 1-3 µm in diameter were chosen for spectral analysis (unless otherwise noted). This procedure was repeated for each of the gold-plated films.

To test the selectivity of the lifting procedure, small quantities of caffeine (<0.003 g) and soil (~0.020 g, primarily sand) were mixed and then lifted with Mylar® and the gold-plated

films. The films were weighed before and after each lift in order to determine the amount of material collected. Raman was used to analyze the lifted material. This procedure was then used to lift and analyze samples of rock cocaine, crystal meth and ecstasy provided by the University of North Texas Police Department (Denton, TX).

An area of the gold-plated film (60 nm) containing both sand and cocaine particles was selected for the imaging experiment. Spectra were collected at 5.0 μm increments in a 60 μm by 80 μm grid and baseline corrected. Of the resulting spectra, the intensity of the cocaine peak at 1004 cm^{-1} was used to create a contour plot of the area imaged.

Finally, two lifts were performed with each of the four analytes. One was prepared for electrospray ionization/mass spectrometry (ESI/MS) and the other for NSI/MS using the methods described above in order to compare the selectivity of each technique.

6.3 Results

Fig 44 shows the total ion counts for the 194 m/z peak for caffeine lifted for various lengths of time. It was determined that 20 seconds of voltage provided the highest yield in terms of material collected on the film. This amount of time was used in all further experiments.

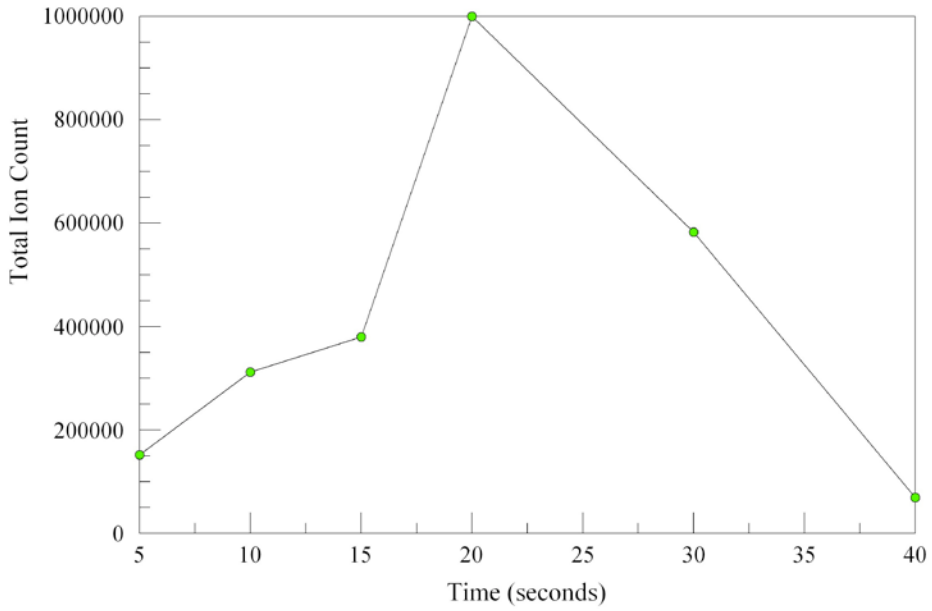


FIG. 44—*Total ion counts for the caffeine peak in the mass spectra for samples lifted using 5-40 seconds of applied voltage.*

Fig 45 shows both the microscope image of the section used in the imaging experiment and the resulting Raman map of the surface. Of the particles visible on the surface, three can easily be identified as rock cocaine based on the Raman spectra of the surface. This method of screening lends itself to quick identification of the particles and can be followed with additional particle-specific analysis such as nanoextraction and identification with NSI-MS.

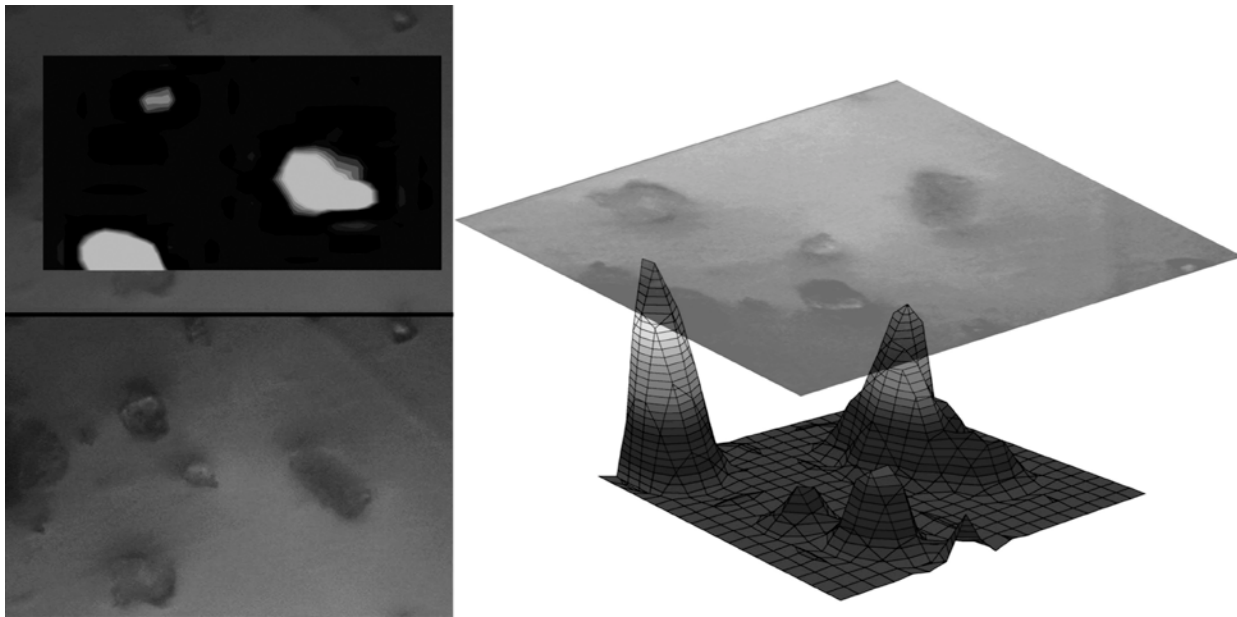


FIG. 45—*Microscope image of the aream mapped in the Raman analysis of cocaine and sand (bottom left). Contour map overlaid in the image (top left) showing areas of cocaine signal in grey and white (the threshold peak intensity for white is 12.23 a.u.). Three-dimensional plot of the Raman image with the microscope image overlaid (right).*

Quantitative amounts of gold (25-100 nm films) were deposited on the Mylar® in order to strike a balance between the lifting effect of the substrate and the SERS enhancement from the gold. All of the gold-coated films preferentially lifted analyte particles and only trace quantities of soil. The sizes of the analyte particles that were lifted varied from roughly 0.5 mm to 1.0 μm in diameter. Overall, this might suggest that the electrostatic properties of the organic analyte particles are more accommodating to the gold substrate due to a higher polarizability over the soil matrix. This effect may also be augmented by the conductive nature of the metal film. Given the tendency of the gold-coated films to selectively lift the organic analyte particles as opposed to the soil matrix, a two-step approach (Fig 46) would act to further improve this method. In this instance, the print can be lifted using an uncoated film, effectively collecting both the analyte and matrix particles comprising the print. This could be directly followed by a second lift performed by covering the initial lift with a gold-coated film and applying voltage to

collect latent drug residues. This would provide both an effective print lift, and a substrate on which to collect and analyze the drug residues via SERS.

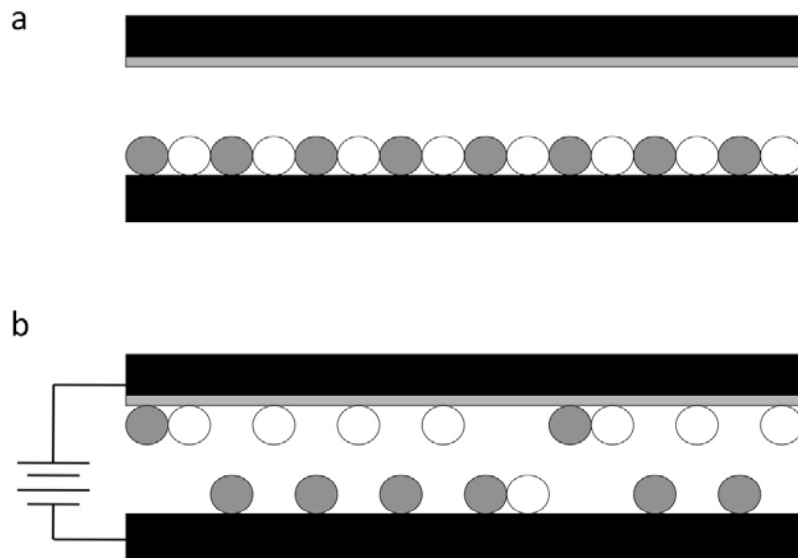


FIG. 46—*Schematic diagram of a two-step lifting process where a) a primary lift containing both analyte (white) and matrix (grey) particles is covered with a gold-coated film and b) a secondary lift is performed to collect the analyte particles for SERS analysis, leaving the primary lift in tact.*

Fig 47 shows the spectra obtained from the caffeine lifted on the four films. On the uncoated film, only peaks characteristic Mylar® are observed. The spectrum from the 25 nm gold film displays the larger peak from caffeine (at 551 cm^{-1}). At 60 and 100 nm gold coverage, the peaks from the Mylar® film are no longer present, and the caffeine signal is readily identifiable. Full spectra, showing the suppression of the Mylar® Raman signals, can be seen in Fig 48 for the caffeine on Mylar® and the caffeine on the 100 nm gold film. The spectra from the caffeine-soil mixture showed no notable differences from the caffeine standard and have thus been omitted. There was a notable increase in the mass of lifted particles on the uncoated film, however the mass of particles lifted by gold-coated films still could not be determined due to the trace quantities recovered.

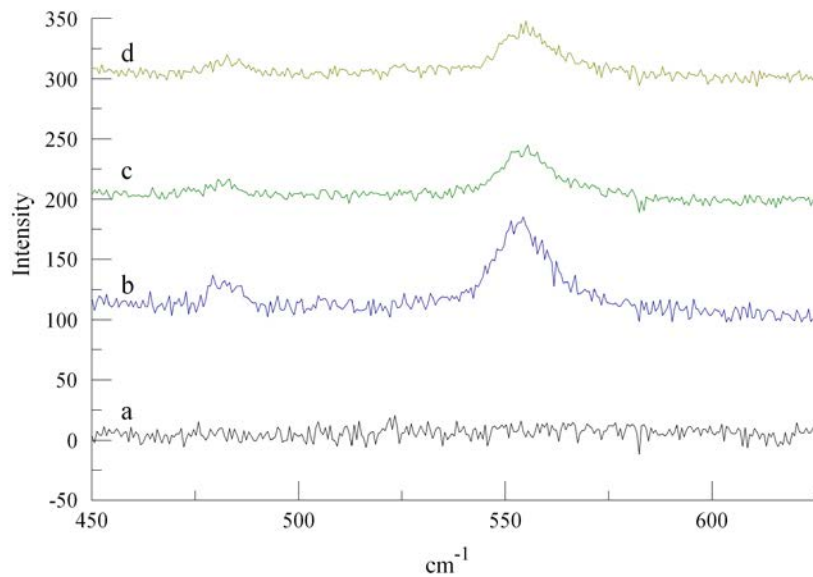


FIG. 47—Raman spectrum of the caffeine standard on a) Mylar® film, b) 25 nm gold film, c) 60 nm gold film and d) 100 nm gold film.

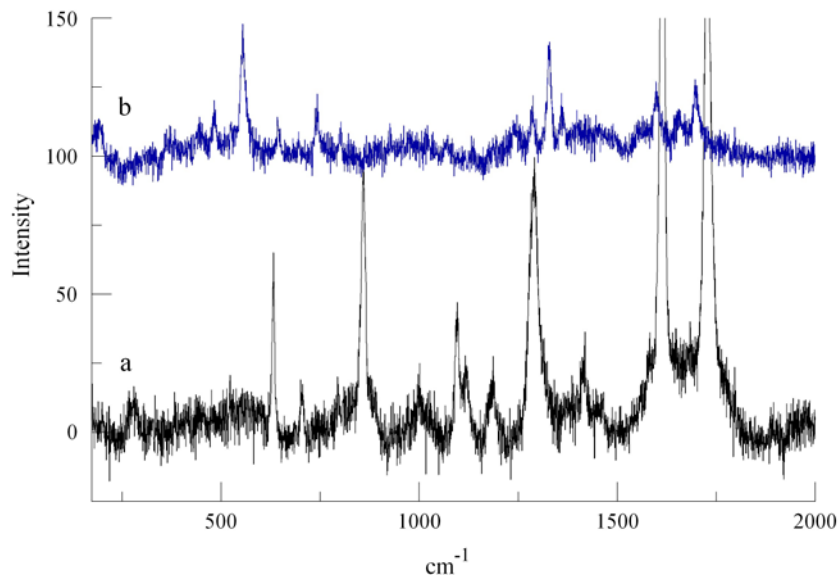


FIG. 48—Comparisons of the full spectra for (a) caffeine on Mylar® and (b) caffeine on the 100 nm gold film.

Figs 49 through 51 show the spectra collected from the mixtures of the drug samples and soil lifted on the four different films. Again, no analyte peaks are observed on the uncoated films with the exception of a small peak at 810 cm⁻¹ in the spectrum for ecstasy. In this case, a

significantly larger particle ($\sim 10 \mu\text{m}$ in diameter) was chosen for analysis due to excessive scattering of the laser line and baseline noise in the spectrum. The spectra for the 25 nm films show no signs of the spectral peaks for the film, displaying a successful suppression of the background signal. While this is true, the signal for crystal meth remains low, showing only the most intense peak in the spectrum near 1000 cm^{-1} . The 60 and 100 nm gold films both show enhancements in the Raman spectra of crystal meth and cocaine. The spectrum for ecstasy on the 60 nm gold film shows a marked reduction in signal strength; however, this is likely to be the result of particle selection and not the effect of the gold substrate. Overall, the 60 and 100 nm gold films showed the best consistent enhancement of the Raman signal.

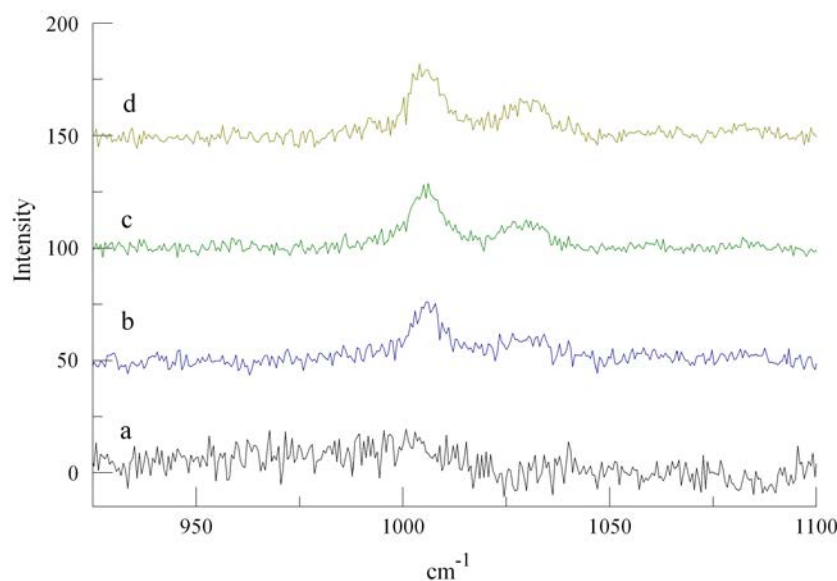


FIG. 49—Raman spectrum for cocaine on a) Mylar® film, b) 25 nm gold film, c) 60 nm gold film and d) 100 nm gold film.

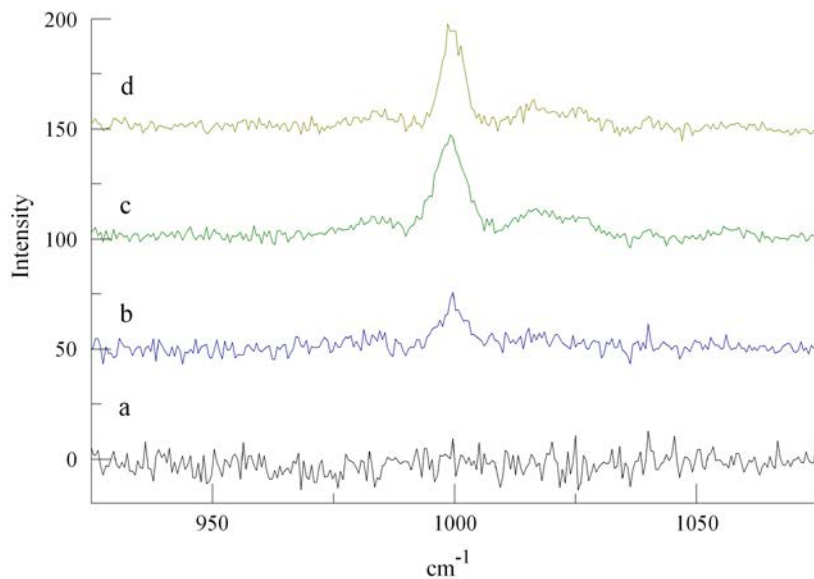


FIG 50—Raman spectrum for crystal meth on a) Mylar® film, b) 25 nm gold film, c) 60 nm gold film and d) 100 nm gold film.

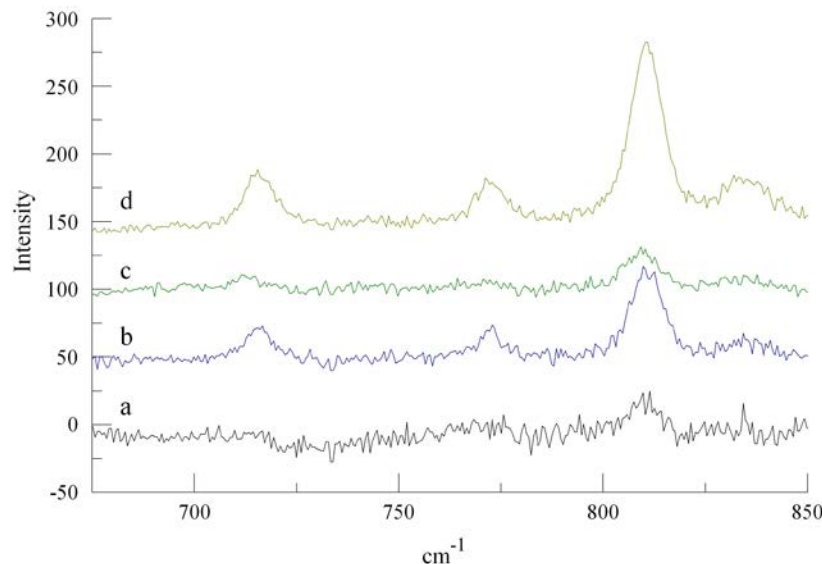


FIG. 51—Raman spectrum for MDMA on a) Mylar® film, b) 25 nm gold film, c) 60 nm gold film and d) 100 nm gold film.

Fig 52 shows the signal-to-noise ratio (SNR) for the four samples on each of the four substrates. For caffeine, cocaine and crystal meth, the SNR on the uncoated Mylar® is zero, due to the lack of spectral peaks representing the analyte. For the caffeine standard, the 25 nm gold

film shows a marked increase in the SNR. It should be noted that the full spectrum on the 25 nm film displayed both spectral peaks for caffeine and the Mylar® film. Only at 60 nm were the peaks from the film fully suppressed. For the three illicit drug samples, it can be seen that the SNR increases with presence of thicker gold layers (with the exception of the aforementioned MDMA sample).

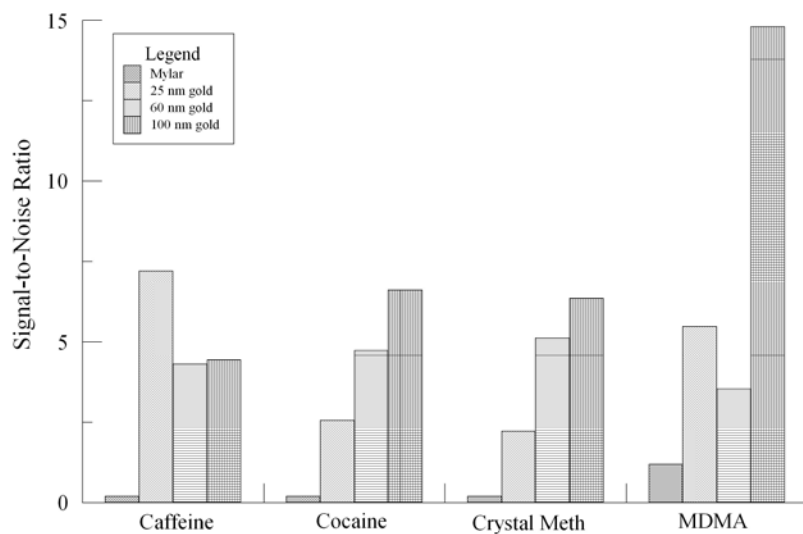


FIG. 52—Comparison of the signal-to-noise ratios for the four samples on each of the films.

The results of the ESI/ and NSI/MS experiments can be seen in Fig 53. The results of these sampling and analysis methods differ in two specific ways. The most immediate difference noted is the presence of contaminant peaks in the ESI/MS spectra resulting from the electrospray wash across the surface of the gold-coated Mylar®. Because nanoextraction allows for extremely localized sampling, few contaminants are noted. Secondly, the absolute intensity of the NSI/MS spectra are significantly higher, resulting from decreased solvent-to-analyte ratio during the extraction process.

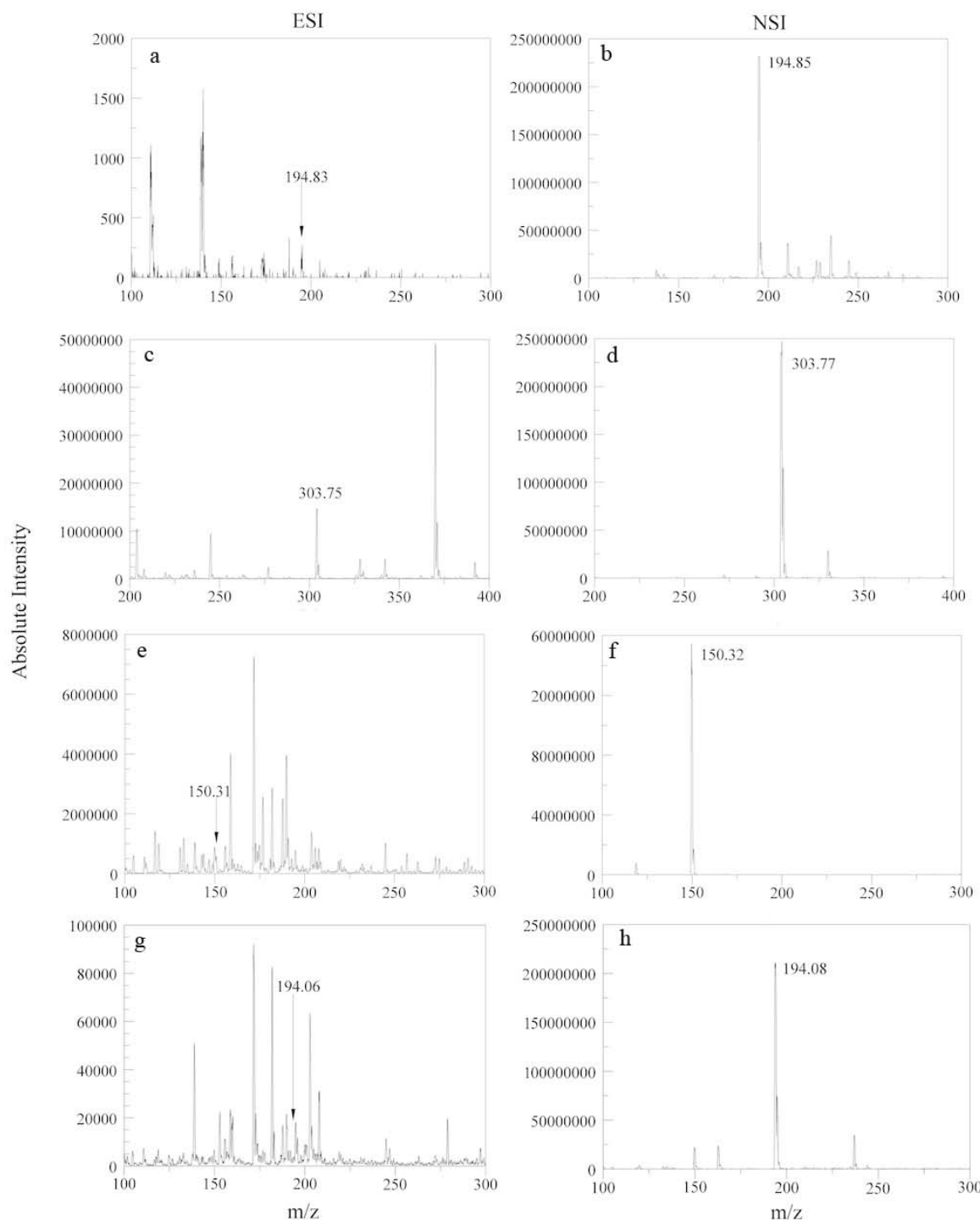


FIG. 53—Comparisons of ESI/MS (left) and NSI/MS (right) for caffeine (a,b), cocaine (c,d), MDMA (e,f) and methamphetamine (g,h).

6.5 References

1. Ryder AG. Surface enhanced Raman scattering for narcotic detection and applications to chemical biology. *Current Opinion in Chemical Biology.* 2005;9(5):489-93.
2. GarciaVidal FJ, Pendry JB. Collective theory for surface enhanced Raman scattering. *Phys Rev Lett.* 1996 Aug 5;77(6):1163-6.
3. Kneipp K, Kneipp H, Itzkan I, Dasari RR, Feld MS. Surface-enhanced Raman scattering and biophysics. *J Phys-Condens Mat.* 2002 May 13;14(18):R597-R624.
4. Campion A, Kambhampati P. Surface-enhanced Raman scattering. *Chem Soc Rev.* 1998 Jul;27(4):241-50.
5. Kneipp K, Wang Y, Kneipp H, Perelman LT, Itzkan I, Dasari R, et al. Single molecule detection using surface-enhanced Raman scattering (SERS). *Phys Rev Lett.* 1997 Mar 3;78(9):1667-70.
6. Grubisha DS, Lipert RJ, Park HY, Driskell J, Porter MD. Femtomolar detection of prostate-specific antigen: An immunoassay based on surface-enhanced Raman scattering and immunogold labels. *Analytical Chemistry.* 2003 Nov 1;75(21):5936-43.
7. Yakes BJ, Lipert RJ, Bannantine JP, Porter MD. Impact of protein shedding on detection of *Mycobacterium avium* subsp *paratuberculosis* by a whole-cell immunoassay incorporating surface-enhanced Raman scattering. *Clin Vaccine Immunol.* 2008 Feb;15(2):235-42.
8. Liu TT, Lin YH, Hung CS, Liu TJ, Chen Y, Huang YC, et al. A High Speed Detection Platform Based on Surface-Enhanced Raman Scattering for Monitoring Antibiotic-Induced Chemical Changes in Bacteria Cell Wall. *Plos One.* 2009 May 7;4(5).
9. Ryder AG, O'Connor GM, Glynn TJ. Quantitative analysis of cocaine in solid mixtures using Raman spectroscopy and chemometric methods. *Journal of Raman Spectroscopy.* 2000;31(3):221-7.
10. Ali E, Edwards H, Hargreaves M, Scowen I. Raman spectroscopic investigation of cocaine hydrochloride on human nail in a forensic context. *Analytical and Bioanalytical Chemistry.* 2008;390(4):1159-66.
11. Faulds K, Smith WE, Graham D, Lacey RJ. Assessment of silver and gold substrates for the detection of amphetamine sulfate by surface enhanced Raman scattering (SERS). *Analyst.* 2002;127(2):282-6.
12. Bell SEJ, Fido LA, Sirimuthu NMS, Speers SJ, Peters KL, Cosbey SH. Screening Tablets for DOB Using Surface-Enhanced Raman Spectroscopy*. *Journal of Forensic Sciences.* 2007;52(5):1063-7.

13. Rana V, Canamares MV, Kubic T, Leona M, Lombardi JR. Surface-enhanced Raman Spectroscopy for Trace Identification of Controlled Substances: Morphine, Codeine, and Hydrocodone. *Journal of Forensic Sciences*. 2011 Jan;56(1):200-7.
14. Sagmuller B, Schwarze B, Brehm G, Schneider S. Application of SERS spectroscopy to the identification of (3,4-methylenedioxy) amphetamine in forensic samples utilizing matrix stabilized silver halides. *Analyst*. 2001;126(11):2066-71.
15. Fini G. Applications of Raman spectroscopy to pharmacy. *Journal of Raman Spectroscopy*. 2004 May;35(5):335-7.
16. Strachan CJ, Rades T, Gordon KC, Rantanen J. Raman spectroscopy for quantitative analysis of pharmaceutical solids. *J Pharm Pharmacol*. 2007 Feb;59(2):179-92.
17. Corrigan DK, Salton NA, Preston C, Piletsky S. Towards the development of a rapid, portable, surface enhanced Raman spectroscopy based cleaning verification system for the drug nelarabine. *J Pharm Pharmacol*. 2010 Sep;62(9):1195-200.
18. Wallace N, Hueske E, Verbeck GF. Ultra-trace analysis of illicit drugs from transfer of an electrostatic lift. *Science & Justice*. 2011 Dec;51(4):196-203.
19. LeMay J. Evidence Beneath Your Feet. *Law Enforcement Technology*. 2006;33(3):42-5.
20. Craig CL, Hornsby BM, Riles M. Evaluation and comparison of the electrostatic dust print lifter and the electrostatic detection Apparatus(2) on the development of footwear impressions on paper. *Journal of Forensic Sciences*. 2006 Jul;51(4):819-26.

CHAPTER 7

CONCLUSIONS AND FUTURE WORK

The utility of mass spectrometry and the potential for miniaturized instruments have been demonstrated via the experiments detailed here. While the work has been informative, it is, by no means, complete.

The miniature mass spectrometer shows functionality typical of a device of its dimensions, however, the power supplies and vacuum hardware used are all laboratory grade bench-top and rack-mountable units. The ultimate goal of this line of research is to produce a self-contained and remotely deployable instrument capable of recording and transmitting real-time data. There are several factors to take into account before this goal can be fully realized. First, in order to develop a ruggedized instrument capable of deployment, most (or all) moving parts will need to be replaced with solid-state components. For sample introduction, this is a simple step. The use of a heated, semi-permeable membrane would allow for the sampling of volatile compounds. Next, the vacuum system would need to be redesigned to house the mass spectrometer in a compact package with little dead space to decrease the pumping load. More importantly, the turbomolecular pump would need to be replaced by an array of sintered porous non-evaporative getters. Unfortunately, an initial roughing stage would still be needed, although once low vacuum is reached, activation of the getters can maintain high vacuum ($<10^{-6}$) for periods up to 18 hours. Both the membrane inlet and the getters are ideas that have been explored in our lab.

The MEMS mass spectrometers discussed in Chapter 4 show much promise. With the ability to utilize multiple substrates such as Pyrex, sapphire, and aluminum nitride, we have the

potential to make ion lenses that can withstand an applied potential above 2 kV before breakdown with electrode spacing of 100 μm or less. These devices have been created with less than 5 μm minimal feature sizes and less than 250 nm position and assembly accuracy. This precision and accuracy are created utilizing an encoded piezo manipulator (x,y,z), with pick-n-place capabilities. The angular alignment of the assembled structures is shown to be less than a degree. Though the devices work as proper ion optics, designs need to be enhanced to improve alignment. Field aberrations at this device size need to be taken seriously, and methods to reduce these aberrations must be implemented to bring these optics into common place environments. MEMS devices have been employed in pressure detection, ion sources, mass analysis, and detection. All-in-one mass spectrometers should be arriving on the stage.

With the portability, ruggedness, and low cost of such devices, these future handheld chemical analyzers can aide in water quality monitoring, disease combing, soil contamination, and can be customized for an array of field applications.

The initial work on designing and constructing a platform for the generation and deposition of gas phase clusters, plasma deposition and modification and multi-spectral analyses has been discussed in some detail. It is clear that these experiments cover only the introductory work needed to fully realize the system, however, it's utility cannot be understated. For precision work, it will be necessary in future experiments to forego the use of vacuum pumps that operate via an oil seal. While the apparent contribution of the water and oil contamination from the rotary vane pump seemed minimal, a closer inspection with Raman microscopy revealed the extent to which such contamination could adversely affect results. In addition to this, a redesign of the sample stage will be necessary to continue effectively performing *in situ* Raman analyses. Isolation pads between the chamber and the laser table stage and the addition

of a dampening material to the exterior portion of the linear actuator would be a good start to this work. The configuration of flanges may be necessary if laser ablation it to be used for ion generation in SLIM experiments, as the mobility cell, sample holder and ablation window restrict access to the two remaining flanges on top of the chamber. Finally, the last piece of the equation will be to add multiple internal reflection infrared spectroscopy for the analysis of deposited films. This will require optics that can be house within the chamber and must be able to withstand low vacuum pressures (millitorr range). The individual components of the multi-analysis platform that have been tested and discussed in this work have been shown to be effective at the creation, deposition and analysis of gas-phase metal clusters. As previously stated, the largest conflict to overcome before this system can be fully integrated is the placement and orientation of the components. Nevertheless, the utility of such a platform cannot be understated given the demand for exploration in materials research.

The coupling of the electrostatic lifting method with gold-coated Mylar® films has been shown to be an effective process in the analysis of ultra trace drug residues. By selectively lifting analyte particles over the matrix, the overall time for microscopic screening of the lift contents is effectively reduced. This also lends itself to analyte-specific extraction while keeping the original lifted print in tact, providing an excellent and nondestructive pre-screening tool for nanoextraction methods and subsequent mass spectral analysis. In addition to this, the gold coatings on the films provide an effective substrate on which to perform SERS analysis. The analyte spectra display significant signal increases with the presence of the gold films, and the peaks arising from the film substrate are reduced or eliminated. While the transfer of residual amounts illicit materials amongst users and traffickers is already distinguishable with current techniques, expanding available analyses to include ultra trace amounts blurs the line between

the parties who are directly involved and those who are not, but are in some limited amount of contact with them. As research progresses into the realm of ultra trace analysis, the interpretation of results will need to be addressed in a legal context if these methods are to be used efficiently and effectively. The proposed two-stage lift for the collection and separation of fingerprints left in dust and organic material therein can provide a valuable tool in the field. If this project were to proceed, a field-ready prototype would need to be constructed in order to facilitate this process outside of a laboratory environment.